THE ROLE OF FLUTE MORPHOLOGY IN MECHANICAL BEHAVIOUR OF CORRUGATED FIBREBOARD – A NUMERICAL, ANALYTICAL AND EMPIRICAL STUDY

A thesis presented in partial fulfilment
of the requirements for the degree of

Doctor of Philosophy
in
Engineering

at Massey University, Palmerston North, New Zealand.

Aiman Jamsari

2020

To corrugating and

beyond . . .

Abstract

Corrugated fibreboard (CFB) packaging is designed to protect its contents during the shipping and storage of goods – a role threatened by damage to the CFB. Damaged goods will not only make the customers unhappy but also cause significant loss to the suppliers. As different goods require different design of CFB box, there is no one solution fits all to overcome this issue. This thesis was focused on understanding the fundamentals of CFB damage, relating the damage with the strength loss, and including the damage in strength predictive tools such as finite element (FE) and analytical models to allow for faster design of CFB boxes and the possibility of finding optimal solutions for different requirements. The type of CFB damage that the research narrowed down into was changes to the flute profile that could arise. Such flute damage could be unintentional (crushing and indentation at any stage during the shelf life of the packaging) or intentional (accompanying perforation for instance – a design option to provide secondary functionality such as in shelf ready applications). There is currently no systematic way of observing and quantifying the structure of the flute profile to allow for a proper understanding of the morphology of the flute. Typically, this is done either through measuring the change in calliper or direct observation on the profiles at the edge of CFB blanks which suffers additional physical damage due indentation from the cutting process. A new technique was presented to be able to do this by laser cutting the samples and digitalising the flutes. The method also includes a statistical tool that can compare different flutes and quantify the change in morphology through a variable called the 'Similarity Factor'. The technique was demonstrated for flute profiles with different extents of crushing, and also allowed for transferring the digitalised profile for FE modelling purposes.

Developing a full box compression strength (BCT) FE model with the micro-geometry of the fluting structure can be very time consuming as it will involve a huge number of mesh element and result in a long simulation time. So to overcome this, smaller component models like the bending and crushing tests that have been shown to be the largest factor affecting the BCT were developed with micro-geometry structure that allowed for significantly less computation time and better understanding of the effect of flute profile. A new finding identified through the application of the bending model was that the orientation of the sample can be rotated to find an optimal orientation angle that gives the best bending stiffness and maximum bending force performance. Analytical models were also assembled, and their performance compared with the FE models. These provided accurate outcomes for bending but were limited in cases such as inability to predict the maximum bending force and determining the locus of failure.

Global damage to the CFB was simulated through deliberately crushing samples to different extents experimentally. The effect of different levels of crushing on flute morphology and mechanical performance was measured through image analysis, torsional, compressive and bending tests. These tests showed that the torsional behaviour of CFB had the highest sensitivity to crushing at low levels. Since the flute morphology measurements showed negligible changes (the original flute geometry was recovered after crushing), it is suggested that the crushing could affect other localised damage to CFB components such as to the fibres in the constituent papers. Further investigation of the extent and nature of this damage could be an interesting extension to find out its relation to the BCT. On the other hand, the reduction in bending strength and edge crush test followed a similar tend to change in flute morphology with increasing crush levels. This shows that some of the loss in strength could be attributed to the change in flute geometry as well as the reduction in calliper (beyond a threshold where morphology was recoverable after compression).

By combining the new tool to characterise the flute structure and with models of varying complexity, their ability to predict the strength of CFB at different extents of crushing could be compared (simulating unintentional damage). These models consisted of an actual flute geometry, idealized flute geometry and an equivalent flute geometry FE models along with analytical solution models. This comparison showed that the use of an actual flute geometry was useful to predict mechanical performance but that the dominant effect on bending strength is the calliper and the flute morphology is a secondary influence.

The utility of the FE model was further demonstrated with inclusion of an intentional localised damage through perforation. The model accurately predicted the drop in the experimentally measured apparent bending stiffness. The findings of the localised perforation study also demonstrated that the bending force of the CFB can be significantly improved by avoiding punching through the peaks that rest on the compressive side of the liner.

The key new contribution of this research was the development of new a way to accurately measure and describe the actual flute profile within CFB exposed to pre-test damage. The profile allowed geometric damage to be quantified and for the true profile to be included in detailed finite element modelling of mechanical behavior. The effect of flute damage on the mechanical behavior of CFB could therefore be determined and predicted and allowed the potential effects on the strength of CFB packages to be inferred.

Acknowledgment

Looking back, I have come a long way from the first day that I started my PhD. Foremost, I would like to express my gratitude to my chief supervisor, Prof. John Bronlund for the various critical thinking ways you taught me over the years. I expect to graduate as a doctor to boxes with him but along the way also grab some short-courses uncertified certs on stuff like steaks and coffee. Most importantly, John taught me a lot about the balance of career and life.

Next goes to Dr. Celia Kueh for being patience at me knocking your door almost every other day when I spent half a year trying to get the model converge, Dr. Eli Gray-Stuart for the guidance and advices you've given me from time to time especially in the first and hardest year (and also a great football teammate!), Dr. Karl Dahm for constantly making explanation on mechanics of materials sounds as easy as ABC (of course there are times when I was still clueless) and Dr. Gonzalo Martinez, who along with John, showed me that optimisation is a way of life. Not to forget staff from Scion; Kelly Wade, Grant Emms, Saad Hussain and Donna for all the inputs and help on corrugated box.

I would also like to thank other members of the Massey packaging team, Andrew East, Gabe Redding, Ramsay Huang, Jamal Olatunji, Nico Tapia and Peter Jefferey. The opportunity to engage with doing industrial trial had given me a valuable practical experience, not to mention the joy of having good dinner after long days of loading boxes. Thanks to the lab technician in School of Food and Advanced Technology, especially Ian Thomas, Clive Bardell, Glenda Rosoman, Anthony Wade, Morio Fukoa, Steve Glassgow, Ann-Marie, John Edwards and Haoran Wang. Coming back and forth to repeat same experiments numerous times are all worth it now.

Thanks also to my colleagues, some which are also part of my footy team that kept my sanity level intact: Max, Matt, Gerald, How, Sebastian and others I may have forgot to mention.

Most special thanks to the love of my life, Siti Nadjiha Rozali, who I am indebted for every highs and lows we went through finishing our PhD together, my beloved parents, Mama and Abah, and siblings for the love, support and encouragement throughout my whole life. And not to forget, our little 7-months Daniel who actually did wrote a small sentence in this thesis and our Lady cat that always puts smile on my face (except when waking us up at night for more foods).

TABLE OF CONTENT

Index of Abbreviations

°C	Degree Celcius
3D	3 Dimensional
ACP	ANSYS Composite PrepPost
ANOVA	Analysis of Variance
BCT	Box Compression Test
BPI	Board performance indicator
CAD	Computer-Aided Drawing
CCT	Corrugated crush test
CD	Cross-machine Direction (perpendicular to the direction of the flute)
CFB	Corrugated Fibreboard
CFC	Carbon Fibre Composite
CT	Computed Technology
DST	Dynamic stiffness testing
ECT	Edge Crush Test
FE	Finite Element
MANOVA	Multivariate analysis of variance
MD	Machine Direction (parallel to the direction of the flute)
PU	Polyurethane
RCT	Ring crush test
RH	Relative Humidity
SCT	Short-span compression test
SF	Similarity Factor
TAPPI	Technical Assoc. Paper, Pulp Converting Standards
ZD	Thickness direction

Index of Symbols

a	Distance between bottom and upper anvil in four-point bending setup	m
Cu	Copper	
D	Bending/Flexural Stiffness	N.m
E	Elastic Modulus	Pa
E_{11}	Elastic modulus in the machine direction	Pa
E_{22}	Elastic modulus in the cross-machine direction	Pa
E_{33}	Elastic modulus in the thickness direction	Pa
G_{12}	In-plane shear modulus	Pa
G_{13}	Out-of-plane shear modulus in direction MD-ZD	Pa
G_{23}	Out-of-plane shear modulus in direction CD-ZD	Pa
H, h	Height of corrugated board	m
h_f, h_c	Height of flute/core	m
$I_{y,c}$	Second moment of area of the flute	m^4
k	Constant for loss of the strength in flute during the conversion for the ECT analytical equation	
L	Length of the flute flank	m
L_{bottom}	Distance between bottom anvils in four-point bending setup	m
P	Pitch	m
R	Flute tip radius	m
S	Tensile stiffness of paper	N/m
$S_{1,f1}$	MD tensile modulus of the inner paper	N/m
$S_{1,f3}$	MD tensile modulus of the outer paper	N/m
$S_{2,c}$	CD tensile modulus of the flute paper	N/m
$S_{2,f1}$	CD tensile modulus of the inner paper	N/m
$S_{2,f3}$	CD tensile modulus of the outer paper	N/m
t_c	Fluting paper thickness	m

t_{f1}	Thickness of the inner paper	m
t_{f2}, t_{f3}	Thickness of the outer paper	m
v_{12}	In-plane Poisson's ratio	
v_{13}	Out-of-plane Poisson's ratio in direction MD-ZD	
v_{23}	Out-of-plane Poisson's ratio in direction CD-ZD	
w	Width of CFB sample	m
α	Take-up ratio	
β	Angle of the flute flank	°
Δ	Linear slope of the force-centre deflection graph	N/m
ρ	Density	kg/m^3
σ_{11}	Stress in direction MD (subscripts *c* refers to compression, *t* refers to tensile)	Pa
σ_{22}	Stress in direction CD (subscripts *c* refers to compression, *t* refers to tensile)	Pa
σ_{33}	Stress in direction ZD (subscripts *c* refers to compression, *t* refers to tensile)	Pa
$\sigma_{CD,F}$	Compression strength of the flute in CD	N/m
$\sigma_{CD,L1}$	Compression strength of the inner liner in CD	N/m
$\sigma_{CD,L2}$	Compression strength of the outer liner in CD	N/m
τ_{12}	In-plane shear stress	Pa
τ_{13}	Out-of-plane shear stress in direction MD-ZD	Pa
τ_{23}	Out-of-plane shear stress in direction CD-ZD	Pa
ω	Angular frequency	rad/sec

Index of Figures

Index of Tables

List of Conference and Publications

Peer-reviewed papers:

Jamsari, M. A., Kueh, C., Gray-Stuart, E., Martinez-Hermosilla, G. A., Dahm, K., & Bronlund, J. E. (2019). A technique to quantify morphological damage of the flute profile in the midplane of corrugated fibreboard. Packaging Technology and Science, 32(5), 213-226.

Jamsari MA, Kueh C, Gray - Stuart EM, Dahm K, Bronlund JE (2019). Experimental and numerical performance of corrugated fibreboard at different orientations under four-point bending test. Packaging Technology and Science, 32(11), 555-565.

Jamsari, M. A., Kueh, C., Gray - Stuart, E. M., Dahm, K., & Bronlund, J. E. (2020). Modelling the impact of crushing on the strength performance of corrugated fibreboard. Packaging Technology and Science.

Conferences, symposium:

Jamsari, M. A., Kueh, C., Gray-Stuart, E., Martinez-Hermosilla, G. A., Dahm, K., & Bronlund, J. E. (2018). A Technique to Quantify Damage of the Flute Profile in the Mid-Plane of Corrugated Fibreboard. In The 21st IAPRI World Conference on Packaging, 19-22 June 2018, Zhuhai, China.

Kueh, C., Jamsari, M. A., Dahm, K., Ilanko, S., & Bronlund, J. E. (2019). Natural frequency modelling to identify material properties of crush damaged corrugated fibreboard. The 13th International Conference Computational Structures Technology, 4-6 September 2018, Sitges, Barcelona, Spain

“Modelling the Edge Crushing Performance of Corrugated Fibreboard under Different Moisture Content Levels” (ID: 4981) presented at International Conference on Computational & Experimental Engineering and Sciences (ICCES 2019) Tokyo, Japan March 25th -28th 2019

Chapter 1.

Introduction

1.1. What is corrugated fibreboard and why is it important?

Corrugated fibreboard (CFB) is regularly used to construct boxes to export, ship and store products. It is famous for its light-weight and high-strength imparted by the corrugated flute structure while maintaining a low cost. During the lifetime of CFB, from the manufacturing process down to the final end use, it is prone to damage such as crushing to the flute structure that may affect performance significantly. In addition, products with different specifications (ie: size, weight or cooling requirements) will require different packaging designs with additional features such as vent holes or perforations. These features will affect the overall mechanical strength of CFB.

It is important to understand the fundamental behaviour of CFB and develop ways to be able to differentiate, characterise and predict how the board behaves when subjected to damage and with addition of features such as creases and perforations. This knowledge will help in achieving good optimal design of CFB boxes for different products.

The path of this project was driven by the main objectives listed as follows:

- Develop an understanding of typical mechanical damage that occurs to CFB and how the morphology of the flute profile changes
- Develop a finite element (FE) model, that implements the micro-geometry of the CFB and apply this to assess its static mechanical strength performance
- Characterise how different levels of damage to CFB impact on the flute morphology and the resulting mechanical strength performance
- Use the actual geometry of damaged CFB samples as a model input to predict mechanical performance and compare these to the experimental data.
- Assess the difference between the available mathematical models that can be applied to CFB, such as analytical solutions, a digitalised flute geometry FE model, a mathematically-described flute geometry FE model and a homogenised flute geometry model of CFB mechanical strength
- Implementing perforations on CFB to understand how the CFB behaves with the addition and how the implementation of perforations in the FE model compares with the experimental findings

1.2. Thesis Structure

This thesis was organised starting by introducing CFB background, current research related to the mechanical damage and assessment of CFB and outlining several potential gaps in this subject in Chapter 2. The rest of the thesis was structured as follows,

	Foundation Work
Chapter 3	*Explored how to describe the changes or damage to the flute morphology by developing a technique to quantify the geometry of the flute.*
Chapter 4	*Development of a micro-geometry FE model that described the flute as an arc-and-tangent curve and applied to important mechanical strength components such as bending stiffness and edge crush test (ECT)*
	Extension from Foundation Work
Chapter 5	*Comparing the change in flute morphology as developed in Chapter 3 with several mechanical strength parameters after CFB was subjected to different extents of crushing.*
Chapter 6	*Combining the foundation work found in Chapters 3 and 4 to assess how the predictions of different mathematical models were affected when CFB was subjected to different extent of crushing.*
Chapter 7	*Adding perforations to the CFB by applying the work from Chapter 3 to assess the effects of perforation to flute geometry and implementing perforations to the FE model developed in Chapter 4*

Finally, the thesis brings down the curtain with concluding remarks and discussion about potential future work.

1.3. Funding and Background

This project was funded by the Ministry of Business, Innovation and Employment (MBIE) with a close connection to Oji Fibre Solutions. The primary goal of this project was to develop a thorough understanding of the strength of CFB and how it is affected by mechanical damage. This project ran parallel with several related projects in the same overall research programme, that focused on developing simplified models to predict packaging design performance that reduce computational time. Part of the aim of this project was also to enlighten the wider programme through providing fundamental understanding of CFB behaviour using the micro-geometry model.

Chapter 2.

Literature Review

Preface

The aim of this chapter is to develop a solid foundation about CFB, discussing the current knowledge related to the objectives as presented in Chapter 1 and identifying potential gaps that can be explored. This chapter starts by introducing the history of CFB and its background, then going more specific into the mechanical testing of CFB and mechanical damage that affects its performance. From here, a gap was identified; to explore the effect of morphological differences in the flute profile on the mechanical performance of CFB. Viable options to address the issue are discussed. Finite element (FE) modelling of CFB is then discussed with approaches to develop such models and potential improvements that can be added. The last section summarises every section in this chapter and explains how everything can be stitched together to develop a novel approach in the research of CFB strength performance.

2.1. Corrugated Fibreboard: Type, Material and Manufacturing

According to the Fibre Box Association (1999), the first known corrugated fibre-based material was patented in 1856 for the production of sweatband linings in tall hats during the period of Victorian Englishman. The unlined corrugated material was first used in 1871 for the packaging of glass and kerosene lamps to protect them from being broken, and three years later, a liner was added on one side of the corrugated paper due to problems with the flute always being stretched. As it became apparent that corrugated board possessed the ability to protect glass and kerosene lamps, the first corrugated box was made in 1894. The corrugated box is still one of the most common materials in the packaging industry today.

As manufacturers demand strong mechanical performance for their packaging products while minimising the quantity of fibre, the design of corrugated layer was ideal. When looking to improve it, designers have come up with a lot of ideas such as adding layers to the fibreboard, optimising the flute shape and even having a selection of materials to be used. With this, different types of CFB were produced and this sub-section presents the different types of commonly used CFB.

2.1.1. Types of Corrugated Fibreboard

CFB consists of two main components which are the liners and the fluting medium. According to Kirwan (2008) and Wright et al. (1992), CFB can typically be classified into four groups (see Figure 2-1); single-lined CFB, single-wall CFB (the most common), double-wall CFB and triple-wall CFB.

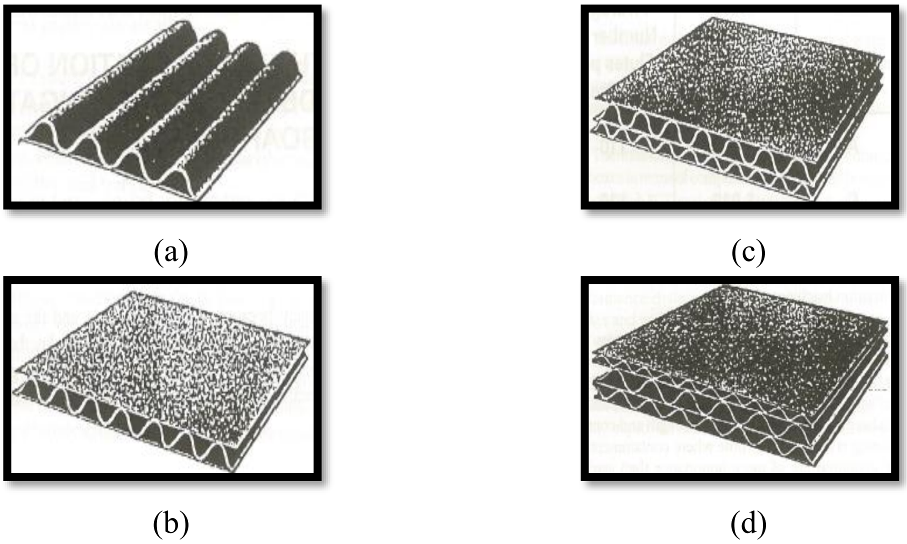

Figure 2-1: Corrugated fibreboard: (a) single faced, (b) single wall, (c) double wall and (d) triple wall. (Source: Wright et al. 1992)

Single-lined (single faced) CFB consists of a liner that is bonded to only one side of the flute. It is commonly used as pads, partitions and to wrap uneven objects as it can be easily curved in the cross machine direction. This type of CFB was dates back to 1874 due to the problem with the flute stretching on the unlined corrugated paper. The addition of a liner ensured that the corrugated shape remained intact.

Single-wall CFB consists of a flute that is sandwiched between two liners. This design improved the strength and performance compared to single-lined CFB and is the most common CFB used in many applications.

Double-wall CFB is made up of two layers of flute that are sandwiched between three liners. This design was made to enhance the strength and ability of the box to protect the goods. Usually, two different types of flute were used such as combining a large flute for strength performance and smaller flute for better graphic capability. If a much stronger board is needed, a triple-wall CFB is used where it consists of three flutes sandwiched between five liners.

2.1.2. *Type of Fluting Medium*

The flute or medium is one of the most critical components in corrugated fibreboard as it contributed a lot in the strength and stiffness through the interaction with liners. For thousands of years, architects have found that arch is the best and strongest way to span a given space. Applying this principle, inventors created the flute that is responsible for resisting bending and pressure from any direction when anchored to the liners (Twede et al., 2014). The flute acts as a cushion that protects the content in the box and serves as an insulator to the contents when there is a sudden change in temperature.

The structure of the flute is defined by its height and pitch (or wavelength) as shown in Figure 2-2 and Table 2-1. The take-up factor is another component of the flute that quantifies the ratio of the length of unfluted geometry to the length of the fluted geometry and defines the amount of paper used for making the flute. Figure 2-3 shows the illustration of the types of flute listed in Table 2-1.

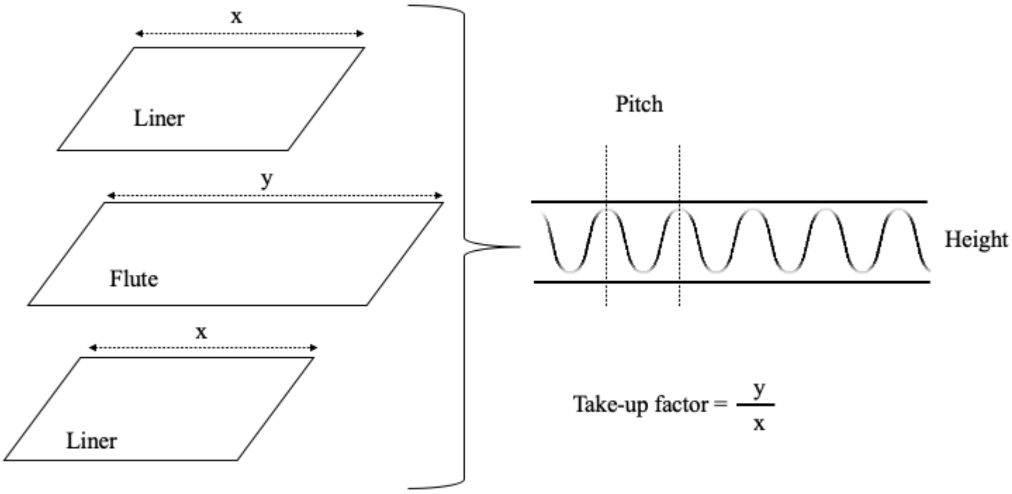

Figure 2-2: Diagram illustrating the height, pitch and take-up factor of corrugated board.

Table 2-1: Corrugated flute types, height, pitch and take-up factor. (Source: Pinnington 2005)

Flute	Height (mm)	Pitch (mm)	Take-Up Factor
A	4.45	8.66	1.53
B	2.50	6.50	1.31
C	3.66	7.95	1.42
E	1.16	3.50	1.24
F	0.75	2.40	1.22

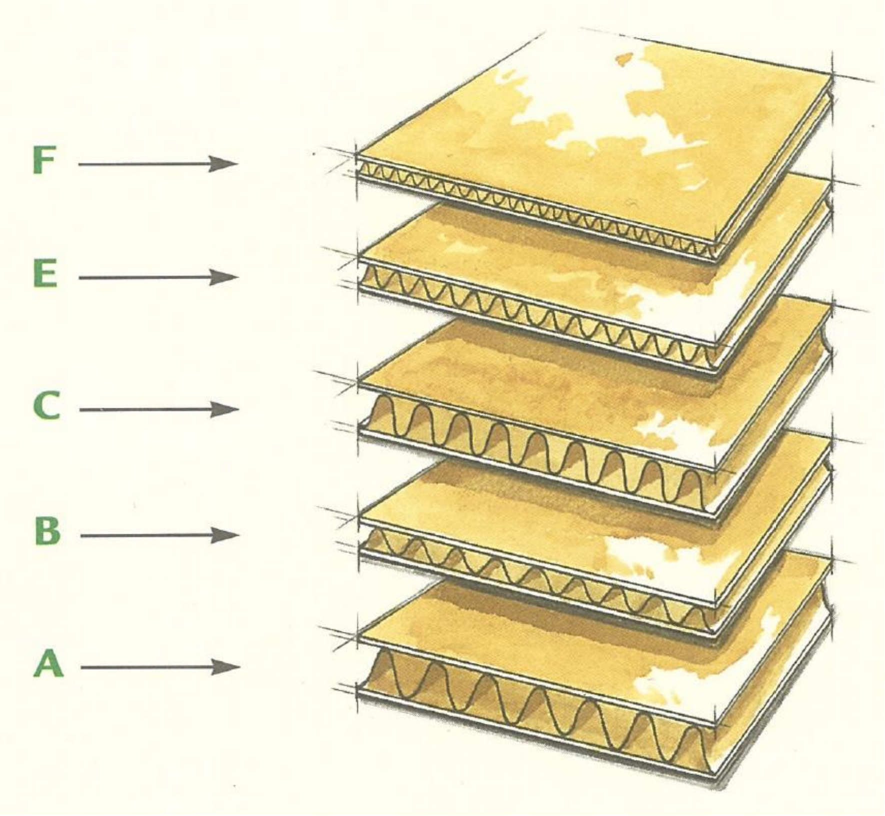

Figure 2-3: Typical types of flute of CFB. (Source: Fibre Box Association, 1999)

A-flute has the highest flute height and pitch which typically makes it the strongest box while B- and C- flutes were made to reduce the amount of flute material at a cost of some strength reduction. According to Paine (2012), E-flute is usually used in display cases and are often combined with high-quality liners. F-flute is used mostly in the fast-food packaging industry as its strength enables it to replace the paperboard using less material (Hanlon et al., 1998).

In addition to these five different flutes, there are many other flutes created for specific purposes and requirements. Larger flutes help to provide more strength and cushioning to the box, while smaller flutes can enhance better printing ability for the packaging. As mentioned in the previous section, different flute profiles may also be combined for a double wall or triple wall CFB. By mixing different flute profiles, the manufacturers can control the strength, stiffness and graphic capability of the board (Lee and Park, 2004). This shows that the flute plays a dominant role in manipulating the properties of the CFB.

2.1.3. Materials used for CFB

The liner is usually chosen to have a smooth surface for graphic and printing purposes as it is difficult to get clear finishes on a rough surface. The liner can also use to absorb and deflect external tension, impact, pressure or bending forces. It is also important for the liners to have an abrasive back side for a firm bond when glued to the tip of flutes. Often, the liner is fabricated in the natural brown colour of Kraft paper or Test liner where the former is often associated with virgin fibres and latter with recycled fibres. However, in some cases, the liner may come in white colour or be coated in another colour depending on the surface finish desired (Finestone and Bloch, 2000). Table 2-2 presents the comparison of some important properties between the Kraft liner and Test liner.

Table 2-2: Properties of Kraft and Test liners as reported from Adamopoulos et al., 2007.

	Kraft Liner	**Test Liner**
Grammage (gm^{-2})	185 – 298	124 – 131
Thickness (mm)	0.258 – 0.437	0.191 – 0.208
SCT in CD ($kN\ m^{-1}$)	4.78	2.32
Bursting Strength (kPa)	937	410

Length of fibres	Long	Short

The Kraft liner is typically superior in strength compared to Test liner as it has a higher grammage (weight of the paper per square metre), short-span compression strength (SCT) in CD and bursting strength due to longer fibres. CD refers to the Cross-machine Direction (perpendicular to the direction of the flute) while MD refers to Machine Direction (parallel to the direction of the flute). Kraft liner is ideal for harsh conditions such as high moisture levels, rough handling or for bulk containers. The Test liner is more suited to mild conditions that do not require extreme demands as it can reduce the cost.

For the flute, the material chosen should have a good stiffness as the flute acts as a cushion to absorb the external forces and flexibility to be shaped into corrugated waves. Commonly, the flute is made up of semi-chemically pulped or recycled-based papers. The semi-chemical paper is often chosen for harsh conditions due to being stronger, while the recycled-based paper is more suited to mild conditions. Table 2-3 summarises the properties for both the semi-chemical paper and recycled-based papers.

Table 2-3: Properties of Semi-chemical paper and Recycled-based papers. (Source: Adamopoulos et al., 2007)

	Semi-chemical	**Recycled-based**
Grammage (gm^{-2})	151 – 172	91 – 111
Thickness (mm)	0.221 – 0.271	0.144 – 0.189
SCT in CD (kN m^{-1})	3.64	1.79
Concora Medium Test (N)	421	187

2.1.4. Manufacturing Process

The process of manufacturing the CFB can be divided into two divisions; the corrugator and converting process. The corrugator involves moisture, glue and heat while the converting involves cutting, shearing and creasing processes (Kline, 1991; Nevins, 2008). Figure 2-4 presents a schematic of the manufacturing process of CFB (Wright et al. 1992).

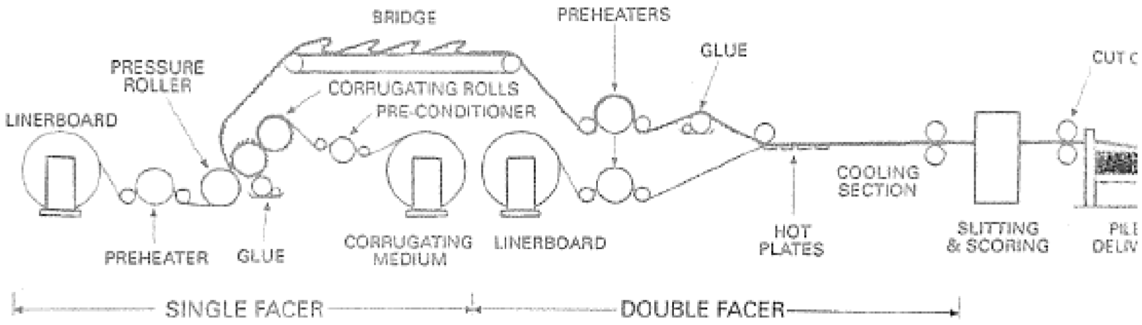

Figure 2-4: Simplified diagram of the manufacturing process of single-wall corrugated fibreboard. (Source: Wright et al. 1992).

Single Facer

The corrugator is the process to combine the flute with the liners and consists of the single facer and the double facer. First, the single facer will pull both the liner and flute via the preheater and preconditioner from the roll stand at the same time. The contact area around each roll stand can be adjusted to control the temperature and moisture content. This can also be controlled using a disk brake or steam shower. The addition of disk brake and steam shower to the manufacturing process are essential as the resultant structure is likely to curl if there is a large difference in the temperature and moisture content of the liner and flute (Kline, 1991).

After the flute has passed through the preconditioner, it will cross between two corrugating rolls where the flute profile is created by the intermeshing teeth across the surface of the rolls. The contorted space between the two corrugating rolls is called the labyrinth. As the flute enters the labyrinth, it is sprayed with steam to heat and moisten the flute. Then the flute is held up against the second corrugated roll which passes through the glue applied to the outer tips of the flute. The flute is then adhered to the liner through the pressure roller which is controlled by two hydraulic pistons. The pressure used is monitored to ensure that the flute is not crushed but is strong enough so that the flute can bond well with the liner.

Double Facer

After the liner and flute are combined, the single-faced board then passed through the bridge to allow some time for the glue to dry up and form a permanent bond between them. Here the single-faced board forms a festoon shape with the conveyer belts running at a slow speed to increase the time on the bridge. At the end of the bridge, the single-faced board is pulled by a rubber coated roller to the next stage of the preheater to prepare them for bonding with another liner. The preheated single-faced board then passed through the glue station where the glue is applied to the other face of the flute tips. After the glue application, the single-faced board is bonded to a new liner at the double backer. The single-wall board then passed through hot plates to cure the glue. The single-wall board is then sent to cool down along the cooling section.

Converting

After the curing process, the single-wall board then passes through the converting process where it is transformed into individual sheets or blanks. The converting consists of rotary shearing, slitting, scoring and finally stacking.

The rotary shearing is the process which cuts the board into desired MD length. Then it passes through the slitting process which cuts them into desired CD length. After that, the blanks go through the scoring process in which creases are formed to allow folding of the blanks after converting (into a box). Finally, they are stacked together and transferred for further developments such as printing, hole cutting and perforating process (converting).

2.2. Standard Mechanical Testing of CFB

There are many organisations that have published standards and methods for testing CFB such as American Society for Testing and Materials (ASTM), The International Organization for Standardization (ISO) and Technical Association of the Pulp and Paper Industry (TAPPI). In this thesis, the TAPPI version of standards were used it has more standards & methods related to CFB performance plus is well recognised across the industry of corrugated packaging.

2.2.1. Conditioning and Sampling

Before the start of any mechanical testing of paper products, it is important to precondition and condition them to ensure that the test results will not be affected by the ambient conditions. TAPPI T-402 SP-08 describe the methodology where, in summary, the materials should be preconditioned at 10-35% relative humidity (RH) and 22-40°C for a minimum of 24 hours. Then the materials should be conditioned at 50% ± 2% RH and 23°C ± 1°C for enough time for them to reach equilibrium with the atmosphere. This can be about 5-8 hours for unsealed boxes, 16 hours for sealed boxes and 72 hours for boards made of heavy substances or wax treated.

Sampling standard TAPPI T-400 describes the procedure to obtain a representative sample from the CFB for testing. This explains how to select and take care of the samples and reporting the results.

2.2.2. *Box Mechanical Testing*

Mechanical testing of CFB can be divided into static and dynamic tests. Example static tests are the box compression test (BCT), bending resistance test and edge crush test (ECT) while examples of dynamic tests are the drop test, inclined impact test and vibration tests. In this thesis, the interest was only on the static test to understand the CFB performance at a local level.

BCT follows the TAPPI T-804 om-06 standard, where the box is placed between two platens and crushed until failure. The results are reported in Newtons (N). McKee et al. (1963) reported a semi-empirical equation to predict the BCT using the bending stiffness, ECT and perimeter of a CFB box. This equation is widely used across the corrugated industry and is still used today. A more simplified McKee's formula that substitutes the bending stiffness with the board thickness is most commonly used by practitioners, but this overestimates the original McKee's formula (Popil, 2017).

The bending stiffness of CFB can be measured following the TAPPI T-820 cm-09 standard where a four-point loading method is applied with measurement of the force and the centre deflection of the sample. Samples should be prepared along MD and CD to obtain the bending stiffness in both directions. The results are reported in N.m. TAPPI T-836 om-13 is another standard used to measure the bending stiffness of CFB by clamping the sample at each end and leaving a free span in the centre. A force is applied at both clamps causing the sample to bend, and the maximum deflection is measured and used for calculating the bending stiffness. The bending stiffness experiment in this thesis were conducted based on TAPPI T-820 cm-09 standard due to equipment availability and simplicity to model.

There are several standards for measuring the ECT performance of CFB such as TAPPI T-811 om-17 (short column test), TAPPI T-838 cm-12 (neckdown method), TAPPI

T-839 om-18 (clamp method) and the TAPPI T-841 om-07 (Morris method). Popil (2012) compared the difference between TAPPI T-811 om-17, T-838 cm-12 and T-839 om-18 against their predicted values and showed that TAPPI T-839 om-18 had the largest deviation. TAPPI T-811 om-17 is known as the official method for ECT (Fibre Box Association, 1999), hence the ECT work in this research was based on this standard.

2.2.3. Paper Component Mechanical Testing

The paper components that made up the CFB are also subjected to mechanical testing to determine its performance. Paper is mainly characterised in terms of their basis weight or grammage which is measured following the TAPPI T-410 standard. This is also reported in Table 2-2 and Table 2-3. There are many different types of mechanical test such as burst strength test (TAPPI T-807), compressive strength test (commonly TAPPI T-826), Concora medium test (TAPPI T-809) and tensile strength test (TAPPI T-494).

Compressive strength test results can be used to predict the ECT (Popil, 2012), while the tensile strength test results can be used to predict the bending stiffness (Nordstrand, 1995). The compressive strength of the paper components can be measured following the TAPPI T-818 (ring crush test), TAPPI T-822 (ring crush test with rigid support method) and TAPPI T-826 (short span compressive strength or also known as STFI from the method's developer). The compressive stress results are expressed in kN.m^{-1}. The tensile test following TAPPI T-494 is done using a constant rate of elongation until the tensile breaking point. The tensile stress and stiffness results are expressed in kN.m^{-1}.

2.3. Damage to CFB

Damage to CFB box can be defined as anything that weakens the performance of the box. It may happen anytime and anywhere, even during the manufacturing process, and weakens the box which increases the risk of damaging the goods. While some damage is hard to avoid, it is important to minimise it in order to preserve the strength of CFB. This subsection will look at the factors affecting the performance of CFB and damage to the flute profile of CFB.

2.3.1. Factors Affecting the Performance of CFB

As presented in Figure 2-5, the CFB performance may be affected anywhere from the materials used, the conversion process (converting the CFB into a box) and use conditions. These three classes are used based on the lifecycle of the CFB.

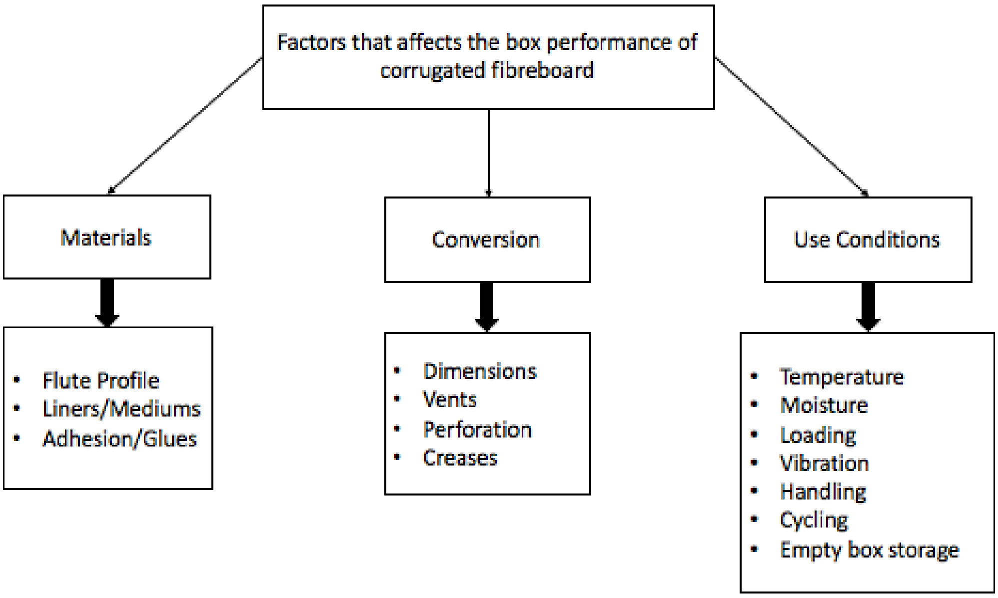

Figure 2-5: Factors that can affect the performance of CFB throughout its lifecycle.

Selection of materials such as the type of paper, flute size and adhesion type correspond to the quality of the CFB. It was shown these criteria provided significant impact on the properties of the CFB especially in terms of its mechanical strength (Adamopoulos et al., 2007; Lee and Park, 2004; Snyder, 1990). The combination of paper that made up the CFB is crucial since both liners and flutes will have their own specific target as discussed in section 2.1.3.

CFB also may be subjected to damage during the manufacturing process. The first part of the process involves moisture and temperature control which can significantly affect the properties of the paper if it is not well controlled (Frank, 2014). Allaoui et al. (2009) explained that a high water content can break the bonds between the cellulosic fibres while Youn et al. (2007) reported that a low moisture can cause cracking on the paper especially during scoring or creasing operations. The CFB then experiences more damage from the conversion process where they are slitted, scored and slotted, however, most of this damage is done intentionally to meet the requirements of the finished box.

The end-use conditions generally cover anything related to the condition of CFB from the end of manufacturing process until it reach the end users. The temperature and moisture are not only important during the manufacturing process, but also throughout the lifecycle of the CFB whether in storage or during transport. Zhang et al. (2011) reported that the BCT degraded by half just due to the impact of temperature and moisture content during storage. Other factors such as loading, vibration, handling and cycling should be expected during transportation and will result in damaging the CFB which can decrease its shelf life (Berardinelli et al., 2003).

These unavoidable damages are the reason why mechanical performance tests are important to ensure that the box can survive in extreme conditions.

2.3.2. Flute Profile Damage

The flute of CFB is one of the most critical components in providing the overall strength and stiffness while also minimising the amount of fibre used due to its corrugated structure. All three classes of factors that affect the performance of CFB explained in Figure 2-5 share a feature of damaging the flute profile in some way. The damage to the flute profile can either be done intentionally or unintentionally as described in Figure 2-6.

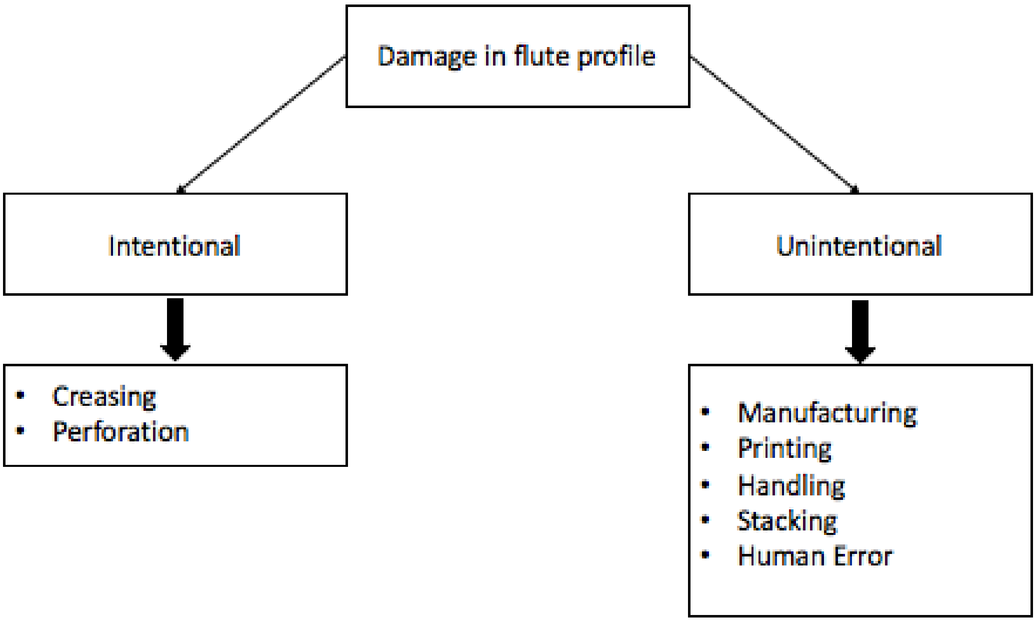

Figure 2-6: Factors that damage the flute profile of CFB.

Intentional damage usually done during the conversion process such as creasing, perforation and slotting vent holes. While this type of damage is unrecoverable, it aims to increase the quality of the board in some other way, such as ease of folding with crease lines and ease of handling with hand holes (Nygårds et al., 2009).

Conversely, there are accidental unwanted damages to the flute profile that may happen anywhere between the manufacturing process through to the end use, such as crushing of flute due to blank stacking, printing and during the handling of the box. This damage will weaken the stiffness properties of the board and allows failure to propagate quickly from the localised failure area on the board. To date, there are limited studies on the structural damage to the flute.

Damage to the structure of the flute will weaken the performance of the board which provides the opportunity to understand and measure the performance through the morphological changes of the flute.

2.4. Image Analysis

To understand and analyse the structural changes on the flute profile of CFB, it is important to develop a good understanding on ways to obtain it. There are several ways to approach this problem such as by simply imaging the edge section of CFB, using a through-thickness 3D scanner and cutting the mid-plane section of the board to analyse the flute structure. This section presents recent findings around this approach and possible options to achieve it.

2.4.1. Imaging the Edge Section of CFB

The simplest way to obtain the flute profile of CFB is through imaging the edge of the board as demonstrated by Nagasawa et al. (2013) and Thakkar et al. (2008) in showing the impact of creasing on CFB, and Biancolini (2005) in comparing the effect of different shapes of flute profile. In particular, Biancolini (2005) showed that the flute profile changes after it leaves the corrugator, after conversion and after case erection. By importing the image of the flute profile to a FE model he showed that the bending stiffness of the different flute profile were different.

It could be argued that their analysis is only valid for what happens at the edge of the board and it is likely that the damage to the flute profile at the edge of the board is different compared to the mid-plane. However, it is challenging to characterise the flute shape at the mid-plane since they are not optically accessible. To be able to do this, a through-thickness 3D scanner may be used or by slicing the mid-plane section of the board without causing indentation damage.

2.4.2. *Through-thickness 3D-scanner*

The through-thickness 3D scanner uses a volumetric technique with the help of x-ray computerised technology that can generate a 3D image of the inside of an object. X-ray computerised technology is a non-destructive imaging technique with the objective to use attenuation of x-rays to reconstruct a slice through an object. Classical x-ray radiography faces a problem where it creates superimposed internal features of the object on the final image, however, in computed technology (CT), this problem was avoided by capturing the projections at many angles and the images are stacked together to create a 3D version of the object.

CT is primarily used for medical purposes but has also been used on homogenous materials such as composites, plastics and rocks. Evans et al. (2015) applied this technique to analyse carbon fibre composite – copper (CFC-Cu) monoblock and used the 3D image for finite element (FE) modelling. The results showed that the imported 3D image was better than traditional CAD modelling by providing finer resolution at the interface between CFC and Cu.

Frisullo et al. (2010) investigated different types of biscuits and breadsticks where the findings showed that the CT technology enabled the measurement of size, shape and the distribution of various phases and networking of the samples which is not possible with 2D imaging. The same findings was also observed by Centea and Hubert (2011) where they found that the technology allowed them to evaluate the void content, distribution and morphology of composite materials that were impregnated.

Eriksson et al. (2014) analysed the damage on carton board box through the same technology which was able to capture the 3D image of the whole box with damage such as creases and delamination. These studies showed that even though thickness 3D scanning is a viable approach to obtain the flute profile of CFB, it is expensive and time-consuming.

2.4.3. Potential ways of cutting the mid-plane of CFB

As suggested by Biancolini (2005), since analysing the mid-plane of CFB can be difficult as it is not optically accessible, using a cutter to carefully cut parts of the board to obtain the internal flute profile may be a viable approach. In doing so, it is important to avoid damaging the flute profile (through damage like indentations) when cutting as it will change the geometrical features.

Mechanical cutters are often chosen as they are cheap, simple to maintain and easy to use (Happonen et al., 2015). Some examples include cardboard scissors, cardboard knives and die cutters. Mechanical cutters cut the board by applying shear force and create a local deformation until fracture propagates and separates the object (Mahvash et al., 2007). Nagasawa et al. (2011) showed that the indentation deformation as a result from being mechanically cut was significant and changes the structure of the flute profile of CFB.

Another technology that can be applied to cut CFB is a laser cutter which is widely known for cutting metallic materials, especially in laser welding and hybrid welding for cutting steel (Salminen, 2010). The laser cutter cuts the materials through vaporisation. The laser beam heats up the material to its evaporation temperature and sublimates it (Piili, 2009). Malmberg et al. (2006) showed that the laser cutter produced a higher quality paperboard edge than using a mechanical cutter by comparison of Scanning Electron

Microscopy images. The layers of the paperboard showed indentation deformation as a result of the mechanical cutting while through laser cutting, a smooth edge was observed on the layers of the paperboard. This suggest that using laser cutter may avoid forming indentations on CFB and may be used to cut the mid-plane of CFB and describe the flute profile at that region.

2.5. Finite Element (FE) Modelling of CFB

There are three commonly used ways to study the performance of a homogeneous materials which are the analytical approach, numerical approach and experimental work. As Biancolini and Brutti (2003) explained, nowadays, analytical approaches have been substituted with more advanced numerical solutions such as FE models which can explain the micro-mechanical behaviour of the corrugated fibreboard while also having the ability to control the input parameters.

There have been several studies reporting the finite element modelling of CFB (Allanson and Svard, 2001; Aboura et al., 2004; Haj-Ali et al., 2009; Fadiji et al., 2018). In the context of this research, a FE model could be used to understand the geometrical changes of the flute and potentially include additional features to the model such as hand holes, vent holes and perforations. This section presents the current literature by summarising the approach of modelling the geometry of CFB, material behaviour and gaps to add features to the model.

2.5.1. Geometry of the CFB

The flute shape in CFB resembles a sinusoidal curve which can mathematically be described by the pitch and amplitude. However, Urbanik (2001) argued that an arc and tangent curve describe the geometry of the flute more accurately as it accounts for the right take-up factor as opposed to sinusoidal, elliptical and trapezoidal shapes. By using this method, the flute calliper (h_f *– represent as H in the figure*), pitch (P) and take-up ratio (α) of the flute are needed as the input parameters to get the flute tip (R), length of the flank

(L) and the angle of the flank (β). The geometrical representation with the parameters is shown in Figure 2-7.

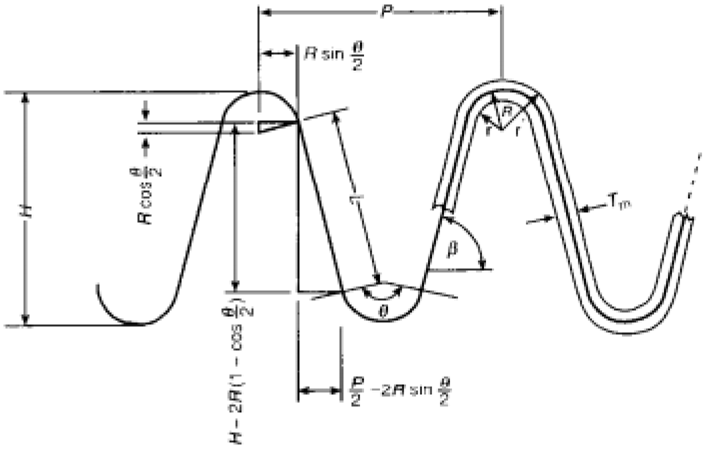

Figure 2-7: Arc-and-tangent model as proposed by Urbanik to characterise the flute of CFB.(Source: Urbanik, 2001).

First, the angle of the flank, β, is calculated as shown in equation (2.1) by having an initial estimation of β = 1 and improving the estimation through running a series of iterations until convergence is reached.

$$\beta = sin^{-1}\left[\frac{\left(2\beta\left({}^{h_f}/_{P}\right) - \alpha - 1\right) cos\beta + \alpha + 1}{\beta + 2({}^{h_f}/_{P})}\right] \tag{2.1}$$

Once the value of β is obtained, the radius of the curve on the flute is calculated using equation (2.2):

$$R = \frac{\alpha - \sec\beta}{4P(\beta - tan\beta)} \tag{2.2}$$

By getting R, the length of the flank on the flute is then calculated (equation 2.3).

$$L = R\left[\frac{h_f - 2R(1 - cos\beta)}{Rsin\beta}\right] \tag{2.3}$$

The liners can then be sandwiched between the generated flute geometry to create a CAD model of CFB that can then be used in FE simulation software such as Ansys and Abaqus for modelling purposes. The bonding between the liners and flute can be assumed to be a perfect bond constraint such as reported by Thakkar et al. (2008), Nagasawa et al. (2013), Haj-Ali et al. (2009) and Åslund et al. (2014).

2.5.2. Material Behaviour of CFB

Orthotropic means three orthogonal axes of symmetry in material properties, and are typically different in each of the directions. Orthotropic behaviour is known as a subset of anisotropic materials where the properties change with the direction of the axis. Such example of anisotropic materials are paper and composite materials, however, many researchers assumed the behaviour as orthotropic when carrying out research on the mechanical strength and proven this to be a simpler model with reasonable accuracy (Aboura et al., 2004; Allansson and Svärd, 2001; Haj-Ali et al., 2009). With an orthotropic behaviour, fewer properties are needed, which reduces the complication in developing the model.

In linear-elastic and orthotropic materials, the main material properties are the elastic modulus, shear modulus and Poisson’s ratio in the three main axes. For paper, these axes are the MD, CD and ZD (thickness direction). The elastic modulus in the MD and CD directions, E_{11} and E_{22}, can be measured through a tensile test such as per TAPPI T-494. Since the elastic modulus in ZD, E_{33}, is difficult to measure as paper is a thin material, researchers have approximated it as $E_{MD}/200$ (Fadiji et al., 2018; Gooren, 2006; Sirkett et al., 2007). The in-plane Poisson's ratio, v_{12}, can be determined by the ratio of the change in axial length to the change in the longitudinal length in compression or tension. Both the out-of-plane Poisson's ratio, v_{13} and v_{23}, are difficult to measure since paper is thin, hence it is typically assumed as in plane stress condition with small numbers of 0.01 assigned (Nordstrand, 1995). The in-plane shear modulus, G_{12}, follows the Baum's approximation as shown in Table 2-4 (Baum et al., 1982). This has been shown as an acceptable approximation for G_{12} by many researchers (Aboura et al., 2004; Haj-Ali et al., 2009). Empirical approximations for G_{13} and G_{23} in equation (2.6) and (2.7) were reported by Beldie (2001) and have been validated by many researchers (Allansson and Svärd, 2001; Fadiji et al., 2018; Gooren, 2006).

Table 2-4: Parameter estimation for FE model input.

Variables	Formula	Eq No.	Reference
E_{33}	$\frac{E_{11}}{200}$	(2.4)	Gooren, 2006
G_{12}	$0.387\sqrt{E_{11}.E_{22}}$	(2.5)	Baum et al., 1982
v_{12} & v_{13}	0.01	-	Nordstrand, 1995
G_{13}	$\frac{E_{11}}{55}$	(2.6)	Beldie, 2001
G_{23}	$\frac{E_{22}}{35}$	(2.7)	Beldie, 2001
σ_{33}	$\frac{4}{\sigma_{11}^2\sigma_{22}^2} > \left[\frac{1}{\sigma_{33}^2} - \left(\frac{1}{\sigma_{11}^2} + \frac{1}{\sigma_{22}^2}\right)\right]^2$	(2.8)	Beldie, 2001
σ_{11c}	$0.6\ \sigma_{11t}$	(2.9)	Nordstrand, 2004
σ_{22c}	$0.6\ \sigma_{22t}$	(2.10)	Nordstrand, 2004
τ_{12}	$\sqrt{\sigma_{11c}.\sigma_{22c}}$	(2.11)	Biancolini et al., 2009

where G refers to shear modulus (GPa), τ refers to shear stress (MPa), subscripts 3 is the direction that aligns with the thickness and c refers to measured values under compression.

Aside from the elasticity parameters, orthotropic materials also have stress limit parameters that define the yield point of the materials. The stress limit parameters can be divided into the maximum tensile stress, maximum compressive stress and maximum shear stress in the three orthogonal axes directions. Similarly, the maximum tensile stress in MD and CD, σ_{11t} and σ_{22t}, can be measured from the tensile test according to TAPPI T-494. Other variables can be calculated based on σ_{11t} and σ_{22t} as shown in Table 2-4. The out-of-plane stress, σ_{33}, relation in equation (2.8) was reported by Beldie (2001) and validated by Haj-Ali et al. (2009). It was reported that maximum compressive stress, σ_{11c} and σ_{22c}, can be assumed to be 60% of the measured maximum tensile stress following typical stress ratios reported in the literature (Haj-Ali et al., 2009; Nordstrand, 2004). The maximum shear stress, τ_{12}, was reported to follow the empirical equation (2.11) (Biancolini et al., 2009). Haj-Ali et al. (2009) followed the transverse shear stress, τ_{13} and τ_{23}, values reported from Beldie (2001) which were both 0.024 MPa with the results showing a good overall prediction between the model and the experiment for ECT. These values are good approximates to begin FE model development.

2.5.3. Inclusion of additional features

Additional features like hand holes, vent holes and perforations may also be added to CFB boxes as they can enhance the box features. Hand holes are usually seen on the top part on the side of the box and allow ease of carrying, especially for the users. Vent holes are typically seen on boxes in the food industry as they are designed to allow air to pass through the box to accelerate the cooling of the contents or maintain the conditions. Perforations involve cutting a series of holes in a line on a box to make it easier to tear them apart. Perforations are used for shelf-ready packaging where the retailers can easily tear the face of the box and directly place it on the shelf for display and sales.

Even though these additional features will most probably reduce the mechanical strength, it is desirable in some cases as it optimises other features. However, it is important to understand how the additional features affect the strength of the box as it can be a safety issue in manual handling if the design does not meet the appropriate strength requirements (Singh et al., 2008). Several studies have been conducted on determining the impact of hand holes and vent holes on the compression strength of CFB by looking at parameters such as the shape, location and size of the holes (Berry et al., 2017; Han and Park, 2007; Singh et al., 2008). In particular, Han and Park (2007) and Berry et al. (2017) showed that the optimal design can be achieved through the understanding obtained using FE simulation.

For perforations in CFB, there is currently only limited studies applying FE simulation to assess the problem. Jiménez-Caballero et al. (2009) suggested simulating the perforated holes on box using connector elements along the unconnected node lines. With this technique, it can save more time as the holes are represented by a connected line instead. However, their model used a simplified laminated model instead of the actual corrugation structure of the flute. Furthermore, there were no results presented to justify the approach as a validated solution. Part of this study will be looking at simulating the finite element model of CFB with perforations and compare it with experimental findings.

2.5.4. Strength performance test

As discussed in Section 2.2.2, BCT is closely related to the bending stiffness, ECT and the perimeter of the box. As this project is interested in understanding the box strength performance at a local level, the FE model should be developed on the bending stiffness test and ECT of CFB. The development of the model will follow the standard methods TAPPI T-811 CM-09 for four-point loading and TAPPI T-811 OM-17 for the ECT.

2.6. Summary

The objectives of this project were presented in Chapter 1 and this chapter was written to identify the available tools and findings while developing a foundation of potential ways to tackle the problems. This chapter also presented potential gaps in the study of the strength of CFB for novel research to be conducted as part of this PhD.

From Section 2.1, an in-depth understanding of the history, manufacturing and important aspects of CFB was presented. This section also reviewed the types of CFB available in the market and how they differ from one another.

Section 2.2 presented the important components contributing to the static mechanical strength of the CFB box and the constituent paper materials. This section outlined the standard procedures and the processes for sample preparation before conducting the experimental tests.

In Section 2.3, a discussion was presented to understand the factors that can affect the performance of CFB. Flute profile was found to be a critical component in affecting strength. In this section, the damage on flute profile was divided into intentional and unintentional damage. Unintentional damage such as crushing, is always unavoidable and unpredictable, hence there is a potential gap to find out a way to understand this damage and its impact on CFB performance.

In Section 2.4, an overview of the available and current technology of image analysis was discussed. The main interest was to find out how to visualise the flute profile of CFB at the mid-plane region. A viable approach is to cut thin strip on the board using a laser cutter as it avoids indentation deformation on the material. The flute profile can potentially be analysed further by describing the geometrical changes due to damage.

In Section 2.5, a brief overview on FE modelling of CFB was presented where the section discussed about how to replicate the actual flute geometry, assumptions of CFB behaviour and important material properties to describe the behaviour. This section also looked at the next step to improve the model by ading additional features and found a gap in that there are limited studies conducted on modelling the perforation of CFB.

Different shaped flute profiles can be digitalised and feed into a FE model that can then simulate their mechanical performance. This allows for modelling the actual flute geometry of CFB.

Reference

Aboura, Z., Talbi, N., Allaoui, S., & Benzeggagh, M. (2004). Elastic behavior of corrugated cardboard: experiments and modeling. Composite structures, 63(1), 53-62.

Adamopoulos, S., Martinez, E., & Ramirez, D. (2007). Characterization of packaging grade papers from recycled raw materials through the study of fibre morphology and composition. Global NEST Journal [9], 20, 28.

Allansson, A., & Svärd, B. (2001). Stability and Collapse of Corrugated Board-Numerical and Experimental Analysis. (Master's Thesis). Lund University, Sweden 2001

Allaoui, S., Aboura, Z., & Benzeggagh, M. (2009). Effects of the environmental conditions on the mechanical behaviour of the corrugated cardboard. Composites Science and Technology, 69(1), 104-110.

Åslund, P. E., Hägglund, R., Carlsson, L. A., & Isaksson, P. (2014). Modeling of global and local buckling of corrugated board panels loaded in edge-to-edge compression. Journal of Sandwich Structures and Materials, 16(3), 272-292.

Fibre Box Association (1999). The Fiber Box Handbook. Chicago, IL.

Baum, G. A., Habeger Jr, C. C., & Fleischman Jr, E. H. (1982). Measurement of the orthotropic elastic constants of paper. The Institute of Paper Chemistry, Wisconsin, USA.

Beldie, L. (2001). Mechanics of paperboard packages: performance at short term static loading. Licentiate Dissertation. Lund University, Sweden

Berardinelli, A., Donati, V., Giunchi, A., Guarnieri, A., & Ragni, L. (2003). Effects of transport vibrations on quality indices of shell eggs. Biosystems Engineering, 86(4), 495-502.

Berry, T. M., Fadiji, T., Defraeye, T., & Opara, U. L. (2017). The role of horticultural carton vent hole design on cooling efficiency and compression strength: a multi-parameter approach. Postharvest Biology and Technology, 124, 62-74.

Biancolini, M. E. (2005). Online quality control of corrugated board panel by image processing. International Journal of Computer Applications in Technology, 23(2-4), 157-165.

Biancolini, M. E., & Brutti, C. (2003). Numerical and experimental investigation of the strength of corrugated board packages. Packaging Technology and Science, 16(2), 47-60.

Biancolini, M. E., Brutti, C., & Porziani, S. (2009). Experimental Characterisation of Paper for Corrugated Board. Paper presented at the Proceedings, Sixth International Symposium: Moisture and Creep Effects on Paper, Board and Containers, Madison, Wisconsin, USA.

Centea, T., & Hubert, P. (2011). Measuring the impregnation of an out-of-autoclave prepreg by micro-CT. Composites Science and Technology, 71(5), 593-599.

Eriksson, D., Korin, C., & Thuvander, F. (2014). Damage to carton board packages subjected to concentrated loads. In 19th IAPRI World Conference on Packaging, Melbourne, Australia, June 15-18, 2014 (pp. 172-182).

Evans, L.M., Margetts, L., Casalegno, V., Lever, L.M., Bushell, J., Lowe, T., Wallwork, A., Young, P., Lindemann, A., Schmidt, M. and Mummery, P.M. (2015). Transient thermal finite element analysis of CFC–Cu ITER monoblock using X-ray tomography data. Fusion Engineering and Design, 100, 100-111.

Fadiji, T., Ambaw, A., Coetzee, C. J., Berry, T. M., & Opara, U. L. (2018). Application of finite element analysis to predict the mechanical strength of ventilated corrugated paperboard packaging for handling fresh produce. Biosystems Engineering, 174, 260-281.

Finestone, A. B., & Bloch, G. (2000). Cardboard and corrugated board container having laminated walls. U.S. Patent No. 6,083,580. Washington, DC: U.S. Patent and Trademark Office.

Frank, B. (2014). Corrugated box compression—a literature survey. Packaging Technology and Science, 27(2), 105-128.

Frisullo, P., Conte, A., & Del Nobile, M. (2010). A Novel Approach to Study Biscuits and Breadsticks Using X - Ray Computed Tomography. Journal of Food Science, 75(6), E353-E358.

Gooren, L. (2006). Creasing behaviour of corrugated board *(Master's Thesis)*. Eindhoven University of Technology, Eindhoven, the Netherlands.

Haj-Ali, R., Choi, J., Wei, B.-S., Popil, R., & Schaepe, M. (2009). Refined nonlinear finite element models for corrugated fiberboards. Composite Structures, 87(4), 321-333.

Han, J., & Park, J. M. (2007). Finite element analysis of vent/hand hole designs for corrugated fibreboard boxes. Packaging Technology and Science, 20(1), 39-47.

Hanlon, J. F., Kelsey, R. J., & Forcinio, H. (1998). Handbook of package engineering (3rd ed.). Technomic Publishing, Lancaster

Happonen, A., Stepanov, A., & Piili, H. (2015). Feasible Application Area Study for Linear Laser Cutting in Paper Making Processes. Physics Procedia, 78, 174-181.

Jiménez-Caballero, M., Conde, I., García, B., & Liarte, E. (2009). Design of different types of corrugated board packages using finite element tools. Paper presented at the SIMULIA Customer Conference.

Kirwan, M. J. (2008). Paper and paperboard packaging technology. Blackwell Publishing Ltd.

Kline, J. E. (1991). Paper and paperboard: manufacturing and converting fundamentals. Backbeat Books.

Lee, M. H., & Park, J. M. (2004). Flexural stiffness of selected corrugated structures. Packaging Technology and Science, 17(5), 275-286.

Mahvash, M., Voo, L., Kim, D., Jeung, K., Wainer, J., & Okamura, A. M. (2007). Modeling the forces of cutting with scissors. IEEE Transactions on Biomedical Engineering, 55(3), 848-856.

Malmberg, H., Leino, K., & Kujanpää, V. (2006). Laser cutting of paper and board (ILACPaper): Lappeenranta University of Technology, Finland.

McKee, R., Gander, J., & Wachuta, J. (1963). Compression strength formula for corrugated boxes. Paperboard Packaging, 48(8), 149-159.

Nagasawa, S., Fujikura, M., Fukuzawa, Y., & Kajizuka, T. (2011). Deformation behavior of corrugated medium during wedge indentation into heightwise corrugated. Journal of Packaging Science and Technology, 20(4), 283-292.

Nagasawa, S., Komiyama, Y., & Mitsomwang, P. (2013). Finite element analysis of corrugated board on rotary creasing process. Journal of Advanced Mechanical Design, Systems and Manufacturing, 7(2), 103-114.

Nevins, A. (2008). Significant factors affecting horticultural corrugated fibreboard strength *(Doctoral Dissertation)*. Massey University, Palmerston North, New Zealand.

Nordstrand, T. (1995). Parametric study of the post-buckling strength of structural core sandwich panels. Composite Structures, 30(4), 441-451.

Nordstrand, T. (2004). On buckling loads for edge-loaded orthotropic plates including transverse shear. Composite Structures, 65(1), 1-6.

Nygårds, M., Just, M., & Tryding, J. (2009). Experimental and numerical studies of creasing of paperboard. International Journal of Solids and Structures, 46(11), 2493-2505.

Paine, F. A. (2012). The packaging user's handbook. Springer Science & Business Media.

Piili, H. (2009). Characterization of interaction phenomena of laser beam and paper materials in cutting. Licentiate of Science Study, Lappeenranta University of Technology, Finland.

Pinnington, T. (2005). The Corrugated Industry: In Pursuit of Excellence. Michael Brunton.

Popil, R. (2012). Overview of recent studies at IPST on corrugated board edge compression strength: Testing methods and effects of interflute buckling. BioResources, 7(2), 2553-2581.

Popil, R. E. (2017). Physical Testing of Paper. Smithers Pira.

Salminen, A. (2010). The filler wire-laser beam interaction during laser welding with low alloyed steel filler wire. Mechanika, 4(84), 67-74.

Singh, J., Olsen, E., Singh, S., Manley, J., & Wallace, F. (2008). The effect of ventilation and hand holes on loss of compression strength in corrugated boxes. Journal of Applied Packaging Research, 2(4), 227.

Sirkett, D., Hicks, B., Berry, C., Mullineux, G., & Medland, A. (2007). Finite element simulation of folding carton erection failure. Proceedings of the Institution of Mechanical Engineers, Part C: Journal of Mechanical Engineering Science, 221(7), 753-767.

Snyder, P. A. (1990). Starch-based corrugating adhesive containing fibers. U.S. Patent No. 4,941,922. Washington, DC: U.S. Patent and Trademark Office.

Thakkar, B. K., Gooren, L. G. J., Peerlings, R. H. J., & Geers, M. G. D. (2008). Experimental and numerical investigation of creasing in corrugated paperboard. Philosophical Magazine, 88(28-29), 3299-3310.

Twede, D., Selke, S. E., Kamdem, D.-P., & Shires, D. (2014). Cartons, crates and corrugated board: handbook of paper and wood packaging technology. DEStech Publications, Inc.

Wright, P., McKinlay, P., & Shaw, E. (1992). Corrugated Fibreboard Boxes. Ed. Amcor Fibre Packaging.

Youn, H.-J., Lee, H.-L., Chin, S.-M., & Choi, I.-S. (2007). Physical properties of linerboard and corrugated fiberboard at the cyclic condition of low humidity. Journal of Korea Technical Association of the Pulp and Paper Industry, 39(2), 38-44.

Zhang, Y.-l., Chen, J., & Wu, Y. (2011). Analysis on hazard factors of the use of corrugated carton in packaging low-temperature yogurt during logistics. Procedia Environmental Sciences, 10, 968-973.

Chapter 3.

Characterising Morphological Damage of Corrugated Fibreboard Flute Geometry

---

Preface

In this chapter, an image processing algorithm is developed that can quantify the morphological difference between different flute profiles of CFB, specifically in the mid-plane of the board which is not optically accessible. As the flute profile of CFB is correlated closely to the mechanical strength of CFB (presented in Chapter 2), it is important to develop a good and sound characterisation method. This chapter mainly involves validating this technique and demonstrating its ability in real-world applications. The outcome from this chapter enables the differentiation of the morphology of the flute profile through a quantifiable variable called the 'similarity factor'.

The work from this chapter was published:

Jamsari, M. A., Kueh, C., Gray-Stuart, E., Martinez-Hermosilla, G. A., Dahm, K., & Bronlund, J. E. (2019). A technique to quantify morphological damage of the flute profile in the midplane of corrugated fibreboard. Packaging Technology and Science, 32(5), 213-226.

The work from this chapter has also been presented in the following conference:

Jamsari, M. A., Kueh, C., Gray-Stuart, E., Martinez-Hermosilla, G. A., Dahm, K., & Bronlund, J. E. (2018). A Technique to Quantify Damage of the Flute Profile in the Mid-Plane of Corrugated Fibreboard. In The 21st IAPRI World Conference on Packaging, 19-22 June 2018, Zhuhai, China.

The work from this chapter was used in collaboration with another study and presented in the following conference:

Kueh, C., Jamsari, M. A., Dahm, K., Ilanko, S., & Bronlund, J. E. (2019). Natural frequency modelling to identify material properties of crush damaged corrugated fibreboard. The 13th International Conference Computational Structures Technology, 4-6 September 2018, Sitges, Barcelona, Spain

3.1. Introduction

Chapter 2.3, presented various ways damage may happen at any stage through the lifecycle of CFB and how it is usually related with the changes to the flute structure. Damage such as an unintentional creasing line has been shown to reduce stiffness which subsequently allows failure to propagate through this local area (Beex and Peerlings, 2009). Popil (2007) reported that crushing of the flute results in a reduction in the flat crush hardness and the transverse shear stiffness of CFB. The loss in these properties may eventually result in the loss of the corrugated box stacking strength (Popil et al., 2007). Since the flute is also known to be the most important part of CFB in providing the stiffness and strength (Twede et al., 2014), it is important to have tools to characterise the flute profile of CFB to allow study on how it affects the performance locally as a CFB or globally as a corrugated box.

Chapter 2.4, discussed several research studies that demonstrated analysis of the flute shape at the edges of the panel. Biancolini (2005) obtained images of the flute profile through a camera and traced the shape manually before using it in finite element analysis to compare the effects of different shapes of the flute profile. It was reported that shape of flute profile was affected after it leaves the corrugator, after conversion and after case erection. Their finite element model showed that a change in bending stiffness of the board occurred with different flute shapes. This study, however, was only done at the edge of the board and it is likely that damage on the mid-plane flute profile is different. Some viable methods to achieve this were discussed in Chapter 2.4 concluding that laser cutting thin strips on the mid-plane region had the best potential due to its ability to avoid indentation when cutting the board.

For these reasons, this chapter presents investigation on developing a technique to geometrically describe the flute profile by laser cutting thin strips of CFB to analyse the shape at the mid-plane of the board. These thin strips were then photographed and further analysed using image analysis tools in Matlab R2018a (MathWorks Inc.).

First, a validation process was conducted to ensure that laser cutting can be used to capture the true flute profile of the board to be examined. Then, the development of the analysis will be explained in detail before introducing a variable called the Similarity Factor (SF) that can quantify the difference between a test sample and a reference flute profile. A validation process is then presented where a series of known computerised flute shapes were generated and analysed to demonstrate the accuracy of using this technique. After the validation process, actual flute profiles were measured and analysed to show the application of the technique.

3.2. Sample Preparation by laser cutting

It is essential that in preparing laser cut samples, the flute geometry structure is not changed. Potentially in making thin samples, the paper components could relax and the flute geometry could change. To demonstrate the capability of laser cutting to capture the true profile of CFB without adding additional damage or changes to the profile, a comparison of board before and after the laser cutting process was conducted. These differences were measured using a fringe projector (PRIMOS Lite) which is a non-destructive equipment to measure the surface profile of a sample. This equipment can capture an image at a size of 20 mm x 13 mm.

To aid comparison, CFB samples were creased to generate damage to the flute profile. This creasing process followed what has been reported by Gooren (2006) and was performed at peak or trough positions of the flute with a target crease indentation of 3 mm. The creases were made using a texture analyser TA.XT Plus (Texture Technologies Corp.) with a 3-mm thick aluminium blunt blade as the creasing tool. The samples were creased at a speed of 12.5 mm/min.

Ten samples of a virgin Kraft C-flute CFB were prepared for each creasing position; ten samples on the peak and ten samples on the trough positions. The dimensions of the samples were 65 mm x 200 mm. The samples were conditioned in accordance with TAPPI T402 prior to the creasing process.

The permanent deformation of the creased region of each sample was then measured by fringe projection, before being through-cut using a 120-Watt Fusion M2 (Epilog Laser) into thin strips of 80 mm x 1 mm perpendicular to the creased line. The permanent deformation of the creased region on the thin strips was then measured. Table 3-1 shows a sample of differences between creased board before and after the laser cutting process together with its surface topography measured using the fringe projector while Figure 3-1 shows example of creased profile samples before and after the laser cutting.

Table 3-1: Top-view image and surface topography of creased CFB on the trough position (flute run horizontally) before and after the laser cutting process. (The crease was measured horizontally from the surface topography figures in the cut region where the colour denotes the height measured)

Process	Before Cutting	After Cutting
Image	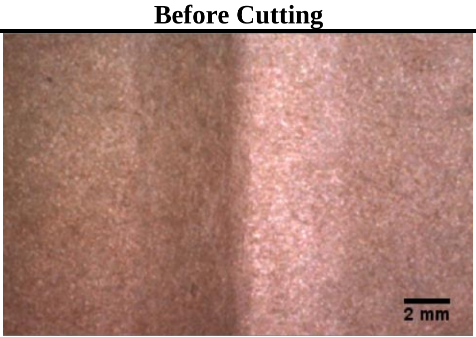	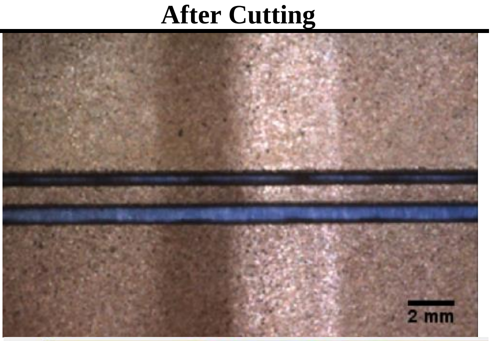
Surface Topography	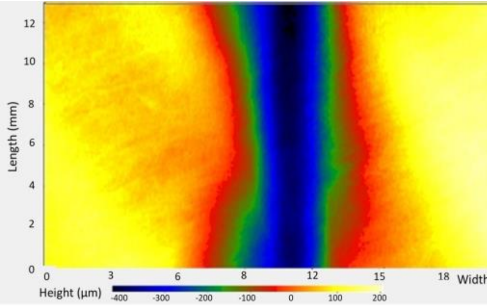	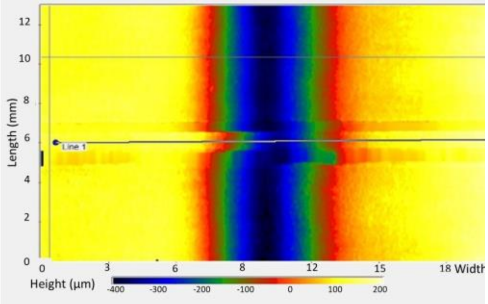

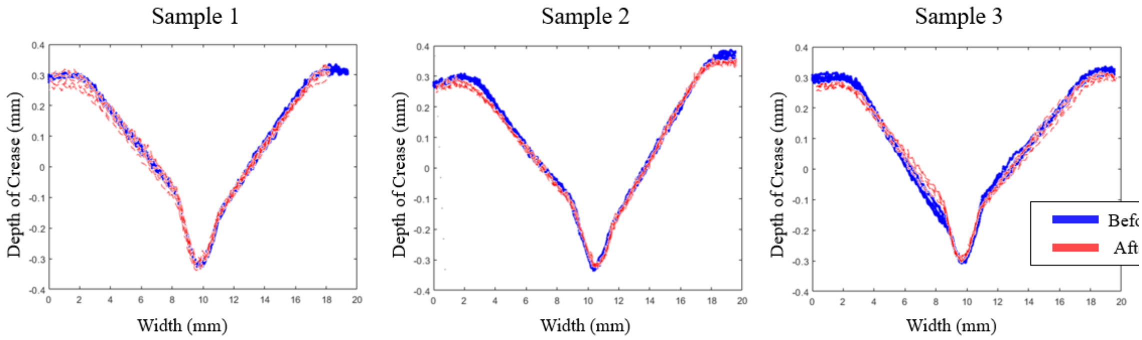

Figure 3-1: Example of samples of creased profile CFB on the trough position as extracted from the surface topography figures. The depth of crease was calculated from the average of the maximum points on the left half and right half, and the minimum point in the figures.

The permanent deformation of the crease before and after the laser cutting process were compared and analysed using a paired sample t-test to determine if the laser cutting technique caused any additional damage in the thickness direction of the board or allow recovery of the original structure on the creased region of the samples.

For the creasing on the peak position, there was no statistically significant difference between the permanent deformation of the creased region before cutting (640.23 ± 14 μm) and after the cutting process (639 ± 25 μm); t (9) = 0.270, p = 0.79. Similarly, for the creasing on the trough position, no statistical difference was found between the permanent depth of the crease before cutting (448 ± 18 μm) and after the cutting process (451 ± 32 μm); t (9) = -0.454, p = 0.66. The results justify the use of a laser cutter to cut small samples on the mid-plane of CFB to allow subsequent analysis of the flute shape.

3.3. Development of the Skeleton Analysis

The skeleton analysis was carried out using the image processing toolbox in Matlab R2018a (MathWorks Inc.). First, the scanned image was converted into a binary image where the flute is white with a black background. The thin strip was then skeletonised where it was reduced into lines without changing its main structure as shown in Figure 3-2. This method follows the Zhang-Suen thinning algorithm where patterns are thinned down to a unitary thickness of 1 pixel (Zhang and Suen, 1984).

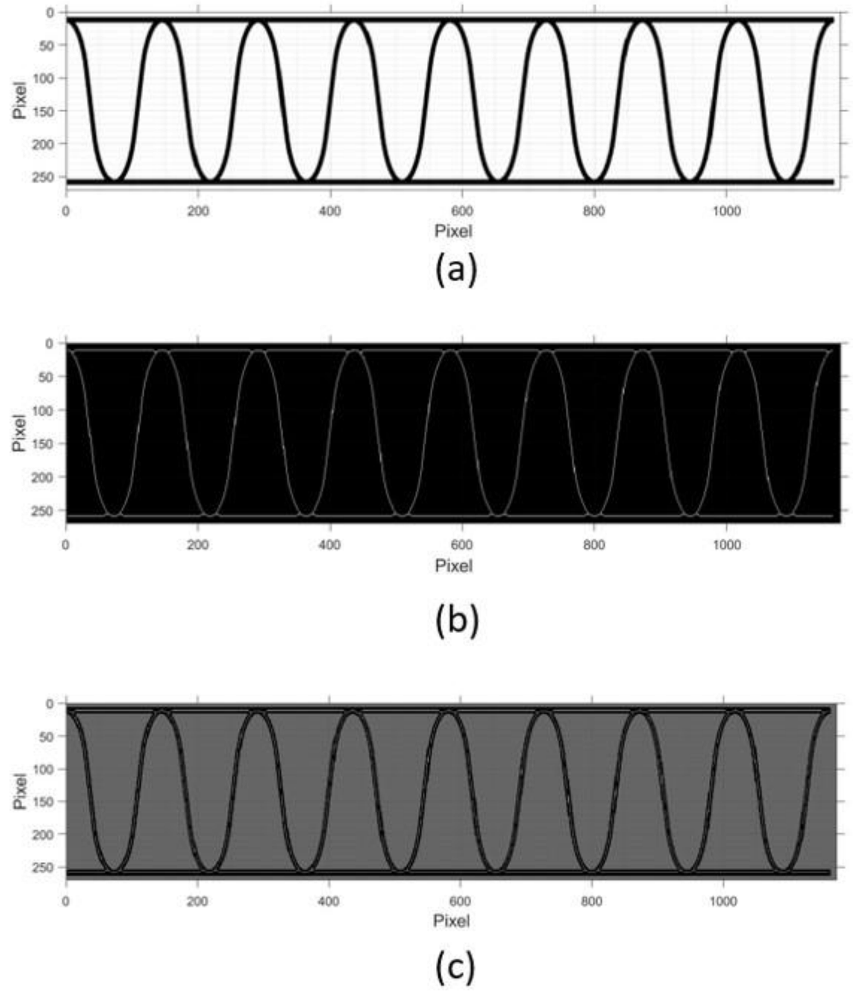

Figure 3-2: (a) Original image of the flute transformed into a black and white image (b) Skeletonization of the image of the thin strip using Matlab R2018a (c) Final product of the skeletonization process where patterns are thinned down to 1 pixel without damaging the original structure (the skeletonised flute in (b) is stacked on the original flute in (a)).

By analysing the number of white pixels in each column throughout the image as a separate group as illustrated in Figure 3-2(b), they can be divided into two different classes (peak or trough, and mid-flute sections) as shown in Table 3-2. With these different classes, the region of the flute can then be determined.

Table 3-2: Segregation of the columns in the image into different groups based on the number of white pixels.

Class	Number of white pixels	Region
1	2 white pixels	Peak or Trough
2	>3 white pixels	Slant height of the flute (mid-flute sections)

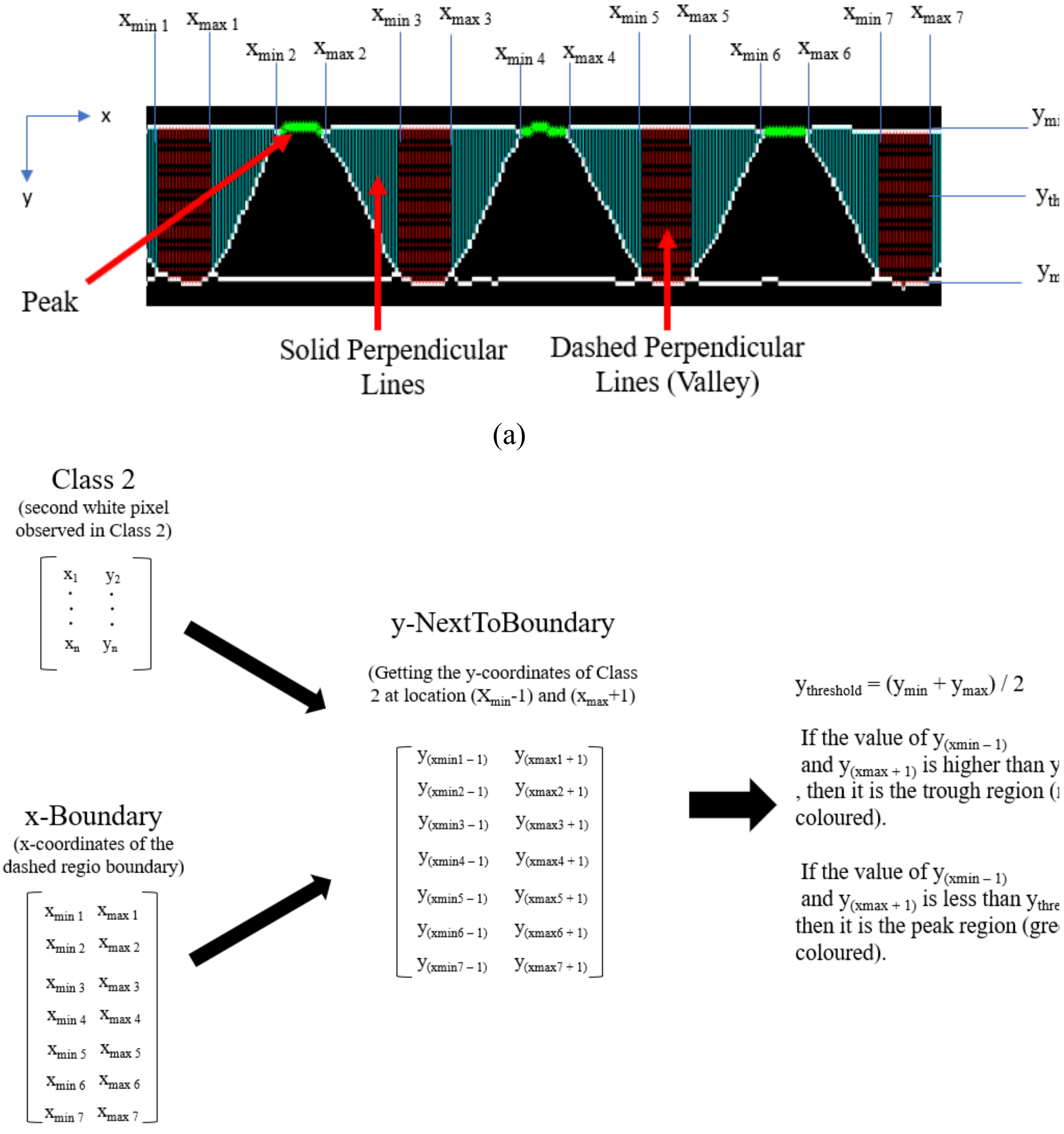

(a)

(b)

Figure 3-3: Determining the shape of the flute after the skeletonization process where (a) shows the visualisation of the process and (b) shows the process of determining the peak and trough positions. (The variables in the figure are shaded in the text)

As shown in Figure 3-3 (a), for the column that was classified as Class 2 (the slanted region), cayenne solid lines were plotted from the first to the second white pixel. The x and y coordinates of the second white pixel which represents the slanted lines were stored in an array called Class 2. (Note: Grey shaded words denote the variables in Figure 3-3)

For Class 1 columns, green dots and red dashed lines were plotted in Figure 3-3. To determine whether the regions in Class 1 lie on peak or trough regions. First, the minimum and maximum x-coordinates of each Class 1 region were recorded into an array called the x-Boundary as shown in Figure 3-3 (b) with reference to the image in (a). These coordinates allowed determination of the peaks and troughs by observing the y-coordinate of Class 2 at locations of the previous column of x_{min} and next column of x_{max}. These y-coordinates was then stored in an array called y-NextToBoundary.

$y_{threshold}$ was initiated by averaging the values of the highest and lowest y-coordinates of the flute (y_{min} and y_{max}). The region of peak or trough was then determined by observing whether the y-coordinates in y-NextToBoundary are higher or lower than $y_{threshold}$; where it is a trough if it is higher and a peak if it is lower (recall the y-axis is defined from top to bottom in the image rows).

When all the points on the flute been determined and recorded, these points were converted from pixels to millimetres by multiplying with the scaling value. The scaling value was determined by dividing the actual length of the strip (in millimetres) by the length of the strip in the image (in pixels).

One of the limitations of this analysis was that the peak should not overlap with the trough on the flute profile as the overlapping would not meet the constraints presented in Table 3-2. Based on the constraints, the peak and trough positions were determined only when the row consists of 2 white pixels. However, when the peaks and troughs started to overlap, the number of white pixels in the peak and valley rows would increase. This results in the analysis being unable to differentiate the actual positions of the peaks and troughs.

3.4. The Similarity Factor (SF)

The aim of the Similarity Factor (SF) is to quantify the morphological difference between a test sample flute profile and a reference flute profile (usually from an undamaged board). The SF was calculated using the same approach as for the coefficient of determination, R^2 in statistics, where a model is compared to experimental data. By subtracting the corresponding coordinate points of the flutes between two images, a set of residuals can be created and used to calculate the SF.

To ensure both the reference and test flutes were aligned, the mean from both flutes were set as zero on the y-axis and the test flute was shifted horizontally until its peaks and troughs matched the reference flute. The reference flute could be an idealized flute shape (used in Section 3.5), image analysis of a high quality CFB example (used in Section 3.6) or a before sample in experiments investigating the effect of a manufacturing step on flute geometry.

The first step to calculate the SF was to find the mean of the reference flute which is given by: -

$$\bar{y} = \frac{1}{n}\sum_{i} y_i \tag{3.1}$$

where n is the number of elements and y is the coordinate of the reference flute as shown in Figure 3-4.

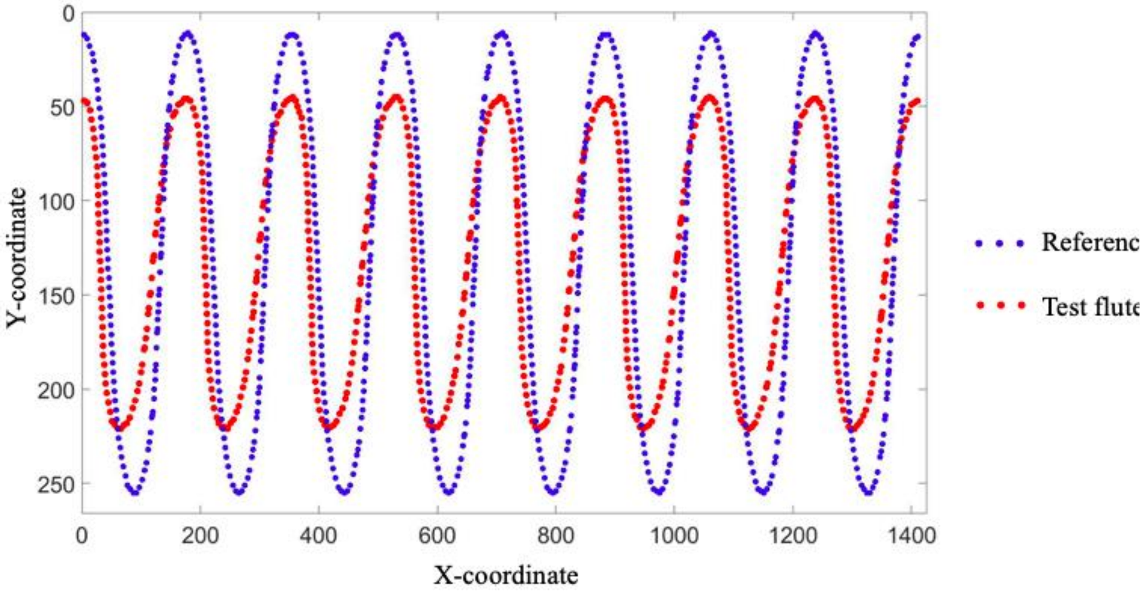

Figure 3-4: Example of computer-generated reference flute coordinate and test flute of shear and caliper reduction as will be presented in the next section. Units are points as both flutes are generated electronically to demonstrate their differences.

Then, using the result from equation (3.1), the total sum of squares was calculated by: -

$$SS_{tot} = \sum_i (y_i - \bar{y})^2 \tag{3.2}$$

The sum of squares of the residual between the test flute and the reference flute was then calculated by: -

$$SS_{res} = \sum_i (y_i - f_i)^2 \tag{3.3}$$

where *f* is the coordinate of the test flute.

Finally, using the results from equations (3.2) and (3.3), the SF was calculated by: -

$$Similarity\ Factor\ (SF) = 1 - \frac{SS_{res}}{SS_{tot}} \tag{3.4}$$

Hence, the computed SF value of each flute can quantify the differences in flute morphology between two given flute profiles (a test and a reference flute profile). It was hypothesised that mechanical damage to the board can modify flute morphology which can be quantified using SF. In addition, the image analysis process also allows the calculation of further advanced features such as the calliper, the radius of curvature on peaks and troughs, and the flank angle of the flute between peaks and troughs.

3.4.1. *Advanced Feature*

Other than the SF, the analysis can also determine some in-depth features that roughly identifies and covers a flute wavelength when dividing them into four regions as illustrated in . The features include measuring the flute height of the flute, determining the curvature of the peak and trough region and calculating the flank angle of the flute.

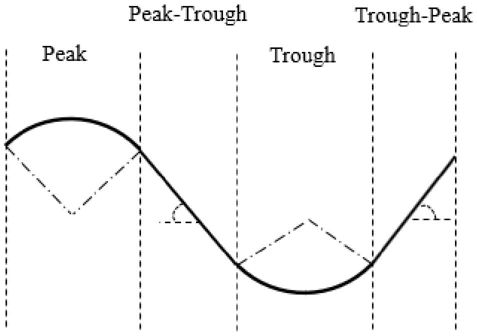

Figure 3-5: A flute wavelength when divided into four regions to carry out detailed analysis in comparison to the reference flute.

Flute Height

From section 0, the coordinates of the peak and trough regions have been determined. To measure the flute height, the coordinates in both regions are subtracted from each other and averaged.

Curvature of Peak and Trough

This feature involves fitting a quadratic polynomial curve on each region of peak and trough with the equation given by:

$$y = ax^2 + bx + c \tag{3.5}$$

where x and y are the flute coordinates fitted into the equation to obtain the fitting coefficients a, b and c. The fitted curve is then differentiated twice to obtain the curvature, k, of the region. The radius of the curve is then computed by:

$$r = \frac{1}{k} \tag{3.6}$$

This step is chosen over the finite difference of the coordinates since it measures the curvatures between each pixel point rather than the region of peak and trough. Hence the curvatures vary between each point when applying a finite difference on them. Figure 3-6 shows the illustration on using the finite difference method to obtain the curvature and applying a fitting curve on the peak and trough region of the flute.

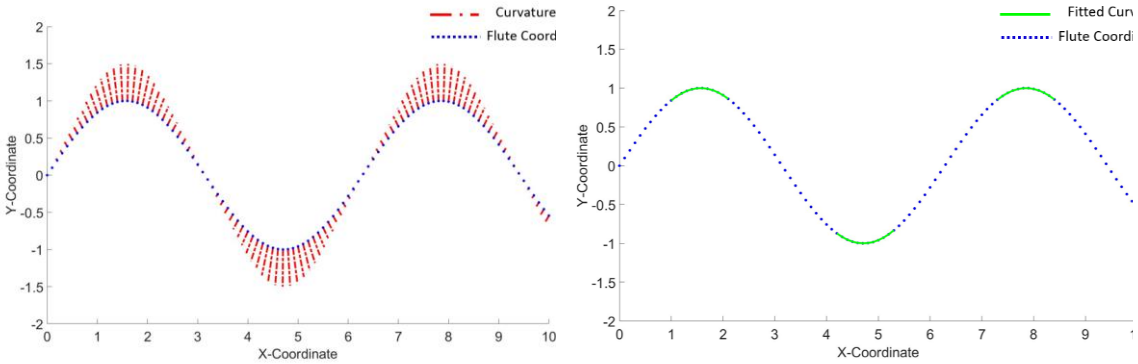

(a) (b)

Figure 3-6: Illustration on measuring the curvature of the peak and trough region where figure (a) shows the curvatures computed using finite difference of the flute coordinates and figure (b) shows curve fitting on the region of peak and trough and calculating the curvatures from the curves.

Flank Angle

First, the midpoint of the length of the flank, $(x, y)_{mid,flank}$, in each region between the peak and trough are determined. Then another two points $(x,y)_{1,flank}$ and $(x, y)_{2,flank}$ are determined by finding the coordinates of the flute that are 25% of the flank height, fh, away from the midpoint in both direction. These points are illustrated in Figure 3-7.

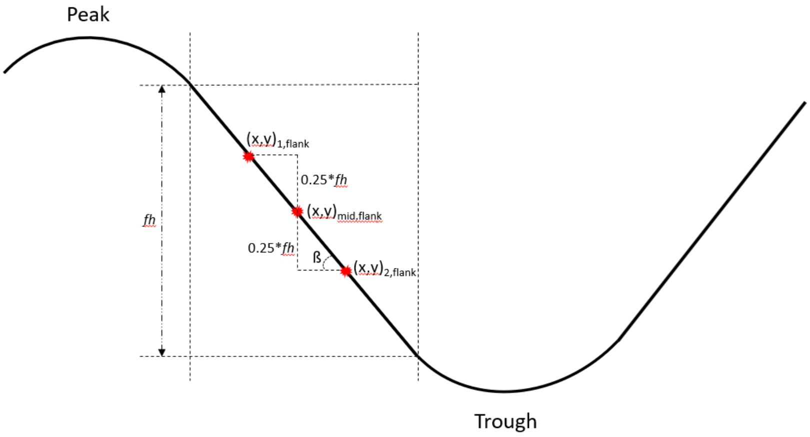

Figure 3-7: Illustration on determining of $(x, y)_{1,flank}$ and $(x, y)_{2,flank}$ coordinates on the flute flank on the peak to trough region.

Using both coordinates, the flank angle, ß, can be computed by:

$$ß = cos^{-1}\left(\frac{\sqrt{(x_{2,flank} - x_{1,flank})^2 + (y_{2,flank} - y_{1,flank})^2}}{(x_{2,flank} - x_{1,flank})}\right) \tag{3.7}$$

3.5. Accuracy of the Skeleton Analysis

To ensure the accuracy of this analysis, it was validated against known parameters of flute geometry. To do this, a variety of flute images were generated using a set of equations in Matlab. Then, the accuracy of the skeleton analysis could be judged by how well it traces the flute compared to the actual points of the generated flute. The SF was then used to compare the initial and the skeleton-analysed computer-generated flute profiles. Ideally, the SF should be close to 1 for all cases.

In Chapter 2.5.1, an arc-and-tangent curve that was developed by Urbanik (2001) was presented and discussed. This approach requires the input of the flute calliper (h_f), pitch (P) and take-up ratio (α) as shown in Figure 2-7 (Note take-up factor is not shown in the figure). The output will generate the flute tip radius (R), length of the flank (L) and the angle of the flank (β). This approach was used to produce the computer-generated flute profiles.

In addition, controlled levels of distortion were also added to the generated flute profiles. These distortions were represented by decreasing the calliper of the flute by a certain percentage, making the flute bend at an angle and adding noise at the edge of the flute to represent an actual board as shown in Figure 3-8. This study assumed a constant damaged on the board such as crushing and shearing where all flutes in each sample experienced the same amount of crushing and flute bending.

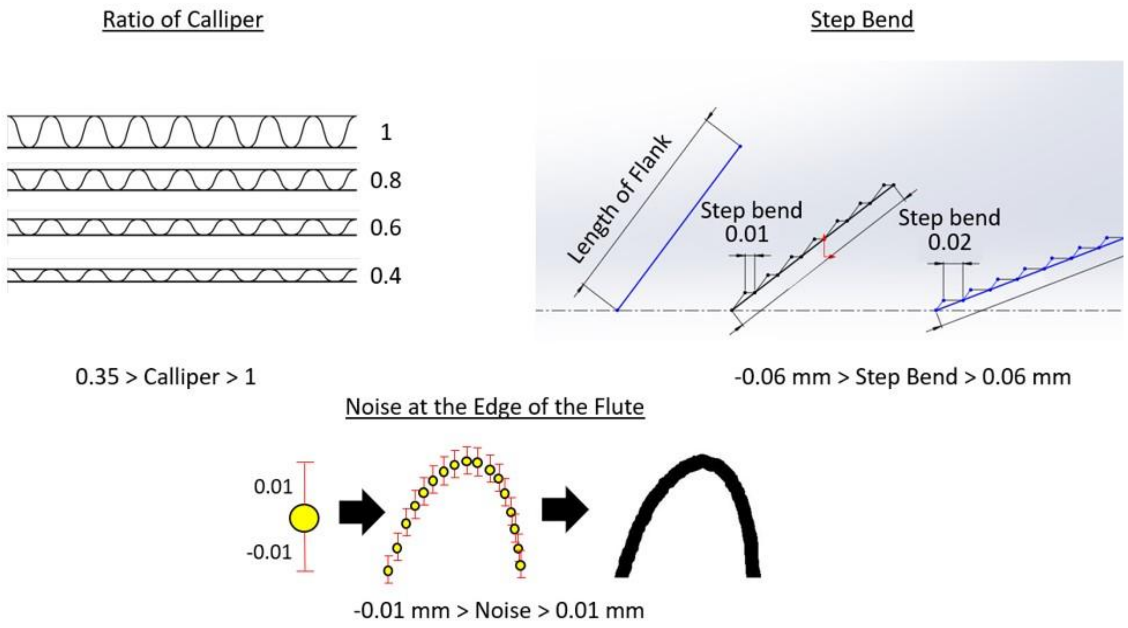

Figure 3-8: The distortions that were added in Urbanik's model which are ratio of decrease in calliper, adjusting the slant of the flute (step bend) and inserting noise at each point on the flute.

These distortions were combined to produce variations of the flute geometry and referred to in this section as the initial flute as shown in Figure 3-9. The coordinates for each of the initial flutes were recorded in matrices allow later comparisons.

To replicate an actual thin strip, a top and bottom liner were added to the initial flute as shown in the second column in Figure 3-9. The addition of liners was crucial as with an actual board, liners will always be present.

The images of the thin strip replicates were then fed into the skeleton analysis, producing skeleton-analysed flutes as shown in the third column of Figure 3-9. Finally, the skeleton-analysed flutes were compared with the initial flutes to measure the accuracy of the skeleton analysis.

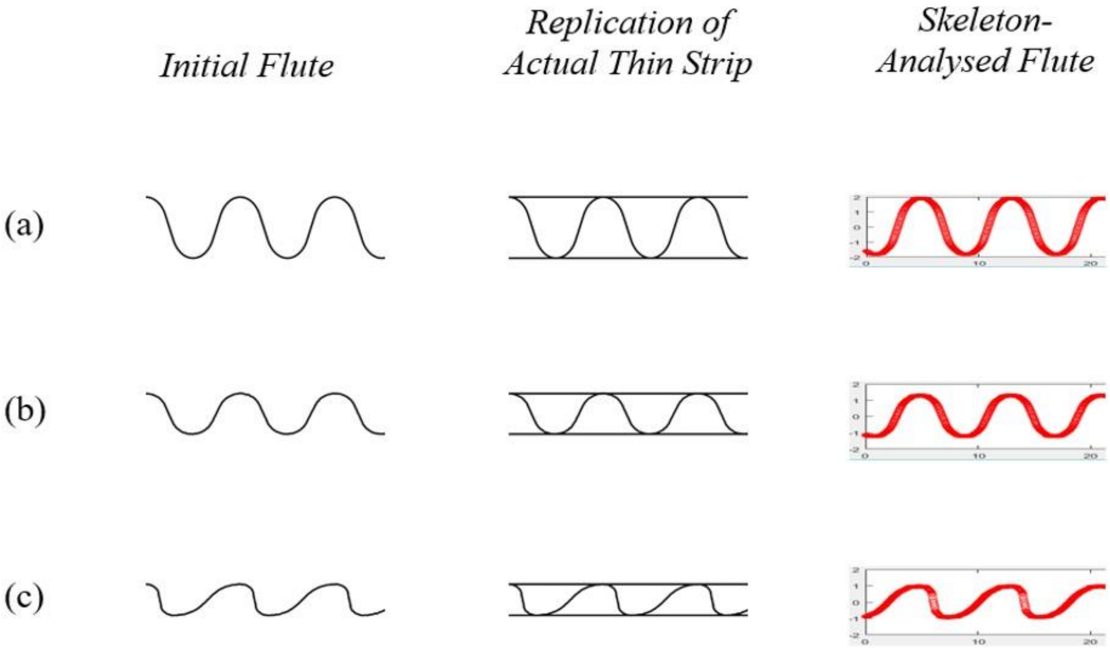

Figure 3-9: The initial flute (640x110 pixel), addition of liners on the initial flute to replicate an actual thin strip produced from Urbanik's model and the skeleton-analysed flute where (a) is the undamaged flute, (b) decreasing the calliper of the undamaged flute and (c) decreasing the calliper and adjusting the flute to bend at an angle.

Taking this approach, a total of 100 random images with different variations were generated and analysed.

As shown in Figure 3-10 and Figure 3-11, the SF's were all higher than 0.9987 which signifies that the differences between the initial flute and the skeleton-analysed flute is small. The error that exists was largely associated with the addition of the top and bottom liners in the skeleton-analysed flute as seen in Figure 3-10. This addition tends to flatten the curvatures of the peaks and troughs at the flute tip as shown in Figure 3-12. It is also worth noting that these images were all idealized flute profiles with the same underlying shape structure, but different input parameters based on Urbanik's geometric model, hence, the SF should be close to 1.

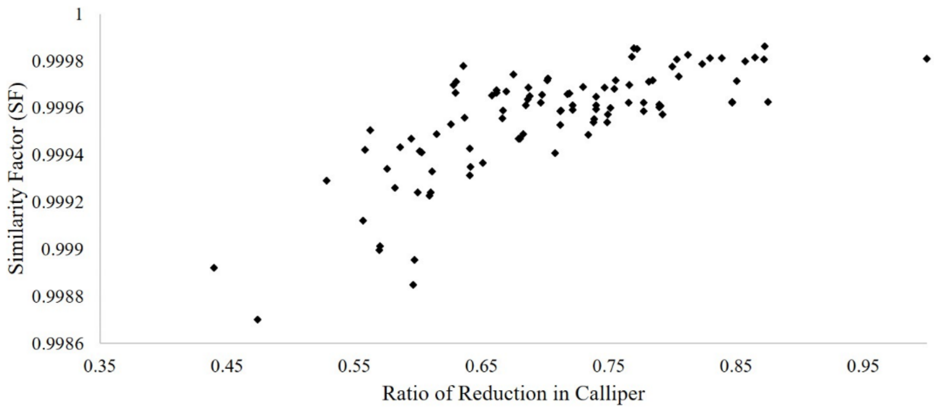

Figure 3-10: Scatter distribution of the SF between the initial flute and skeleton-analysed flute against the fraction of the original calliper.

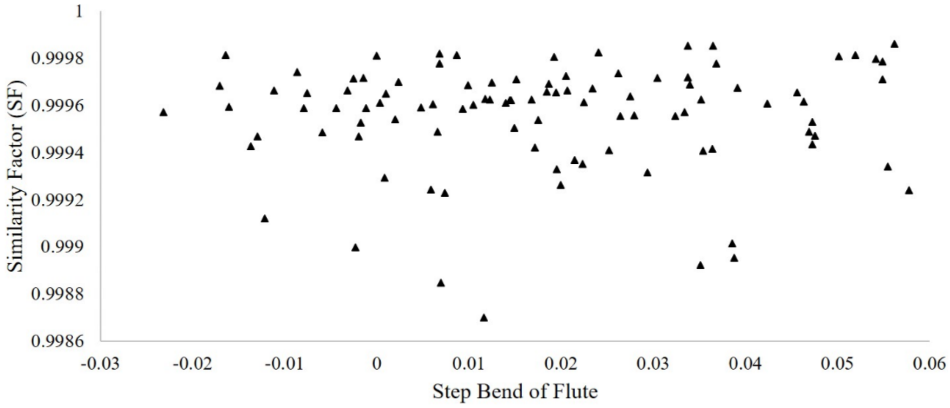

Figure 3-11: Scatter distribution of the SF between the initial flute and skeleton-analysed flute against the step bend of the flute.

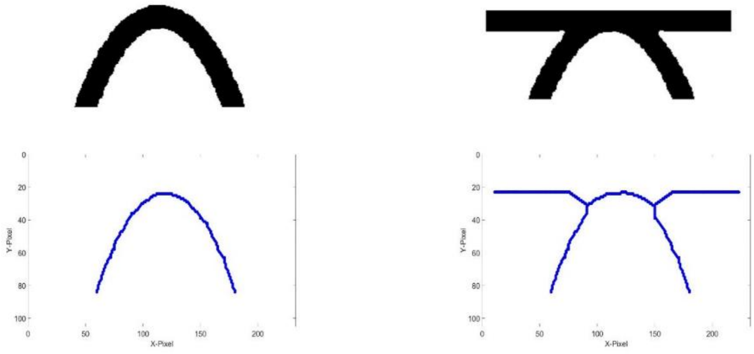

(a) Initial flute

(b) Skeleton-analysed flute

Figure 3-12: Illustration on the peak of a flute profile where (a) shows the initial flute coordinates and (b) shows the flute with liners and its flute coordinates after being skeletonised. It is observed that the curvature of the skeleton-analysed flute is flatter than the initial flute.

To justify that the curvatures on the peaks and troughs were the cause of the differences in the SF between the initial and the skeleton-analysed flutes, advanced features were used to measure the radius of curvature on the peaks and troughs, and the flank angles between peaks and troughs. The results of these features were then analysed using a paired sample t-test analysis to determine the statistical significance of the differences between both images as illustrated in Appendix A. The paired sample t-test showed that there was no significant differences on both flank angles between the initial flute and the skeleton-analysed flute, however, there were significant differences in both the radius of curvature on peaks and troughs due to the flattening of the curve with the addition of liners as shown in Figure 3-12.

To find out the lowest SF possible between the initial flute and the skeleton-analysed flute, three different flutes were generated with the extreme-case distortion based on parameters of flute geometry shown in Figure 3-8. These flutes were set to have the lowest possible caliper set at zero, maximum and minimum step bend. The SF results are presented in Table 3-3. The lowest SF was found to be 0.9984 and only the radius of curvature on peaks and troughs showed significant differences.

*Table 3-3: Comparison of the initial flute and the skeleton-analysed flute with different extreme-case parameters as set in Figure 5. In the last four columns, * means statistically significant between initial and skeleton-analysed flute while - means not statistically significant. The results were based on a paired sample t-test.*

Image	Step Bend (mm)	Ratio of Calliper (%)	SF (Initial vs Skeleton-Analysed)	Radius of Curvature Peak	Lean Angle Peak Trough	Radius of Curvature Trough	Lean Angle Trough Peak
Undamaged	0.000	1.00	0.9999	*	-	*	-
Extreme Case 1	0.000	0.35	0.9985	*	-	*	-
Extreme Case 2	0.060	0.35	0.9984	*	-	*	-
Extreme Case 3	-0.060	0.35	0.9984	*	-	*	-

For all the four cases, the plot of the initial flute, skeleton-analysed flute and the residual between both geometries are presented in Figure 3-13. It can be observed that the non-zero residual points were scattered only on the regions of peaks and troughs. Hence, this supports the earlier statement that the radius of curvature on peaks and troughs were affected with the addition of liners.

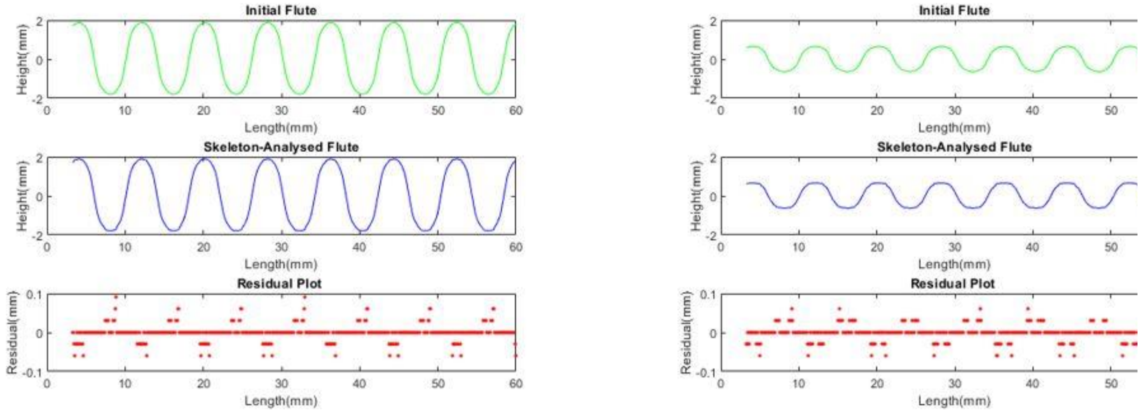

(a) Undamaged

(b) Extreme-case 1

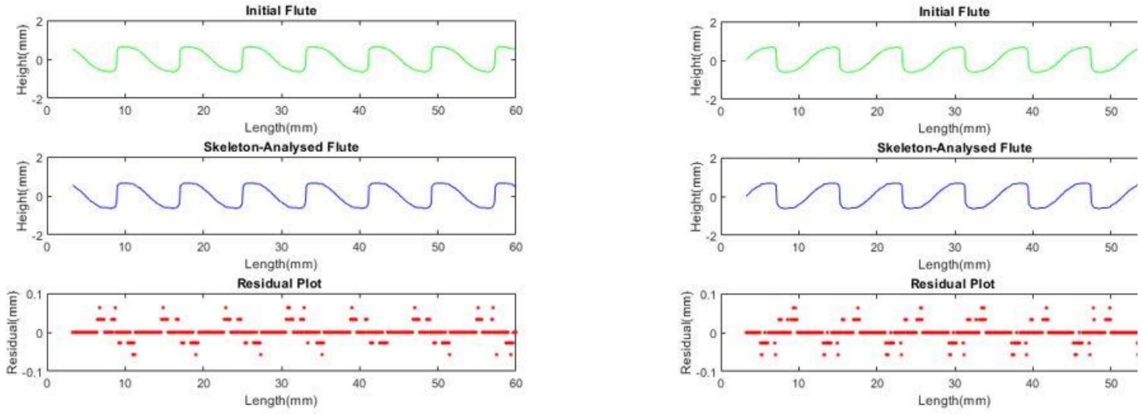

(c) Extreme-case 2

(d) Extreme-case 3

Figure 3-13: The plot of the initial flute, skeleton-analysed flute and the residuals between both flutes for different geometrical structure of a flute profile.

The similarities between both the initial and skeleton-analysed flute geometries at all other points aside from the curvatures on the peaks and troughs (which were unavoidable), shows the ability of the skeleton analysis to trace the flute with good accuracy.

The residuals from the curvature regions were only present when comparing flute with liners relative to flute without liners as demonstrated in this section. In analysing actual board, this noise is eliminated since all flutes will have liners on them.

3.6. Sample Acquisition and Quantifying Damage using Skeleton Analysis

This section demonstrates the use of the skeleton analysis technique and SF to quantify morphological damage on actual board that was subjected to different levels of mechanical crushing.

Virgin Kraft C-flute CFB with a thickness of 4.24 mm was used and comprised of a 0.253 mm outer liner, a 0.204 mm fluted liner and a 0.32 mm inner liner. Ten samples of 150.8 mm x 280 mm dimensions were crushed to 0.5 mm, 1.0 mm and 1.5 mm to capture the flute profile at each stage of compression. The compression process was done at a speed of 12.5 mm/min using an Instron 1195 machine and a flat platen. The extent of crushing were decided based on typical crushing behaviour of CFB as shown in Figure 3-14 where level (b) 0.5 mm represents the end of the linear slope of the graph, level (c) 1.0 mm represents about the maximum force required to irreversibly compress the board and level (d) 1.5 mm represents the flute profile after failure.

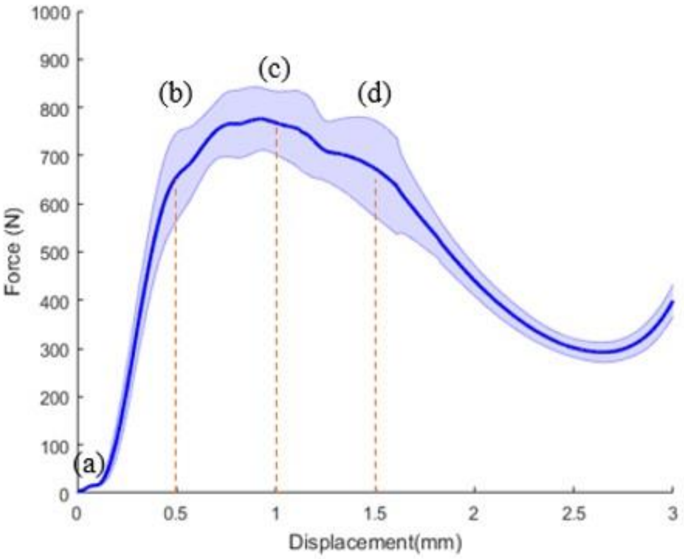

Figure 3-14: Graph of force against displacement when compressing 150.8 mm x 280 mm C-flute CFB. The graph contains the average and standard deviation plot from 10 replicates of CFB where the average line is denoted by the solid line and the standard deviation is denoted by the upper and lower region.

The crushed samples then went through the laser cutting process to obtain the thin strips of the flute profile with a dimension of 80 mm x 1 mm using the same laser cutter parameters as described previously. The thin strips were then carefully placed on a light table (back lighting) with a blank paper filter added between the thin strips and the light table to ensure an evenly distributed light. A Nikon D3100 camera with 18 – 55 mm lens was used to obtain the images. A flatbed scanner was initially considered as it works best in avoiding distortion issues but it causes shadows on the flutes as a result of the back lighting that scans from top to bottom.

To minimise distortion, the camera was placed perpendicular to the thin strips with a distance of 550 mm between the lens and the samples, and ensure it was level to the ground as illustrated in Figure 3-15. To ensure a constant alignment of the thin strips, a jig was used.

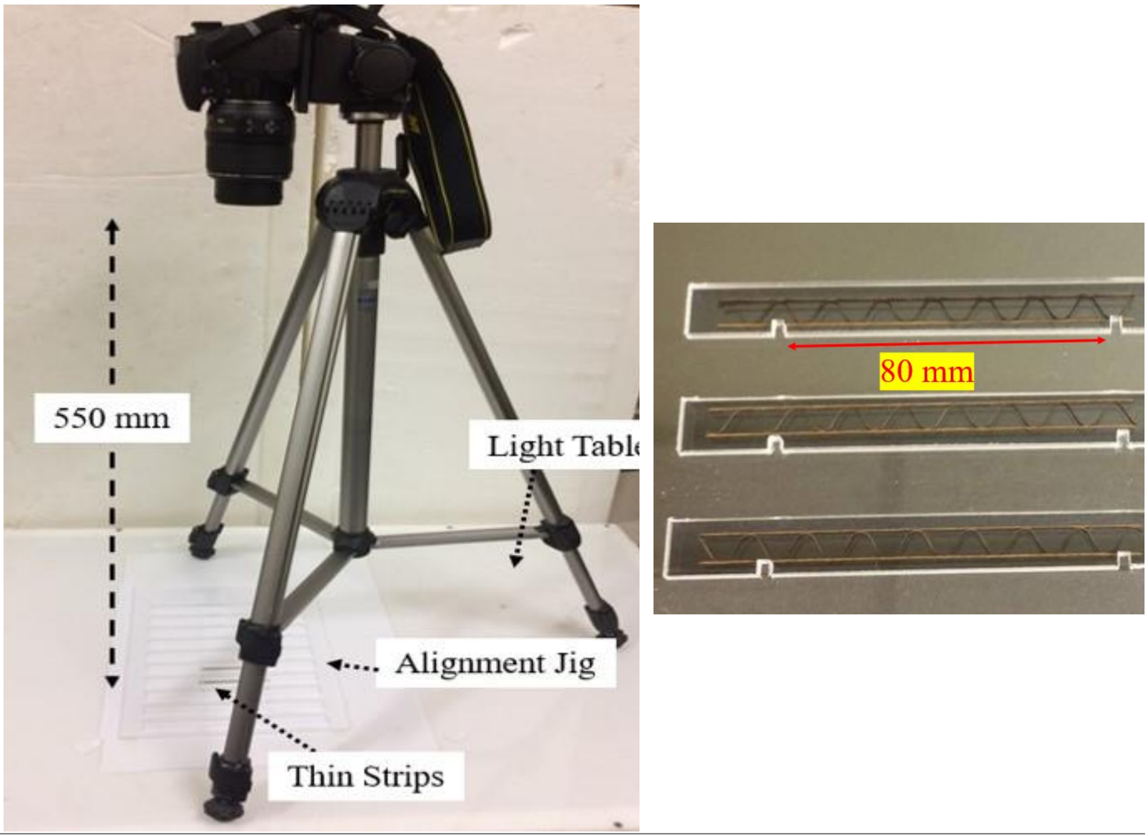

Figure 3-15: Setup of the camera used to capture the image of thin strips to capture the flute profile of CFB on the left hand side and a closer look at the jig on the right hand side..

The captured images that contained multiple thin strips were then cropped and converted into individual binary images of thin strip with a dimension of 440 x 80 pixels. These individual binary images were then fed into the skeleton analysis to obtain their SF. The average undamaged flute from ten samples was used as the reference geometry.

Table 3-4 shows that the SF decreased as the level of crushing progressed. The recorded SF of 0.9974 with a standard deviation of 0.0007 for the 0 mm uncrushed level showed the natural variation that can be expected between undamaged flutes of CFB. As the board was crushed to level (b), the SF significantly decreased with an average of 0.9961. The SF further decreased as the flutes were crushed to levels (c) and (d).

Table 3-4: Illustration of the flute profiles obtained from the thin strips at different levels of crushing damage, along with calculated average similarity factor and the standard deviation from 10 samples.

Crush Level	Flute Profile	Similarity Factor (SF)
(a) 0 mm		0.9974 ± 0.0007
(b) 0.5 mm		0.9961 ± 0.0009
(c) 1.0 mm		0.9878 ± 0.0061
(d) 1.5 mm		0.9760 ± 0.0051

To identify the region where the differences were observed between each level of flute, the advanced features were applied on each flute to measure the calliper, the curvatures on the peaks and troughs, and the flank angles between peaks and troughs. The average values together with the standard deviation of each feature are tabulated in Table 3-5.

Table 3-5: The curvatures of peaks and troughs, and flank angles between peaks and troughs at four different levels of flute crushing. The number of stars (*) denotes the significance level between each crushed level based on an ANOVA and Tukey posthoc analysis, hence, same number of stars means same level of significancy.

Crushed Level	Calliper (mm)	Radius of Peak Curvature(mm)	Flank Angle Peak Trough (°)	Radius of Trough Curvature(mm)	Flank Angle Trough Peak (°)
0.0 mm	3.82 ± 0.03*	1.81 ± 0.27*	59.78 ± 1.90*	-1.73 ± 0.16*	62.69 ± 1.92*
0.5 mm	3.76 ± 0.04**	1.90 ± 0.30*	61.15 ± 1.90*	-1.74 ± 0.19*	62.03 ± 2.24*
1.0 mm	3.63 ± 0.04***	3.12 ± 0.76**	67.38 ± 2.65**	-2.01 ± 0.27**	63.73 ± 5.11*
1.5 mm	3.45 ± 0.05****	3.62 ± 0.76***	66.32 ± 2.13**	-2.63 ± 0.30***	74.63 ± 2.51**

From Table 3-5, it can be observed that there was a significant decrease in the calliper when the board was crushed to level (b). However, there was no significant difference in other features between 0.0 mm and level (b) which might be due to the crushing damage being at the end of the elastic part of the load curve based on Figure 3-14.

It was seen that the mean values of the peak curvature radius, flank angle between peak to trough and the trough curvature radius were larger when the board was crushed to level (b). The combination of these features may be the reason why SF was found to be significant between 0.0 mm and level (b) based on Table 3-4.

When the board was crushed to level (c) which was beyond the elastic region, the calliper, peak curvature radius, flank angle between peak to trough and trough curvature radius showed significant differences compared with the previous two crushing levels. Finally, when the board was severely damaged to level (d), all the features showed significant change compared to level (c) except for the flank angle between peak to trough. The illustration of the measurements in Table 3-5 are shown in Appendix A.

3.7. Conclusion

This chapter demonstrated that a laser cutter can be used to cut CFB without significantly affecting its flute profile. This allowed direct observation of the flute profile of the board at mid-plane. The imaging of thin strips and subsequent skeleton analysis developed in this chapter was validated against known geometries and showed excellent agreement with small differences due to difficulties in image differentiation between the flute tips and liners.

This chapter also demonstrated the use of the skeleton analysis to analyse the flute profile using the SF and other advanced features. As the board experienced more damage, the SF reduced. The reduction of SF can be explained by observing the curvatures of the peaks and troughs, and the flank angles between peaks and troughs.

This technique can be used as an objective measure of flute damage which can potentially be linked to changes in mechanical properties of CFB. In Chapter 5, work focusing on relating these quantified flute damage measurements to the mechanical properties of the damaged board such as the transverse shear stiffness, bending stiffness and the edge crush test are presented. In addition, the geometry traced using the skeleton analysis can be transferred into a computer-aided design software to be able to represent the exact flute shape for modelling purposes. This approach is presented later in Chapter 6 after appropriate models of CFB are developed in the next chapter.

Reference

Beex, L., & Peerlings, R. (2009). An experimental and computational study of laminated paperboard creasing and folding. International Journal of Solids and Structures, 46(24), 4192-4207.

Biancolini, M. E. (2005). Online quality control of corrugated board panel by image processing. International Journal of Computer Applications in Technology, 23(2-4), 157-165.

Gooren, L. (2006). Creasing behaviour of corrugated board (Master's Thesis). Eindhoven University of Technology, The Netherlands.

Popil, R. E. (2007). Shear measurement of board crushing effects. Paperboard Packaging, 92(7), 37.

Popil, R. E., Coffin, D. W., & Habeger, C. C. (2007). Transverse shear measurement for corrugated board and its significance. Paper presented at the 61st Appita Annual Conference and Exhibition, Gold Coast, Australia 6-9 May 2007: Proceedings.

Twede, D., Selke, S. E., Kamdem, D.-P., & Shires, D. (2014). Cartons, crates and corrugated board: handbook of paper and wood packaging technology. DEStech Publications, Inc.

Urbanik, T. (2001). Effect of corrugated flute shape on fibreboard edgewise crush strength and bending stiffness. Journal of Pulp and Paper Science, 27(10), 330-335.

Zhang, T., & Suen, C. Y. (1984). A fast parallel algorithm for thinning digital patterns. Communications of the ACM, 27(3), 236-239.

Chapter 4.

Predicting Corrugated Fibreboard Performance: Modelling and Validation

---

Preface

This chapter investigates ways of assessing the mechanical performance of CFB which has been presented in the literature review back in Chapter 2. Since conducting box compression testing (BCT) consumes a lot of time and materials, in this work an alternative approach was taken. Bending and crushing performance of CFB are both strongly related to the BCT and are independent of complications such as folds, manufacturing joins and box geometry. This chapter includes development of a finite element (FE) mechanical model for both tests which provides an in-depth understanding of CFB performance and how paper properties and flute geometry influence strength performance. These models are validated against experimental tests for CFB. A validated model provides the basis for exploration of how flute geometry and damage impacts CFB performance in latter chapters of the thesis.

The bending performance of CFB at different orientations part of this chapter was written and published as:

Jamsari MA, Kueh C, Gray‐Stuart EM, Dahm K, Bronlund JE (2019). Experimental and numerical performance of corrugated fibreboard at different orientations under four-point bending test. Packaging Technology and Science, 32(11), 555-565.

Part of this chapter that focused on the edge crush test (ECT) of CFB has been applied to data from another research project (Nevins, 2008) and presented in the following conference (attached in Appendix F):

"Modelling the Edge Crushing Performance of Corrugated Fibreboard under Different Moisture Content Levels" (ID: 4981) presented at International Conference on Computational & Experimental Engineering and Sciences (ICCES 2019) Tokyo, Japan March 25th -28th 2019

4.1 Introduction

As described in the literature review, (Chapter 2.2), the box compression test (BCT) is widely used to quantify the strength performance of the box, however this approach consumes time and materials and is a strong function of box geometry and design. To accommodate this problem, bending and edge compression tests (ECT) can be carried out as these are strongly related to the BCT according to McKee et al. (1963). The ECT is carried out in the CD direction of CFB while the bending stiffness is carried out in MD and CD directions. In addition to the bending stiffness on MD and CD, it was also of interest in this study to measure and model the bending behaviour of CFB when orientated at different angles between MD and CD directions. While bending behaviour of CFB at intermediate angles is not widely measured, it provides additional data to compare FE models against, and a more complete validation.

Chapter 2.5 summarised the approaches to carrying out FE simulation on CFB. Describing the anisotropic behaviour has been shown to be challenging and requires extensive experimental work. Orthotropic behaviour can be assumed for the paper structure as it is simpler and has been shown to be effective in modelling the strength of CFB. It was also found that the flute geometry of CFB can constructed through arc-and-tangent curves which takes into account the right take-up factor as opposed to simpler sinusoidal, elliptical and trapezoidal shapes (Urbanik, 2001).

The aim of this study was to develop a FE model of ECT and bending stiffness of CFB to gain an in-depth understanding. Such a model can form the basis for later investigation of how non ideal flute geometries (such as can be measured using the image analysis method presented in Chapter 3) impact on CFB performance. A good predictive model also provides rapid way of predicting CFB properties from paperboard material properties and CFB geometry.

Along with the experimental characterisation and FE model development, this study also evaluates analytical solutions for both tests. The study was started by developing the analytical solution and FE models of both tests. Then the experimental test of ECT and bending stiffness of CFB oriented at different angles between CD and MD were carried out to validate the models.

4.2 Materials and Methodology

4.2.1 Tensile Properties of Paper Components

The board used in this study was a single wall C-flute corrugated board which was supplied by Oji Fibre Solutions, New Zealand. The geometrical characteristics of the board are given in Table 4-1 and the details of each paper component are listed in Table 4-2.

Table 4-1: Geometrical characteristics of CFB used in this research.

Board Thickness (mm)	4.24
Flute Height (mm)	3.67
Flute Pitch (mm)	8.05
Take-up Factor	1.46

Table 4-2: Properties of the constituent paper that made up the CFB.

Paper	Inner (Kraft)	Flute (Semi-Chem)	Outer (Kraft)
Thickness (mm)	0.320	0.204	0.253
Grammage	257	163	205
Density (kg/m^3)	781	784	791

The tensile testing for each constituent paper that made up the CFB was conducted by a New Zealand research company, Scion, in accordance with the TAPPI T 494 standard. The elastic variables of each paper are given in Table 4-3.

Table 4-3: The average values and standard deviation of some variables for each constituent that was provided by Scion where direction 1 corresponds to MD and direction 2 corresponds to CD.

Variables/Constituents	Outer Liner	Flute	Inner Liner
E_{11} **(MPa)**	8630 ± 680	6790 ± 380	7700 ± 610
E_{22} **(MPa)**	3330 ± 260	2870 ± 390	3060 ± 770
v_{12}	0.20 ± 0.02	0.22 ± 0.02	0.27 ± 0.03
σ_{11t} **(MPa)**	72.7 ± 7.5	54.9 ± 3.5	69.1 ± 3.1

σ_{22t} (MPa)	34.3 ± 1.6	29.8 ± 0.9	31.8 ± 2.2

4.2.2 Experiment

Four-Point Bending Experiment

The details of CFB used in this research has been presented earlier in Table 4-1 and Table 4-2. The virgin CFB panel was cut using an Epilog Fusion M2 laser cutter into 260 x 50.8 mm samples for the four-point bending test in accordance with TAPPI T-811 CM-09. They were cut into five groups of ten samples that were classified by the flute angle relative to the CD direction. Figure 4-1 shows the illustration for each sample group.

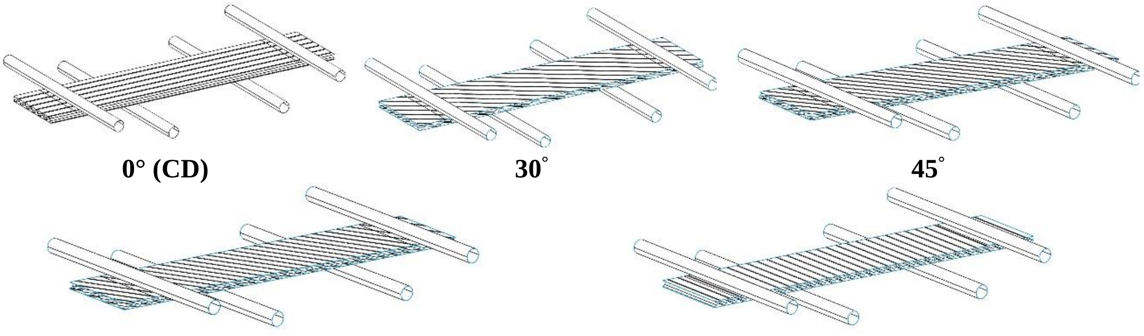

0° (CD) **30°** **45°**

60° **90° (MD)**

Figure 4-1: Illustration of samples oriented at a different angle to carry out the four-point bending test. These are the model samples that were fed to ANSYS to carry out the finite element analysis. Notice the presence of split lines in each sample that acts as a glue region between the flute and the liners.

After the cutting process, the samples were stored in a controlled condition (23°C at 11% RH for at least 48 hours and then 50%RH for at least 24 hours) in accordance to the TAPPI T-402 SP-08 standard. For the four-point bending test schematic diagram, refer to model setup in Figure 4-4. The experimental setup is shown in Figure 4-2.

Figure 4-2: Four-point bending test on 0° CFB carried out by using a texture analyser equipment TA.XT Plus (Texture Technologies Corp.).

A ZX2 Series laser displacement sensor (Omron Corporation) was placed in the four-point bending setup underneath the board to measure the centre deflection of the samples. The test was carried out using a texture analyser equipment TA.XT Plus (Texture Technologies Corp.) with a displacement rate of 12.5 mm/min. From the experiment, the graph of the force against centre deflection was plotted and the bending stiffness was calculated from the following equation: -

$$D = \left(\frac{1}{16}\right)(\Delta)\left(\frac{L_{bottom}^{3}}{w}\right)\left(\frac{a}{L_{bottom}}\right) \tag{4.1}$$

where D is the flexural stiffness (N.m), Δ is the slope of the force against centre deflection graph (N/m), L_{bottom} is the distance between both the bottom anvils (m), w is the width of the sample (m) and a is the distance between the bottom and upper anvil (m).

Figure 4-3 shows a sample of a typical force against centre deflection graph and location of the selected slope.

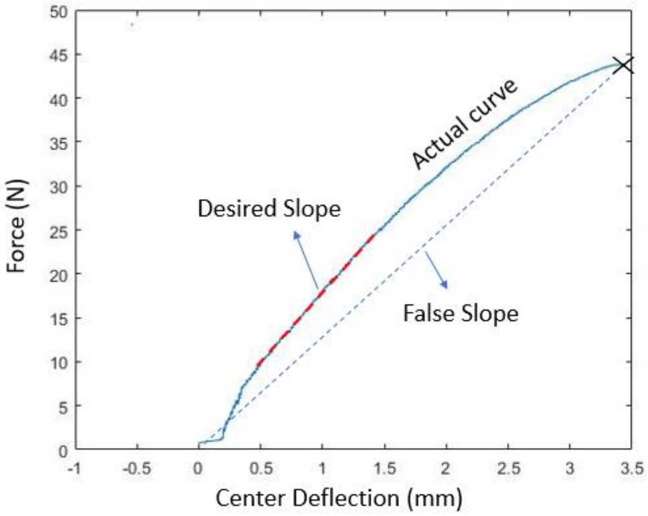

Figure 4-3: Typical force against centre deflection graph measured from the four-point bending experiment.

At 0 – 0.2 mm, the applied load was trying to accommodate the initial slack of the sample. At about 0.2 – 0.3 mm, the initial loading was observed. At 0.3 – 2 mm, the linear region of the curve was observed, and signs of visco-elasticity were seen before reaching the maximum force at about 3.5 mm. The desired slope, as indicated in the figure, was chosen and used in equation (4.1) to obtain the bending stiffness. Figure 4-3 also shows that using point zero and the point of maximum force will result in a false slope measurement.

Edge Crush Test (ECT) Experiment

The same virgin Kraft CFB was used for ECT experiments where ten samples were cut into dimension of 38.1 x 50.8 mm following the TAPPI T-811 OM-17 standard. After cutting the samples, about 6 mm from both ends of all samples were reinforced with bees' wax to prevent failure from occurring in these regions. All samples were then stored in a controlled condition in accordance to the TAPPI T-402 SP-08 (23°C at 11% RH for at least 48 hours and then 50%RH for at least 24 hours).

To ensure the sample was held so that it is vertical, two metal blocks was used in accordance to the TAPPI T-811 OM-17 standard. The ECT test was performed using a texture analyser TA.XT Plus (Texture Technologies Corp.) with a displacement rate of 12.5 mm/min and the maximum force obtained was used to calculate the ECT force by dividing it by the width of the sample (50.8 mm).

4.2.3 *Analytical Solution of Four-Point Bending*

Carlsson et al. (1985) derived an equation to calculate the bending stiffness (D_{22}) along the CD of CFB. The equation considers the tensile stiffness of each constituent paper that make up the CFB together with their thicknesses, the height of the flute and the board, and the moment of inertia of the flute. The equation is given by:

$$D_{22} = S_{2,f1}\left(\frac{(H-t_{f1})^2}{4}\right) + S_{2,f3}\left(\frac{(H-t_{f3})^2}{4}\right) + S_{2,c}\left(\frac{I_{y,c}}{h_f}\right) \tag{4.2}$$

where $S_{2,f1}$ is the CD tensile modulus of the inner paper (N/m), $S_{2,f3}$ is the CD tensile modulus of the outer paper (N/m), $S_{2,c}$ is the CD tensile modulus of the flute paper (N/m), t_{f1} is the thickness of the inner paper (m), t_{f3} is the thickness of the outer paper (m), h_f is the height of the flute (m), H is height of the board (m) and $I_{y,c}$ is the second moment of area of the flute (m^4). The tensile modulus is calculated by multiplying the elastic modulus by the thickness of the constituent paper.

To calculate the moment of inertia of the flute, $I_{y,c}$, Lee and Park (2004) presented a detailed equation which is given by:

$$I_{y,c} = \left(\frac{4\mathrm{w}}{P}\right)\left[\int_0^{\frac{P}{4}} \frac{t_c h_f^2}{4} sin^2\left(\frac{2\pi x}{\mathrm{P}}\right)\sqrt{1+\frac{\pi^2 h_f^2}{\mathrm{P}^2}cos^2\left(\frac{2\pi x}{\mathrm{P}}\right)}\,dx\right] \tag{4.3}$$

where w is the width of the sample (m), P is the flute pitch (m) and t_c is the fluting paper thickness (m).

Urbanik (2001) reported that the stiffness contribution from the flute is negligible when bending the CFB in MD. Hence, the bending stiffness on MD using equation (4.2) was simplified into:

$$D_{11} = S_{1,f1}\left(\frac{(H-t_{f1})^2}{4}\right) + S_{1,f3}\left(\frac{(H-t_{f3})^2}{4}\right) \tag{4.4}$$

where $S_{1,f1}$ is the MD tensile modulus of the inner paper (N/m) and $S_{1,f3}$ is the MD tensile modulus of the outer paper (N/m). The tensile stiffness of each paper, S (N/m), is calculated by multiplying the thickness of the paper with the elastic modulus, E.

Currently, there is no reported work on calculating the bending stiffness at an angle for CFB through analytical solution. As the paper components were assumed as orthotropic, one of the ways to obtain the properties at an angle is through rotation of compliance tensor matrix approach (Electrical Park Research, 2006; Roylance, 2001). Taking this approach, first a compliance tensor, $A(f)$, was calculated from:

$$A(f) = \begin{bmatrix} \frac{1}{E_{11}} & \frac{-v_{12}}{E_{11}} & 0 \\ \frac{-v_{21}}{E_{11}} & \frac{1}{E_{22}} & 0 \\ 0 & 0 & \frac{1}{G_{12}} \end{bmatrix} \qquad Q(f) = A(f)^{-1} \qquad (4.5)$$

where G_{12} was calculated using the relation presented in Table 2-4 of Chapter 2 and *Q(f)* is the stiffness tensor matrix.

To convert the elastic variables to desired angle, θ, a rotation matrix, *T*, that was derived based on force balance equations (refer (Roylance, 2001)) was introduced. For θ, 0 degree corresponds with flute direction on CD while 90 degree corresponds with flute direction on MD.

$$T(\theta) = \begin{bmatrix} \cos^2(\theta) & \sin^2(\theta) & 2\cos(\theta)\sin(\theta) \\ \sin^2(\theta) & \cos^2(\theta) & -2\cos(\theta)\sin(\theta) \\ -\cos(\theta)\sin(\theta) & \cos(\theta)\sin(\theta) & cos^2(\theta) - \sin^2(\theta) \end{bmatrix} \qquad (4.6)$$

Reuter's matrix, *R*, was introduced to define the conversion from tensor to engineering strain:

$$R = \begin{bmatrix} 1 & 0 & 0 \\ 0 & 1 & 0 \\ 0 & 0 & 2 \end{bmatrix} \qquad (4.7)$$

The new stiffness tensor matrix, *Q(f, θ)*, and new compliance tensor matrix, *A(f, θ)*, that accounts for the rotation angle (refer to Electrical Park Research, 2006 for the equation derivation) was then calculated from:

$$Q(f,\theta) = T(\theta)^{-1}\, Q(f)\, R\, T(\theta)\, R^{-1} \qquad (4.8)$$

$$A(f,\theta) = Q(f,\theta)^{-1} \qquad (4.9)$$

The new angled elastic moduli were calculated using the new compliance tensor matrix, *A(f, θ)*:

$$E_{11}^{\theta} = \frac{1}{A(f,\theta)_{1,1}} \quad E_{22}^{\theta} = \frac{1}{A(f,\theta)_{2,2}} \tag{4.10}$$

where E_{11}^{θ} is the elastic modulus in direction 1 when the fibres are rotated at angle θ and E_{22}^{θ} is the elastic modulus in direction 2 when the fibres are rotated at angle θ.

The variables in equation (4.10) were multiplied by their respective paper thickness in Table 4-2 to get the tensile moduli and fed into equation (4.2) to obtain the bending stiffness of CFB at an angle.

4.2.4 Empirical Solution of ECT

The ECT can be calculated based on the equation derived by Markstrom (1999):

$$ECT = k\left(\sigma_{CD,L1} + \sigma_{CD,L2} + \alpha\sigma_{CD,F}\right) \tag{4.11}$$

where $\sigma_{CD,L1}$ and $\sigma_{CD,L2}$ is the compression strength of the liners in CD (N/m), $\sigma_{CD,F}$ is the compression strength of the flute in CD, α is the take-up ratio, and k is the constant that considers the loss of the strength in flute during the converting and the paper testing method. The value of k is determined based the type of compression test conducted on the paper. These can be the ring crush test (RCT), corrugated crush test (CCT) and short-span compression test (SCT). The k value used in this study was for SCT with a value of 0.71. The SCT of the paper components, which was calculated based on the relation in Table 2-4 to give the compression stress and divided by the paper thickness to give the SCT, are given in Table 4-4:

Table 4-4: Compressive strength of each paper components that made up the virgin Kraft C-flute CFB used in this research.

Inner Liner, $\sigma_{CD,L1}$(kN/m)	Flute, $\sigma_{CD,F}$ (kN/m)	Outer Liner, $\sigma_{CD,L2}$ (kN/m)
6.10	3.65	5.21

4.2.5 FE Model

Development of **Flute Geometry**

Urbanik (2001) developed a series of curved arc and straight flank segments to mathematically define the flute geometry as discussed in Chapter 2.5.1. By using this method, the flute calliper (h_f), pitch (P) and take-up ratio (α) of the flute are needed as the input parameters to get the flute tip (R), length of the flank (L) and the angle of the flank (β). Using these three output parameters, a half wave that consists of an arc and tangent curve was drawn in Solidworks. This curve was then extruded into a longer version of the flute and the liners and anvils used to perform the four-point bending test were then added. The final geometry was then transferred into ANSYS version 17.2 to carry out the FE simulation. A combination of static structural and ANSYS Composite PrepPost (ACP) were used to run the FE simulation where static structural was used performs the bending and edge crush simulations, and ACP was used to determine the failure criterion plot.

Material Properties

The paper components of CFB were assumed to behave as orthotropic linear elastic materials in the model. In ANSYS, the first input for the materials properties were the density and thicknesses of the papers which were presented earlier in Table 4-2.

As the CFB in the model was assumed to behave as an orthotropic elastic shell element, the inputs were orthotropic elasticity and orthotropic stress limits for each paper component. The main variables measured from Table 4-3 were used to calculate other variables as presented in Chapter 2.5.2. To summarise, this yielded 18 variables overall as follows in Table 2-4:

Table 4-5:Eighteen variables of orthotropic behaviour that were used as the input into Ansys.

Orthotropic Elastic	**Orthotropic Stress Limit**
E_{11}	σ_{11}
E_{22}	σ_{22}
E_{33}	σ_{33}
ν_{12}	$-\sigma_{11}$
ν_{13}	$-\sigma_{22}$
ν_{23}	$-\sigma_{33}$
G_{12}	τ_{12}
G_{13}	τ_{13}
G_{23}	τ_{23}

where E refers to elastic modulus, v refers to Poisson's ratio, G refers to shear modulus, σ refers to normal stress (positive and negative signs refer to measured under tension and compression), τ refers to shear stress and subscripts *1,2,3* are the directions that aligns with the MD, CD and thickness.

To account for the maximum bending force in the model, the Tsai-Wu failure criterion was implemented following what has been presented by Haj-Ali et al. (2009) where the ultimate failure of CFB is identified when the failed region on the liners reached the full pitch length. The prediction of ultimate force for ECT single-wall board shows reasonable agreement with their experimental findings.

Four Point Bending Model Setup

A surface shell type of shell 181 with four-node element and six degrees of freedom at each node was used to generate the liners and flute in the model. A region of 0.8 mm width (as measured in actual board image) on the flute tips and the liners were connected as a perfect bond while the contact between the anvils and the board was modelled as a frictionless contact. This model did not consider the effect of the glue between flute and the liners for the purpose of simplification. The large deformation setting was turned on to account for the geometric non-linearities in the model and the model was solved using a direct solver through sparse direct matrix method. The four-point bending setup which was based on TAPPI T 820 standard is illustrated in Figure 4-4.

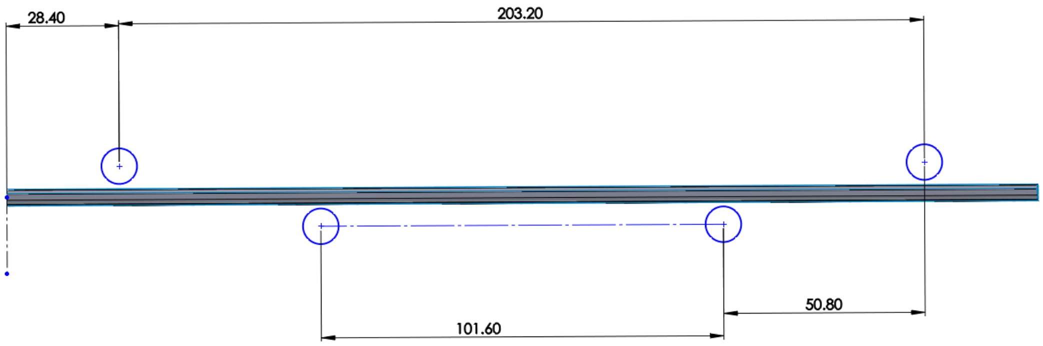

Figure 4-4: Setup of the four-point bending fixture of CFB as per TAPPI T-811 CM-09.

It is also important to note that all the elements were oriented so that the x-direction follows the MD, y-direction follows the CD and z-direction follows the out-of-plane direction of each paper component. For the anvils, the material is structural steel and assumed to be isotropic.

The round edges of the top anvils were displaced by 15 mm downwards in z-direction where the maximum force will be reached within that range for all models and the displacement in the x and y direction was set as fixed. The round edges of the bottom anvil were set as fixed displacement in x, y and z directions. A nodal vertex on the centre of the inner liner was set to be fixed along the y-direction to prevent rigid body motion while the direction of x and z were left free.

A damping coefficient of $2\text{x}10^{-5}$ which has been reported by Allanson and Svard (2001) was added as it has been found to aid convergence caused by localised buckling. The damping coefficient adds viscous forces to the global equilibrium equations and help to reduce convergence issue. All the bodies in the model were meshed as quadrilateral elements with a size of 1 mm as illustrated in Figure 4-5. The number of elements and nodes for each model are summarised in Table 4-6. Further refinement on the mesh was found to not yield any improvement on the results, increased the computational time and caused convergence difficulties in several cases.

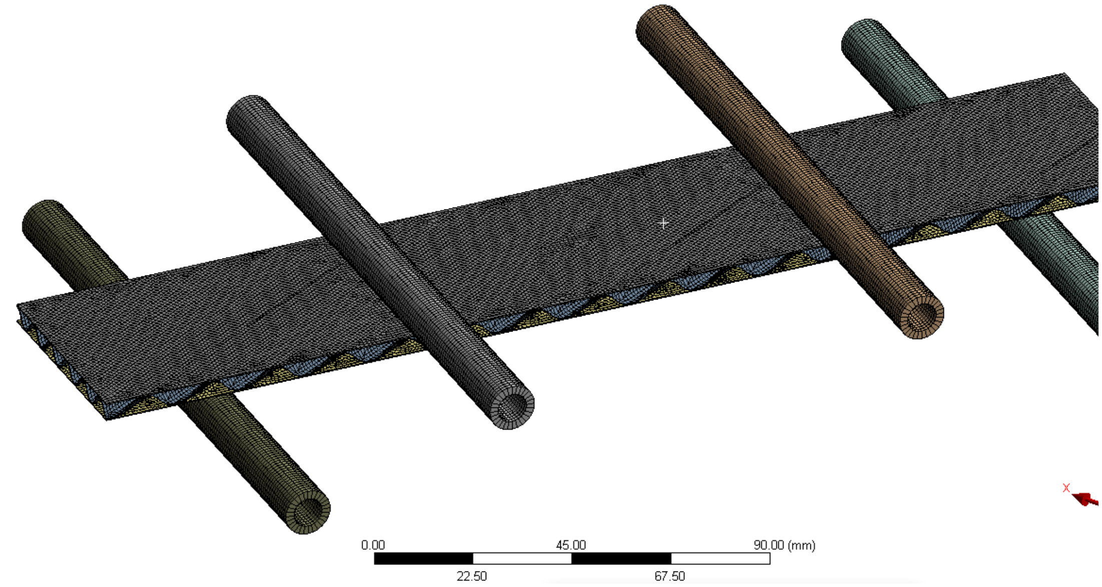

Figure 4-5: Quadratic mesh element with a size of 1 mm on 30° CFB sample.

Table 4-6: The number of mesh elements and nodes for each model of corrugated board.

Groups	**0°(CD)**	**30°**	**45°**	**60°**	**90°(MD)**
Elements	66,396	68,018	67,056	67,372	66,405
Nodes	67,481	68,811	67,770	68,192	67,647

After running the models, the force and centre deflection data were collected and plotted. The data was then processed using Mathworks Matlab 2017a to determine the slope and calculate the bending stiffness of the board based on equation (4.1).

The Tsai-Wu failure plot at twice the displacement of failure initiation from each model was also collected for comparison with the failed region of the experimental samples.

ECT Model Setup

Similar to the four-point bending model, Shell 181 was used for the flute and liners and a region of 0.8 mm on the flute tips and the liners were connected as perfect bond. The large deformation setting was turned on to account for the geometric non-linearities and the model was ran using a direct solver through direct sparse matrix method.

For the ECT model, the setup was based on TAPPI T 811 standard where the sample dimension is 38.1 x 50.8 mm and two regions 6 mm from the top and bottom of the sample were waxed to prevent failure occurring in these regions (see Figure 4-6). To simulate the wax regions in the model, these regions were set as rigid and only allowed to be displaced in the y-direction and to rotate around the x-axis. This helped to prevent failure from occurring in these regions. The top edges were displaced by 1 mm in the negative y-direction and the direction x and z were left free. The bottom edges were fixed in x, y and z directions.

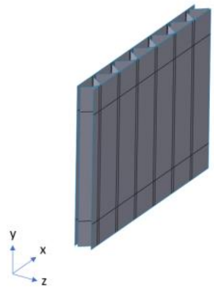

Figure 4-6:Geometry model of an ECT sample based on TAPPI T 811 standard.

A quadrilateral mesh element of 1 mm was used where the total number of elements lay between 7,500 and 7,800. The minimum and maximum substeps were set to 75 and 150 respectively (further increases did not lead to changes in the results). By examining the contour plots of the Tsai-Wu failure criterion, failure was determined when the failed regions (values larger than 1) on the liners reached the length of the pitch.

4.3 Results & Discussion

4.3.1 *Four Point Bending*

Experimental Four-Point Bending

Figure 4-7 shows the bending stiffness and maximum bending force of CFB samples obtained experimentally from the four-point bending test. A one-way ANOVA and Tukey posthoc analysis has been carried out to determine the if differences in the bending stiffness and maximum bending force between each group angles of CFB were significant (Appendix B).

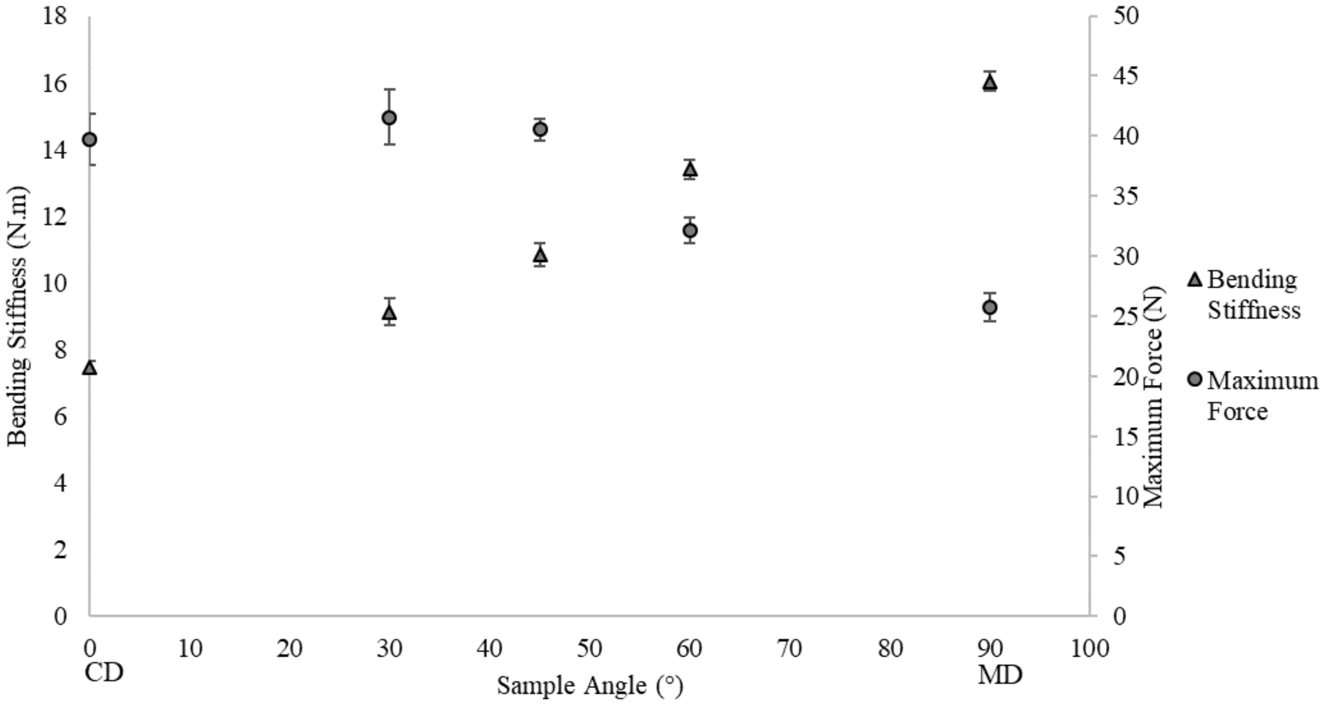

Figure 4-7: Graph of maximum force and bending stiffness of CFB oriented at different angles. The error bars of experiment are +/- 1 standard deviation of population with n=10.

For the bending stiffness of the CFB, it was found out that difference between each group was statistically significant from each other (*p-value <0.05*) with the 90° group being the highest and followed by the 60°, 45°, 30° and 0° groups.

On the maximum bending force of the CFB, the 0°, 30° and 45° groups were found to have no statistically significant difference between each other (*p-value >0.05*). However, those groups were found to be significantly higher than the 60° and 90° groups (*p-value <0.05*).

Although the 90° group had the highest ability to resist bending compared to other groups, it had the lowest maximum force compared to the rest. Commonly, the flutes are orientated vertically on a box panel similar as in 0° group which gives low bending stiffness, but higher maximum force compared to 90° group which means 0° group produces stronger panel but may easily bend or bulge out. However, based on the results in Figure 4-7, the 30° and 45° groups showed an improved bending stiffness without a significant difference in the maximum bending force as compared to the 0° group. This finding agrees with the reported work by Maltenfort (1996) where the compression strength of a diagonal fluted tray was found higher than a regular tray. It might also be advantageous since a box oriented at an angle has been shown to reduce the board area on a blank. Further studies need to be conducted to compare the performance of CFB with 0°, 30° and 45° flute angles as a panel or box as this could possibly improve the top-to-bottom box strength.

Experiment VS Predictions: Bending Stiffness

Figure 4-8 shows the results of the bending stiffness of CFB at different angles calculated from the FE model, analytical solution and experiment. The error bars of the bending stiffness from the FE model were determined by changing the model input parameters by the ± standard deviation of all the variables in Table 4-3.

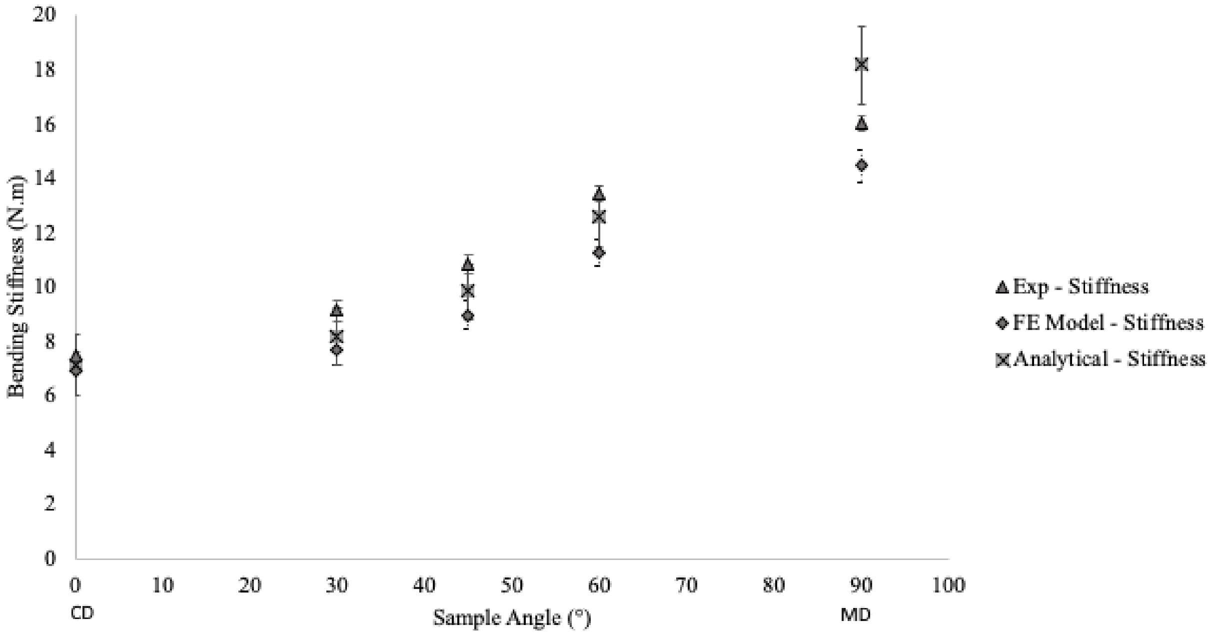

Figure 4-8: Bending stiffness of CFB oriented at different angles comparing the results from the experiment, FE model and analytical model. The error bars of experiment are +/- 1 standard deviation with n=10 while FE model used Monte Carlo approach by generating 100 different dataset based on the properties in Table 4-3. The analytical solution error bars calculated based on analytical uncertainties approach using the variables in Table 4-3.

It was observed that the predicted bending stiffness from the FE model generally underpredicted the experimental results but followed the trend reasonably well between 0° to 90° angles. It was suggested that neglecting the glue that bonds the liners and flute might be the reason for the difference since there will be additional stiffness with the presence of glue (Gilchrist et al., 1999) while approximation of some material constants (such as presented in Section 2.5.2) might also be a reason. Between orthotropic elasticity and orthotropic stress limit, the bending stiffness (in the elastic region) was found to be sensitive to the orthotropic elasticity variables, primarily to the changes in the elastic moduli, E_{11} and E_{22}.

The predicted bending stiffness using the analytical solution was also found to underpredict the experimental stiffness in most cases except at 90°. It is suggested that the overprediction in 90° group was due to the analytical model not considering that the inner liner may be depressed into the void between flutes during bending (resultant of a compressive stress). This effect was considered in the FE model, and present in the experiment which both showed similar trends. Still, the analytical solution provides a reasonable estimation of the actual bending stiffness as it matches closely with the experimental trend. The findings here suggest that the rotation of compliance tensor matrix approach used to rotate the elastic moduli to the desired angle before feeding them into the bending stiffness relation in equation (4.2) works well.

Experiment VS Predictions: Maximum Bending Force

Besides predicting the bending stiffness of CFB, the FE model can also determine the maximum bending force experienced by the sample during the four-point bending test through the plot of Tsai-Wu failure criterion. Figure 4-9 shows a scatter plot of the maximum bending force in each group of samples from the experiment and numerical model results.

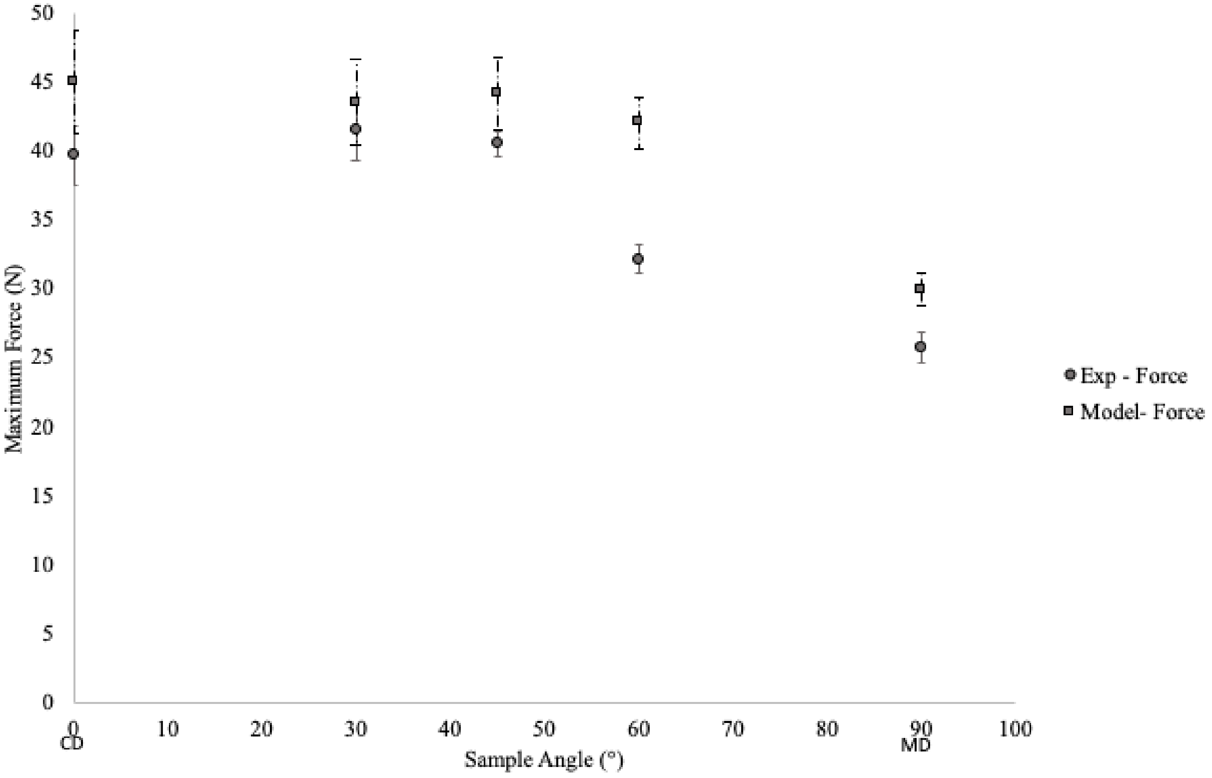

Figure 4-9: Maximum force of each group of samples from the experiment and numerical model of four-point bending test on CFB. The error bars of experiment are +/- 1 standard deviation with n=10 while FE model used Monte Carlo approach by generating 100 different dataset based on the properties in Table 4-3.

It was observed that the maximum bending force from the experiment was similar between 0° to 45° groups (*p-value>0.05*) and started to decrease significantly in the 60° and 90° groups (*p-value <0.05*). The maximum bending force in the FE model showed a similar trend between 0° to 60° angles with 90° being significantly lower than the rest.

At 0° flute angle, it was believed that both the flute and liners were responsible for resisting the bending during the test while at an angle of 90°, the resistance to bending was dominated by the liners (Urbanik, 2001). From this explanation, it was expected that the contribution of the flute at some point decreased with increasing angle. This explains why the maximum bending force at 0° was significantly higher than 90°.

The trend from the experiment shows the maximum bending force starts to significantly decrease between 45° and 60° angles. This suggests that the contribution of the flute in resisting bending continued from 0° up until a point between angles of 45° and 60° where the contribution of flute started to diminish and caused a significant reduction in the maximum bending force. However, in the FE model, the trend showed that the maximum bending force started to significantly decrease between 60° and 90° groups which suggested that the flute and liners still contribute to resisting bending at an angle of 60°.

What this means was that the change in dominance towards liners happens at lower angles from the experimental findings compared to the FE model. A possible reason behind this behaviour might relate to the small irregularities on the fluting medium that was not represented in the model. These irregularities may result from the damage incurred in the corrugating labyrinth for the fluting medium as this has previously been shown to impact its strength (Whitsitt & Sprague, 1987). This may induce failure earlier at 60° angle in the experiment.

In the FE model, the maximum bending force was found to be more sensitive to the orthotropic stress limit as opposed to orthotropic elasticity, primarily on the tensile and compressive stresses in MD and CD which were the main components in Tsai-Wu failure criterion.

There is currently no analytical solution to predict the maximum bending force during bending of CFB despite the bending stiffness being the most sought-after output from this experiment. Thus, FE analysis remains the only modelling option to find the expected maximum bending force.

Experiment VS Predictions: Bending Failure Formation

Figure 4-10 shows the Tsai-Wu failure criterion plot on the model and the test samples after going through the four-point bending test.

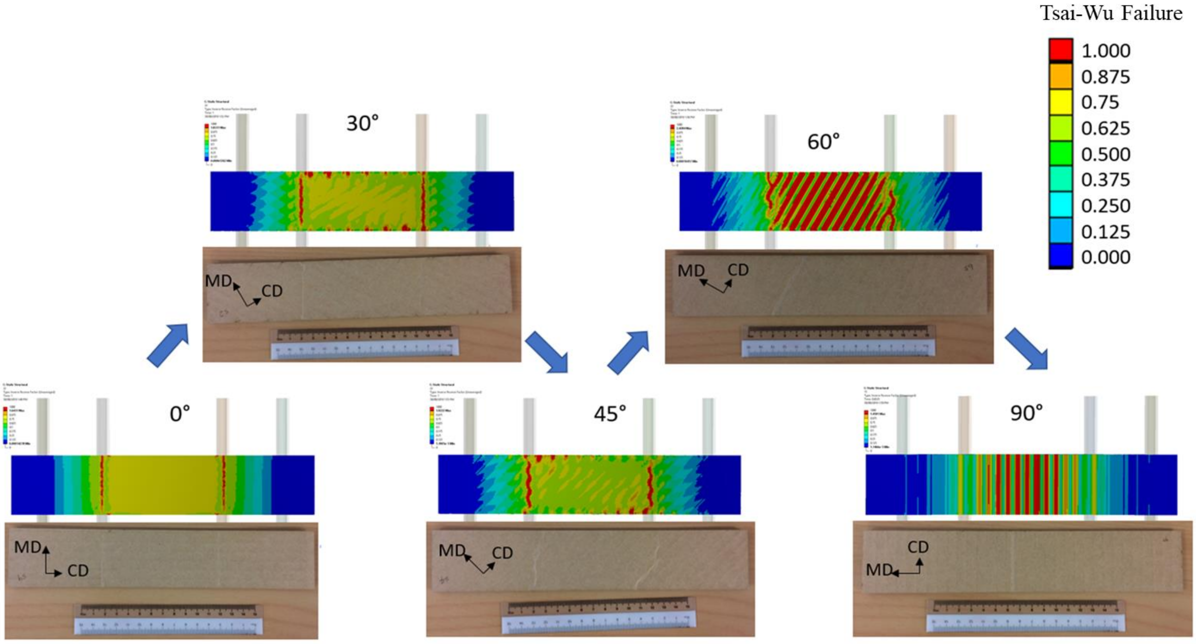

Figure 4-10: Tsai-Wu failure criterion plot and experimental sample after the four-point bending test.

It was observed that the pattern from the models showed excellent agreement with the experimental samples. For the 0° and 30° samples, the failure plot shows that a straight crease line formed just underneath the bottom anvils which were also seen in the test samples. For the 45° sample, both the failure plot and experimental samples showed that the crease forms a combination of lines that are parallel to the width and parallel to the CD. For the 60° and 90° groups, both the failure plot and the experimental sample showed that failure was dominated by formation of crease lines parallel to the CD. The agreement in the failure pattern between the model and the experiment provides further evidence of the reliability of the model.

4.3.2 ECT: Experiment VS Predictions

Figure 4-11 shows the result of ECT obtained from the experiment, FE model simulation and analytical solution.

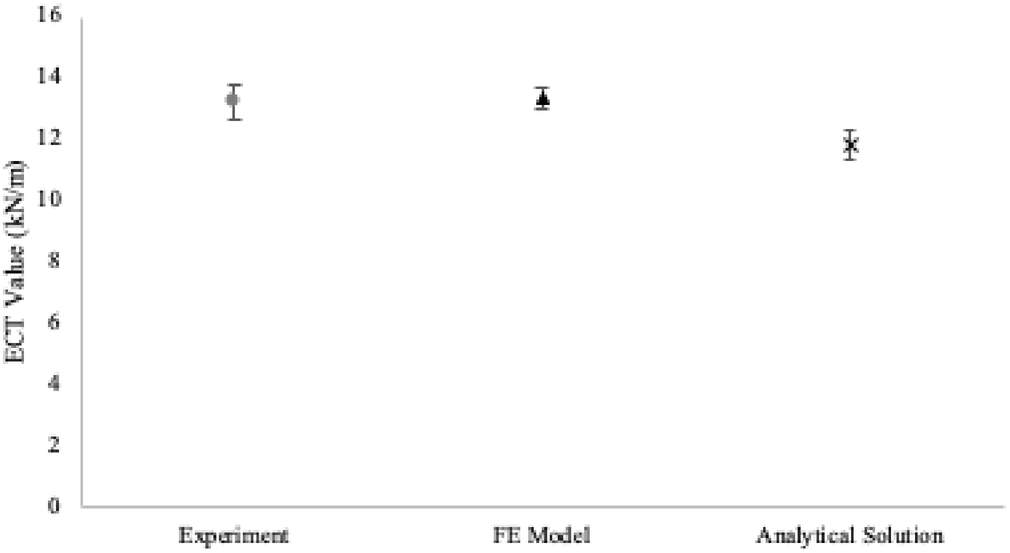

Figure 4-11: The results from ECT experiment, FE model and analytical solution. The error bars of experiment are +/- 1 standard deviation with n=10 while FE model used Monte Carlo approach by generating 100 different dataset based on the properties in Table 4-3. The analytical solution error bars calculated based on analytical uncertainties approach using the variables in Table 4-3.

It was observed that the result from the FE model accurately predicted the ECT force from the experiment. The result from the analytical solution was lower than both experimental and FE model but still matched reasonably well. It is likely that the deviation of the analytical solution was higher than the FE model due to its dependency to less variables which could lead to higher sensitivity in change of the variables value.

Figure 4-12 shows the comparison between the experimental sample and FE model sample analysed using Tsai-Wu failure criterion at different stages throughout the edge crushing process.

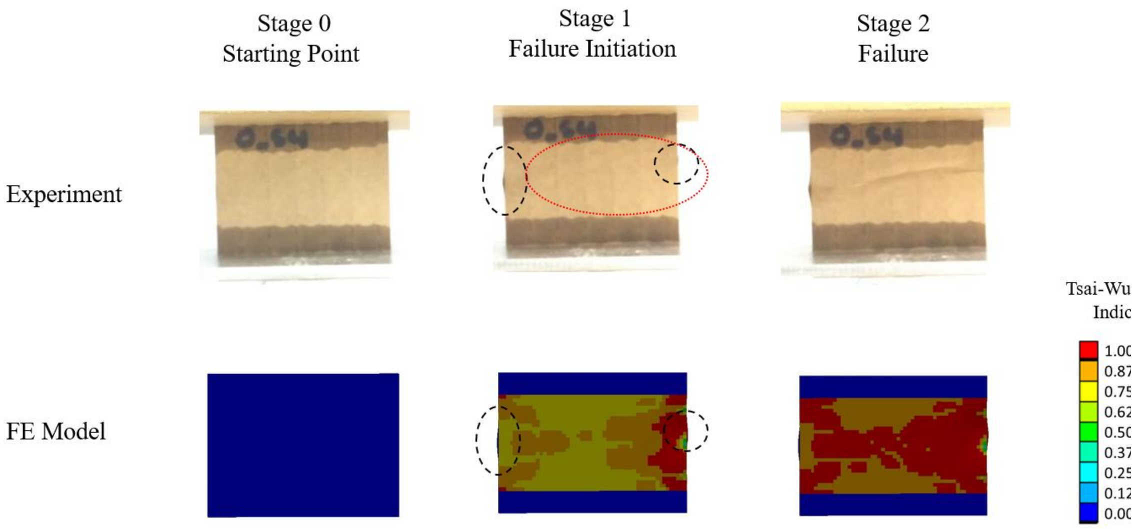

Figure 4-12: Comparison between the failure of ECT sample in the experiment and failure in FE model as determined using Tsai-Wu failure criterion. Sample size was 38.1 x 50.8 mm.

Images from stage 0 were obtained at the start of the experiment. At stage 1, during which failure started to initiate, small parts of the fluting medium were observed overhanging outwards in both the experiment and FE model as indicated by the black dashed circles. This was due to the compressive force that tends to crease the sample. It was also evident that the right part of the liner from the FE model started to experience failure during this stage. By comparing the experimental sample image between stage 0 and stage 1, there was also signs of crinkling on the liner as indicated by the red dotted elipse. At stage 2, when the samples experienced failure, both the experiment and FE model showed crease formation along the width of the sample.

From the findings, it was shown that analytical solution can provide reasonably accurate predictions of the ECT force of CFB using the constituent papers compressive properties. The FE model that considered more constituent papers properties allowed a better prediction and detailed analysis of the ECT with the inclusion of accurate failure analysis of the sample.

4.4 Conclusion

In the four-point bending experiment, the bending stiffness of all the samples was positively correlated with the flute angle with an almost linear relationship observed. The maximum bending force initially did not vary significantly with increasing angles up to 45° ($p\text{-value} > 0.05$) but decreased for 60° and 90° groups ($p\text{-value} < 0.05$).

The FE model and analytical solutions predicted the trend of the bending stiffness of the CFB from 0° to 90° groups reasonably well compared to the experimental findings. It was found that rotation of compliance tensor matrix approach coupled with the bending stiffness relation for CFB works well in predicting the bending stiffness of CFB at an angle through analytical solution.

The maximum bending force predicted in the FE model also showed a similar trend to the experimental data except that significant reduction in maximum bending force was only observed at 90° in the model. The Tsai-Wu failure plots in the FE model justify the reliability of the model as they showed excellent agreement with the locus of failure from the experimental samples.

From the ECT findings, the analytical solution showed that it can predict the ECT force with reasonable accuracy. The FE model allowed for a more accurate predictions of the ECT and it could also capture the failure locus of the CFB sample and failure progression throughout the test.

The FE models developed in this work provide a sound basis for further exploration of how CFB performance is affected by damage to CFB structure in Chapter 6 and Chapter 7.

.

Reference

Allansson, A., & Svärd, B. (2001). Stability and Collapse of Corrugated Board-Numerical and Experimental Analysis (Master's Thesis). Lund University, Sweden 2001

Carlsson, L., Fellers, C., & Jonsson, P. (1985). Bending stiffness of corrugated board under special consideration of asymmetrical and multiply construction. Das Papier, 39(4): 149-156

Gilchrist, A., Suhling, J., & Urbanik, T. (1999). Nonlinear finite element modeling of corrugated board. The 1999 ASME Joint Applied Mechanicals and Materials Division Meeting. Blacksburg, New York, USA; pp. 101–106.

Haj-Ali, R., Choi, J., Wei, B.-S., Popil, R., & Schaepe, M. (2009). Refined nonlinear finite element models for corrugated fiberboards. Composite Structures, 87(4), 321-333.

Lee, M. H., & Park, J. M. (2004). Flexural stiffness of selected corrugated structures. Packaging Technology and Science, 17(5), 275-286.

Maltenfort, G. G. (1996). Corrugated shipping containers: An Engineering approach: Jelmar Publishing Company.

Markstrom, H. (1999). Testing methods and instruments for corrugated boards. Lorentz and Wettre, Kista, Sweden.

McKee, R., Gander, J., & Wachuta, J. (1963). Compression strength formula for corrugated boxes. Paperboard Packaging, 48(8), 149-159.

Nevins, A. (2008). Significant factors affecting horticultural corrugated fibreboard strength. PhD Thesis. Massey University. Retrieved 15 June, 2010, from Massey Research Online.

Electrical Park Research (2006). Effect of Orientation on Stiffness of Aligned Fibre Composites. Michigan Tech University, 2006; Michigan, USA. Accessed on 26th

June 2019 from http://www.mse.mtu.edu/~drjohn/my4150/compositesdesign/cd3/cd1.html

Roylance, D. (2001). Transformation of stresses and strains[online], report, Massachusetts Institute of Technology, 2001; Cambridge, Massachusetts, USA. Accessed on 26th June 2019 from http://web.mit.edu/course/3/3.11/www/modules/trans.pdf

Urbanik, T. (2001). Effect of corrugated flute shape on fibreboard edgewise crush strength and bending stiffness. Journal of Pulp and Paper Science, 27(10), 330-335.

Whitsitt, W., & Sprague, C. (1987). Compressive strength retention during fluting of medium: strength losses in fluting. Tappi Journal, 70(2), 91-96.

Chapter 5.

Impact of Crushing on the Structural and Mechanical Performance of Corrugated Fibreboard

---

Preface

This chapter is focussed on characterising the sensitivity of different mechanical performance tests of CFB to the levels of crushing on the board. It was also of interest to find out how the flute structure responds to crushing and the correlation between flute geometry and mechanical performance. The performance tests used in this chapter were bending stiffness, edge crush test, dynamic stiffness testing (DST) and quantifying the flute morphology using the techniques developed in Chapter 3.

5.1 Introduction

In Chapter 2, McKee’s semi-empirical equation was presented that shows the compression strength of a CFB box depends on the bending stiffness, ECT and perimeter. McKee’s equation showed that mechanical performance of CFB components such as bending stiffness and ECT are the important factors of a box compression strength and its use reduces the need for costly box testing. This is recognised across the packaging industry and included in commercial software for packaging design such as Cape Pack (Esko), TOPS Pro (TOPS Software Corporation) and ModelPACK (Innventia) (Sohrabpour & Hellström, 2011).

Popil et al. (2007) suggested that the transverse shear rigidity may also impact the loss of compression strength of CFB box. This implies that torsional stiffness may have an impact to the box strength that is not captured by the mechanical performance components in McKee’s equation. Torsional stiffness of CFB can be measured through a torsional pendulum approach using a dynamic stiffness tester (DST) instrument that were designed by Ian Chalmers (Chalmers, 2006; Chalmers, 2007). Guo (2016) reported that the measured board performance indicator (BPI) from the DST showed a strong sensitivity towards flat crushing.

In Chapter 3, the importance of the flute morphology was demonstrated and how it can be significantly affected through different levels of flat crushing on the board. Overall, the differences in flute profiles were quantified by the SF value and changes in geometric features such as peak and trough curvatures and flank angles were also described.

The main objectives of this chapter were to investigate the influence of crushing on the mechanical performance of CFB and to compare the changes in the flute morphology to the changes in the mechanical performance. The performance tests used in this research study were four-point bending test, ECT, DST and flute morphology.

5.2 Materials and Methodology

5.2.1 *Preparation of Samples*

Virgin Kraft C-flute CFB panels with dimensions 320 mm x 280 mm were pre-crushed to five different levels (12.5%, 25%, 50%, 75% and 87.5% of the calliper) using an Instron 1195 series IX automated material testing machine at a crosshead speed of 12.5 mm/min. These levels of crush represent how much the panels were crushed and not the final calliper of the crushed panels as some of the displacement that occurred during the process was recovered after the load was removed. Uncrushed panels were also included as the reference point and the basis for calculation of the similarity factor (SF). Each level of pre-crush consisted of ten panel samples, resulting in sixty panels overall.

From each panel, samples for five tests were obtained, consisting of four point bending samples on MD and CD (50.8 mm x 260 mm), an ECT sample (38.1 mm x 50.8 mm), a DST sample (25 mm x 125 mm) and five thin strips for flute morphology analysis (1 mm x 80 mm). These samples were cut using a 120-Watt Fusion M2 (Epilog Laser). For the ECT samples, about 6 mm from both ends of samples were reinforced with bees' wax to prevent failure from occurring in these regions. All the samples were then stored in a standard conditioning room (23°C, 50%RH) as per TAPPI T-402 SP-08.

5.2.2 Test Setups

Four-Point Bending and ECT

The four-point bending and ECT tests were set up in accordance to the TAPPI T-811 CM-09 and T-811 respectively. The details of the setup were explained in Chapter 4.2.5. The bending stiffness was measured in both CD and MD directions.

Dynamic Stiffness Tester (DST)

The torsional stiffness was performed by applying torsion on the samples using a DST model Korutest beta (see Figure 5-1). The test worked by clamping both ends of the sample, with one end fixed and the other allowed to rotate through a small angle of twist. The rotating end has a built-in counterweight to allow for torsional pendulum motion. As the rotating clamp was released from the initial twisting, the oscillations generated a damped sinusoidal curve from which the angular frequency, ω, can be determined. The torsional stiffness can be calculated by:

$$\text{Torsional Stiffness} = (\text{Angular Frequency})^2 \text{ x Moment of Inertia} \qquad (5.1)$$

However, the moment of inertia is assumed as a fixed constant in this case as it alters slightly depending on the sample thickness (Chalmers, 2009). With the moment of inertia fixed, the angular frequency squared is directly proportional to the torsional stiffness. The DST reports the result in BPI units which was calculated by dividing the angular frequency by 100 with one unit carried after the decimal point.

Before the start of the experiment, the DST was calibrated using a supplied steel rod with a known *BPI* which lies between 26.0 – 26.7. The experiment was designed to specifically performed on samples orientated in MD (Chalmers, 2009).

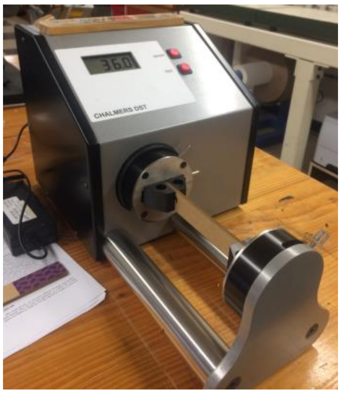

Figure 5-1: Illustration of the DST experimental setup conducted on 25 mm x 125 mm sample of CFB.

Flute Morphology

The thin strips analysed using the methodology outlined in Chapter 3. The samples were aligned on a jig and the image was captured using a Nikon D3100 camera with 18 – 55 mm lens and placed at 550 mm from the samples (see Figure 3-15). The digital images of the thin strips were then used to quantify the morphological changes on the flute profiles relative to the average of the five uncrushed flute profile in each sample. This analysis has been validated in Chapter 3 and was shown to be a promising tool to understand morphological damage on flute profile of CFB.

5.2.3 One-way Analysis of Variance (ANOVA)

To determine the significance between each level of crushing and the different tests used to quantify the performance of CFB, a one-way ANOVA statistic tool was run separately on the different measures of performance (dependent variable) to understand the significancy between each crushed level. There are six assumptions in running the one-way ANOVA in which all of it has been met. The assumptions are:

1. One dependent variable measured at continuous level (different measures of performance)
2. One independent variable that consists of two or more categorical and independent groups (different level of crushing)
3. Independence of observation where there was no relationship between the observations in each group of independent variable
4. There was no significant outliers in the groups of the independent variable in terms of the dependent variable as measured through box plot
5. Dependent variable were normally distributed in each group of independent variable as measured through Shapiro-Wilk test
6. Homogeneity of variance was met through Levene’s test of equality of variances

Along with the one-way ANOVA, Tukey post hoc analysis test was also used as an extension to compare the results between each group of independent variable.

5.3 Results & Discussion

5.3.1 Reliability of the Performance Tests

The one-way ANOVA showed that there were statistically significant differences in all performance measurements between the different levels of crushing:

- Bending Stiffness CD, $F(5,54) = 489.61$, $p<0.0005$; partial $\eta^2 = 0.978$
- Bending Stiffness MD, $F(5,54) = 1429.77$, $p<0.0005$; partial $\eta^2 = 0.993$
- ECT, $F(5,54) = 76.61$, $p<0.0005$; partial $\eta^2 = 0.876$
- DST, $F(5,54) = 951.34$, $p<0.0005$; partial $\eta^2 = 0.989$
- SF, $F(5,54) = 3580.29$, $p<0.0005$; partial $\eta^2 = 0.997$

The findings from the one-way ANOVA suggested that all the tests can be used as reliable tools in measuring the response of CFB to different levels of crushing.

5.3.2 Bending Stiffness of CFB

Figure 5-2 shows the result of the four-point bending test on CD and MD conducted on CFB samples at different levels of crush. The data is reported as mean and standard deviation. The Tukey post hoc analysis outcome to compare the significance between each group of samples is reported in Appendix C.

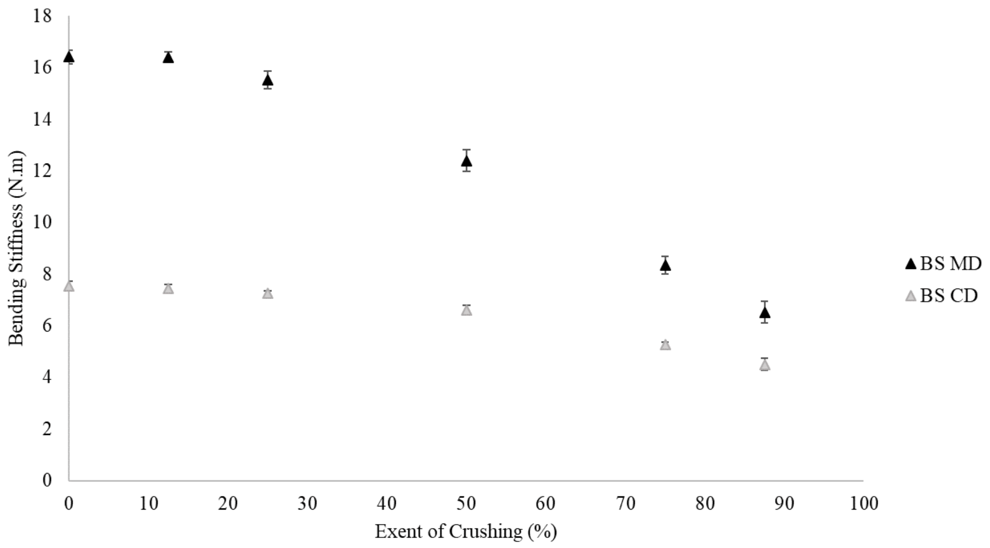

Figure 5-2: Bending stiffness on CD and MD for samples of CFB at different crush levels. Error bars are +/- 1 SD (n=10)

Although there was a slight decrease in bending stiffness in CD from 0% (7.55 ± 0.19 N.m) to 12.5% (7.45 ± 0.17 N.m) crushed samples, the Tukey post hoc analysis showed that there was no statistical difference between them (*p-value>0.05*). Similarly, there was a slight decrease between 12.5% and 25% (7.24 ± 0.12 N.m) crushed samples, but there was no statistically significant evidence found (*p-value>0.05*). However, there was a significant decrease between samples of crushed level 0% and 25.0% (*p-value<0.05*). The bending stiffness on CD then showed a significant dropping trend between each crushed level as level of crushing progressed beyond 25%.

On bending in MD, there was no significant difference observed in the bending stiffness on MD between the 0% (16.42 ± 0.26 N.m) and 12.5% (16.40 ± 0.20 N.m) crushed levels (*p-value>0.05*). As the crushed level progressed beyond 12.5%, the Tukey post-hoc analysis revealed a statistically significant drop in the bending stiffness of MD between each level of crushing.

5.3.3 *Edge Crush Test (ECT)*

Figure 5-3 shows the result of the edge crushing behaviour conducted through ECT on CFB samples at different levels of crushing. The data is reported as mean and standard deviation. The Tukey post hoc analysis to compare the results between each group of samples is reported in Appendix C.

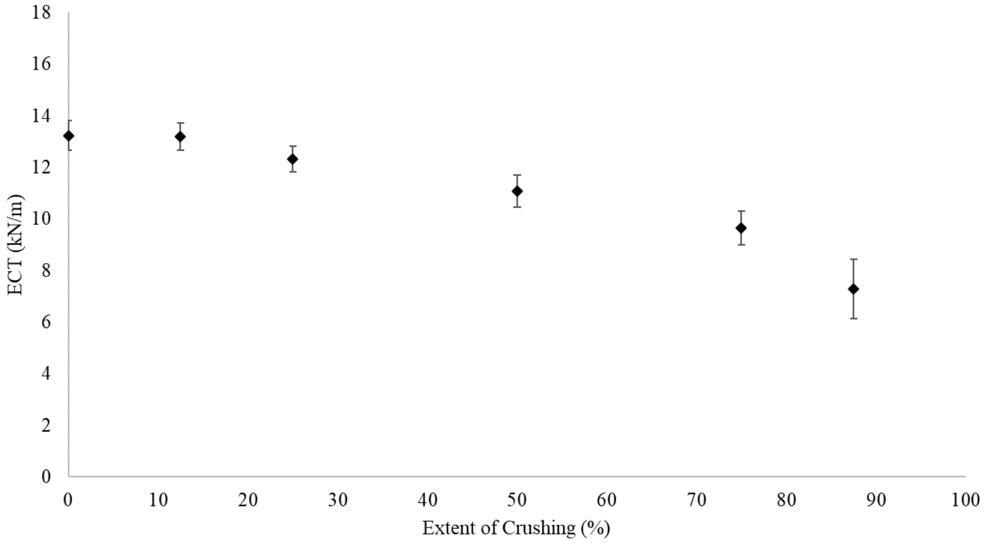

Figure 5-3: ECT results for samples of CFB at different crush level. Error bars are +/- 1 SD (n=10)

It was observed that there was no statistically significant drop in the ECT between the 0% (13.23 ± 0.57 kN/m) and 12.5% (13.19 ± 0.52 kN/m) crushed samples (*p-value>0.05*). Although a slight drop was observed from the first two crushed levels to the 25% (12.31 ± 0.49 kN/m) crushed level, the Tukey post hoc analysis revealed that there was no statistically significant difference between all three (*p-value>0.05*). The crushing behaviour started to show statistically significant drop between each crush level as the samples were crushed beyond 25%.

5.3.4 *Torsional Stiffness*

Figure 5-4 shows the result of the torsional stiffness behaviour measured through conducting DST on CFB samples at different level of crushing. The data is reported as mean and standard deviation. The Tukey post hoc analysis outcome to compare the significance between each group of samples is reported in Appendix C.

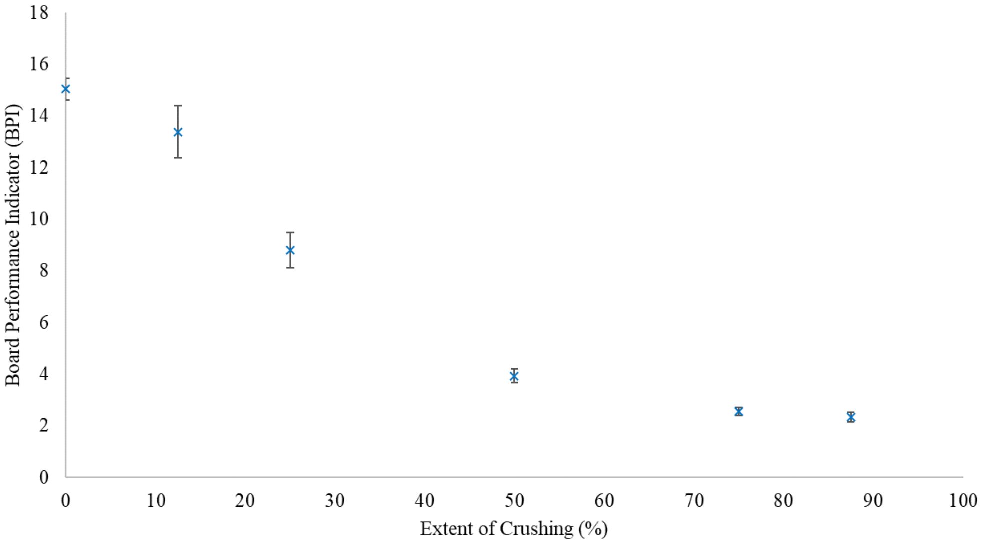

Figure 5-4: DST results for samples of CFB at different crush level. Error bars are +/- 1 SD (n=10)

Unlike in the previous three cases, the torsional stiffness behaviour as measured using BPI dropped significantly between crush levels of 0% (15.05 ± 0.42 BPI) and 12.5% (13.38 ± 1.00 BPI) (*p-value<0.05*), which suggested that crushing CFB has a huge impact on its torsional stiffness performance. The trend in showing a statistically significant drop in the BPI between each crushed level continued until 75%. Between 75% (2.54 ± 0.16 BPI) and 87.5% (2.34 ± 0.19 BPI) crushed levels, there was no statistically significant difference observed.

As mentioned in section 5.2.3, DST depends on the torsion pendulum as a result from the initial twisting on the rotating clamp. It was observed experimentally that as the level of crushing increases, the torsion pendulum twist became weaker and in most 75% and 87.5% crush level samples, the test had to be repeated as the torsion pendulum twist was too weak and it did not generate enough oscillations for it to output a result. This explains the reason why there was no significant difference found between samples of 75% and 87.5% crushed levels as the torsional stiffness of these samples were already out of the equipment's measurement range.

5.3.5 Flute Morphology

Figure 5-5 shows the result of the flute morphology differences measured through the Similarity Factor (SF) obtained through images of thin strips from CFB samples at different level of crushing. The Tukey post hoc analysis outcome to compare the significance between each group of samples is reported in Appendix C.

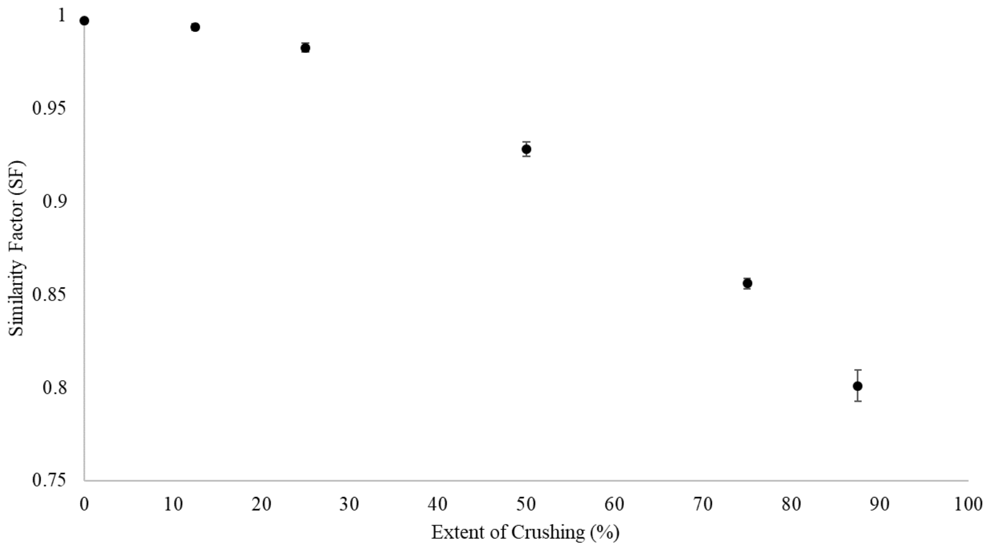

Figure 5-5: Similarity factor of the flute morphology of CFB at different crush level. Error bars are +/- 1 SD (n=50, 5 replicates of 10 samples)

There was no statistically significant difference observed between 0% and 12.5% crush levels (*p-value>0.05*). While there was no statistical evidence in their difference, conversely there was no overlap between the mean and standard deviation of 0% (0.9971 ± 0.0010) and 12.5% (0.9937 ± 0.0018) crushed levels which showed that SF still has the ability to differentiate the difference in flute morphology of 0% and 12.5% crushed samples. As the level of crushing progressed beyond 12.5%, a statistically significant drop between each group was observed (*p-value<0.05*).

It is also observed that the 87.5% crushed level showed a large standard deviation relative to other crushed levels. To find out the reason behind this behaviour, the additional features in the flute morphology analysis (flank angle, peak-trough skewness) was applied. This analysis showed that as the level of crushing progressed, the average flank angle of the flute on both peak-trough and trough-peak started to skew away (see Figure 5-6). The difference in average was found to be the highest at the 87.5% crushed level, which suggested a shear deformation type of damage. Additionally, the standard deviations on both peak-trough and trough-peak flank angles at the 87.5% crushed level still showed some overlap which suggested that there may be a mix of samples experiencing flat crushed damage and shear deformation types of damage.

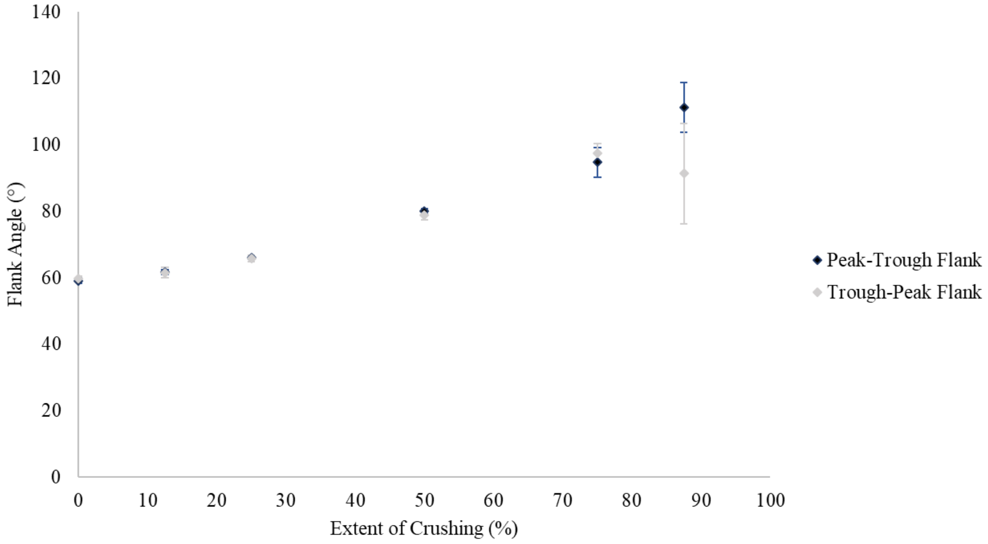

Figure 5-6: Flank angle of the flute that were obtained from the flute morphology analysis as an additional feature to describe the geometry of the flute (another descriptor feature, the radius of curvature on peaks and troughs, are presented in the Appendix C). Error bars are +/- 1 SD (n=50, 5 replicates of 10 samples)

To support this explanation, an observation on images from 87.5% crushed samples was carried out. Figure 5-7 shows the evidence of flat crushed dominated damage (a) and shear crushed dominated damage (b) samples. This could be due to manufacturer defects especially during blank stacking as a small skew on the angle of the flute towards one way on the virgin sample could easily induce shear failure.

Figure 5-7: Evidence of a) flat crushed dominated damage sample and b) shear crushed dominated damage sample.

The evidence of the existence of the two types of flute damage in the 87.5% crushed level explains the reason for the large standard deviation observed in Figure 5-5.

5.3.6 Discussion

The one-way ANOVA revealed that each test showed significant sensitivity in response to different crushing levels on CFB. This justifies that all the performance tests are useful and reliable in measuring the impact of crushing on CFB.

In the first two levels of crushing (0% and 12.5%), aside from DST, all tests showed no statistical differences. This suggested that DST has the highest sensitivity to damage at low crushing levels, justifying Popil et al.'s (2007) suggestion that the crushing of CFB may impact its shear resistance behaviour. It is also interesting to point out that the flute morphology did not show any statistically significant difference between these levels of crushing whereas the DST did. This suggests that the torsional behaviour may not be dependent on the change of the flute morphology and could mean that the crushing causes other localised damage to the fibres in the constituent papers. Since the ECT and bending stiffness (the biggest factor affecting box compression strength McKee et al. (1963)) was not affected significantly during this stage, it will be interesting to see whether the change in torsional behaviour of CFB box could affect the actual box compression strength in future studies.

As the level of crushing progressed further to 25%, the bending on MD, DST and flute morphology analysis all showed statistically significant drops compared to the 12.5% crush level but the bending stiffness in CD and ECT remained insensitive to crushing between these levels. All tests then showed a significant drop between each crushed level as the level of crushing progressed beyond 25% except for DST in measuring the difference between 75% and 87.5% crushed levels due to the samples may already be out of the equipment's measurement range.

In general, the bending stiffness, ECT and flute morphology analysis showed a similar response towards the crushing levels where there was a slow drop in the first three levels of crushing and bigger drop as the crushing progress. Bending stiffness is known sensitive to the calliper change as reported from equation (4.2) and (4.4) while ECT is associated to compressive stress rather than the calliper as reported from equation (4.11). The flute morphology on the other hand, measures the change in the structure of the flute which also includes the change in calliper. The similarity in the response of all these tests toward the crushing levels may suggest that both bending stiffness and ECT are strongly related to the flute morphology. This will be the main topic of discussion in the next chapter.

5.4 Conclusion

From the findings in this chapter, it was proven from the one-way ANOVA that all the performance test showed good reliability in measuring the response of CFB towards different crushed levels.

The DST showed the highest sensitivity in response to crushing with significant differences between the measured values at crush levels of 0% and 12.5% where other tests showed no such differences. It is suggested that the torsional behaviour as measured through DST could be affected by other localised damage to the fibres of the constituent papers since the effect of flute morphology was already eliminated through the SF measurement. The DST however, showed no significant difference between 75% and 87.5% as it was out of the equipment's sensitivity range.

Bending stiffness, ECT and flute morphology analysis all showed a similar response of dropping in general which suggest the mechanical performance tests are strongly related to the change in flute structure when crushed at different levels. This will be further investigated and discussed in the following chapter.

Reference

Chalmers, I. (2009). Method and apparatus for testing of shear stiffness in board. U.S. Patent No. 7,621,187. 24 Nov. 2009.

Chalmers, I. R. (2006). A new method for determining the shear stiffness of corrugated board. Appita Journal, 59(5), 357-361.

Chalmers, I. R. (2007). The use of MD shear stiffness by the torsional stiffness technique to predict corrugated board properties and box performance. 61st Appita Annual Conference and Exhibition, Gold Coast, Australia 6-9 May 2007: Proceedings.

Guo, Z. (2016). Torsional Stiffness of Corrugated Paperboard (Masters dissertation). Miami University, Ohio, USA.

McKee, R., Gander, J., & Wachuta, J. (1963). Compression strength formula for corrugated boxes. Paperboard Packaging, 48(8), 149-159.

Popil, R. E., Coffin, D. W., & Habeger, C. C. (2007). Transverse shear measurement for corrugated board and its significance. 61st Appita Annual Conference and Exhibition, Gold Coast, Australia 6-9 May 2007: Proceedings.

Sohrabpour, V., & Hellström, D. (2011). Models and software for corrugated board and box design. 18th International Conference on Engineering Design (ICED 11), Impacting Society through Engineering Design, Vol. 10: Design Methods and Tools pt. 2, Lyngby, Copenhagen, Denmark 15-19 August 2011. Proceedings

Chapter 6.

Modelling the Impact of Crushing on the Strength Performance of Corrugated Fibreboard

---

Preface

In this chapter, the models developed in Chapter 4 are applied to predict the performance of CFB at different extents of crushing as and validated against the experimental data collected in Chapter 5. One of the ways to do this was to apply the flute morphology data collected using the techniques developed in Chapter 3 to define the input geometry to the models.. This provided a good representation of the actual crushed geometry of the flute in the model.

The main objective of this chapter was to investigate the sensitivity of the calliper and flute morphology in predicting the mechanical performance of CFB; bending stiffness and ECT. Three different models of increasing complexity were used in this chapter. These were analytical solution, an equivalent finite element (FE) model, and a micro geometry models that used the real and idealized flute geometry. The output from these models were compared with the experimental output that were discussed in Chapter 5. DST was not included as it requires the dynamic response of CFB whereas the modelling work of this thesis is focussed on static model.

Part of this work on the FE equivalent model was developed by the author's co-supervisor, Dr. Celia Kueh. The author then used the model to compare the predictive power of this to the other models. The work and outcome from using the equivalent FE model in getting the results used in this chapter was done by the author.

The work from this chapter was published in:

Jamsari, M. A., Kueh, C., Gray‐Stuart, E. M., Dahm, K., & Bronlund, J. E. (2020). Modelling the impact of crushing on the strength performance of corrugated fibreboard. Packaging Technology and Science.

6.1 Introduction

Chapter 2.3, discussed that crushing on CFB can occur during manufacture, conversion, erecting, packing and distribution. This can impact the structure of the flute and reduces the mechanical strength performance as demonstrated in Chapter 5. This will result in having a weaker box that is unable to protect its contents properly.

To reduce experimental overhead in understanding how flute profile influences the mechanical performance, researchers have developed several models such as analytical solutions, finite element (FE) shell models and more complex micro geometry models using idealized or real flute geometries. We have demonstrated the use of the analytical solutions and idealized flute geometries in Chapter 4 with a positive outcome.

Analytical or shell models have the advantage of low computing overhead but the models generally only account for the CFB calliper. The more complex FE analyses such as those based on detailed flute geometries can allow consideration of how flute geometry influences the strength.

In chapter 5, image analysis tools, using the skeleton analysis developed in Chapter 3 were used to characterise the real flute geometries after crushing CFB samples. This allows for a detailed FE analysis that considers the change in flute morphology due to the crushing on CFB.

This chapter compares the predictive performance of the analytical, FE equivalent shell, and ideal and real shape micro geometry FE models for crushed CFB under four-point bending in both MD and CD directions, and ECT performance. Since DST captures the dynamic behaviour of CFB through the angular frequency of the torsional pendulum motion, it was not considered in this thesis since it may require the viscoelastic property that represent the strain rate dependent elastic behaviour and that the modelling work focus on static model.

6.2 Materials and Methodology

6.2.1 Preparation of Samples

The preparation of samples for different levels of crushing on CFB was presented in Chapter 5.2.1. Table 6-1 shows the pitch and height of the flute for undamaged sample (0%) and the remaining pre-crushed samples. Using the skeleton analysis developed in Chapter 3, the geometry of the pre-crushed flute was extracted. The flute pitch was obtained by calculating the horizontal distance between the centre of the peaks and the flute height was computed from the vertical distance between the peaks and troughs.

Table 6-1: Pitch and height of the flute for different pre-crushed level samples measured electronically using Matlab R2018a (MathWorks Inc.) based on the methodology described in Chapter 3.

Extent of crushing	**0%**	**12.5%**	**25%**	**50%**	**75%**	**87.5%**
Pitch, P (mm)	8.08±0.07	8.04±0.05	8.03±0.15	8.05±0.06	8.05±0.06	7.96±0.06
Height of Flute, h_c (mm)	3.64±0.03	3.55±0.03	3.45±0.03	3.13±0.03	2.69±0.03	2.62±0.06

The four-point bending and ECT samples were then obtained from the pre-crushed samples. The experimental work and results of the four-point bending and ECT was presented in Chapter 5.

6.2.2 Tensile Properties of Paper Component

The board used in this chapter is the same single wall virgin Kraft C-flute CFB supplied by Oji Fibre Solutions that was used in the model development outlined in Chapter 4. The properties of the board and its constituent papers were presented in Table 4-1, Table

4-2 and Table 4-3. The other orthotropic variables needed as the inputs to the FE model were presented and discussed in Chapter 2.5.2.

6.3 Analytical Solutions of CFB Mechanical Performance

The analytical solution for four-point bending of CFB followed as presented as equation (4.2) for bending in CD and equation (4.4) for bending in MD. To calculate the bending stiffness of the crushed samples, the pitch, P, and height of the flute, h_c, were changed in equation (4.2), (4.3) and (4.4) based on the values summarised in Table 6-1.

The empirical solution for the ECT of the CFB was presented in equation (4.11) where the compressive stress in CD and the take-up factor were used as the inputs to the equation. Unlike the bending stiffness equations, the ECT empirical solution suggests that ECT is independent of the flute height, h_c. Hence, it was not possible to use the empirical solution to determine the ECT of the crushed CFB (or that the predicted ECT would be the same for all levels of crush).

6.4 Finite Element Model

6.4.1 Geometry Characterisation

Three quasi-static and implicit FE models were used for this study which consisted of two micro-geometry models defined by a real flute geometry an idealized flute geometry, and an equivalent shell model that represents the flute as a homogenous material. The differences between each model are summarised in Table 6-2.

Table 6-2: Summary of the differences between each FE model used in this study.

	Real Geometry	**Idealized Geometry**	**Equivalent Shell**
Flute Geometry	Geometry extracted from an actual flute using image analysis technique	Geometry defined by sinusoidal wave equation	Use of equivalent shell layer calculated from the properties of the flute structure
Four-point bending	64,000 – 66,000 mesh elements	60,000 – 63,000 mesh elements	25,307 mesh elements
ECT	7,500 – 7,800 mesh elements	6,500 – 7,100 mesh elements	1,938 mesh elements

The real geometry of the crushed flute was extracted from the captured images following the flute tracing technique presented in Chapter 3. The pixel coordinates obtained from each image were then transferred to BS Solidworks 2015 (Dassault Systèmes) to generate the CAD model, and the liners and anvils were added before transferring it to Workbench 17.2 (Ansys Inc.) to simulate the four-point bending and ECT test.

For the idealized geometry, even though Urbanik (2001) reported that the arc-and-tangent curve is more accurate than sinusoidal curve in representing the flute, it was not possible to generate a curve using the reported equation as there is a limit to how much the pitch can be change for a given take-up factor. To overcome this limitation, a sine geometry was used which closely resembles the arc-and-tangent curve and has the advantage that it does not require any take-up factor input. The drawback of using the sine-geometry was that it did not account for the correct take-up factor of the actual crushed flute as shown in Figure 6-1. The higher take-up factor seen in real geometry could mean that it can be stronger due to more amount of paper in the flute compared to idealized geometry. The sine geometry of the flute of the crushed model was characterised by the following equation in BS Solidworks 2015 (Dassault Systèmes):

$$y = \frac{h_c}{2} \sin\left(\frac{2\pi x}{P}\right) \tag{6.1}$$

where the values of h_c (height) and P (pitch) were presented in Table 6-1.

The liners and the anvils were then added, and the CAD geometry was transferred to Workbench 17.2 (Ansys Inc.) to carry out the simulations of four-point bending and ECT tests.

The flute geometries of different levels of pre-crushed CFB for both real and idealized geometries are shown in Figure 6-1.

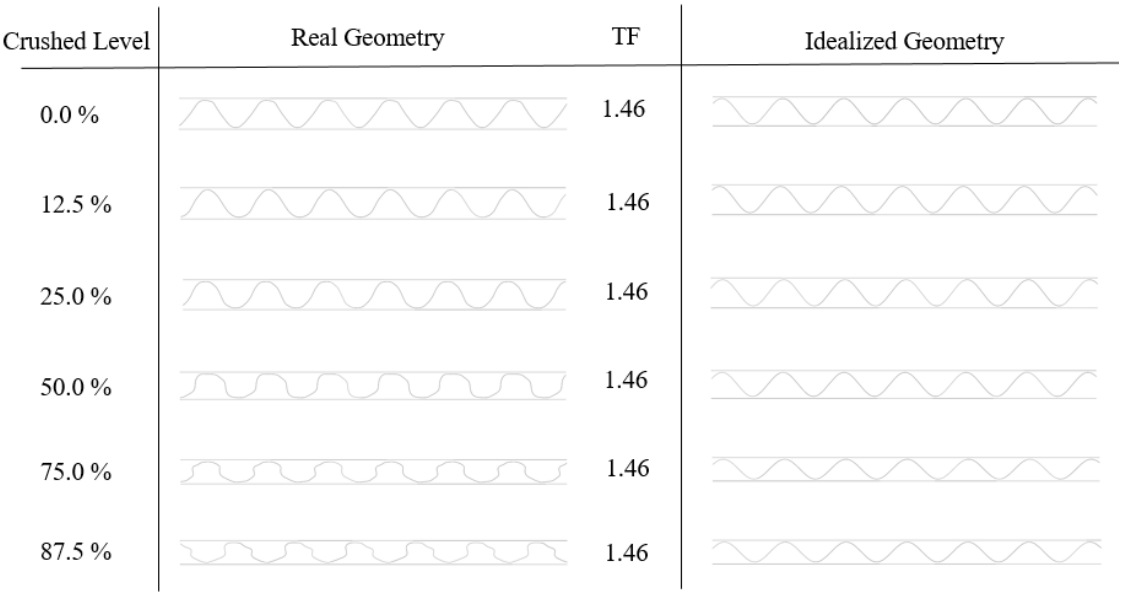

Figure 6-1: The flute geometry of C-flute CFB at different levels of crushing obtained from the using the real geometries through image analysis and from using idealized geometries through sinusoidal wave equation. The TF stands for take-up factor of the board in the crushed level.

To simplify the micro geometry model, an equivalent model was used where the flute was modelled as a shell layer with some of the orthotropic variables of the flute layer converted to account for the structure of the flute. This approach can save significant computational time compared to micro geometry models. The calculation for the equivalent shell properties of the flute is presented in Appendix D and the crush level varied by the height of the flute, h_c, and height of the board, h. (This model was developed by the author's co-supervisor, Dr Celia Kueh and was used by the author in obtaining the results used in this chapter). The outer and inner liners used the same properties as presented in Table 4-2 and Table 4-3. A shell layer with a dimension of 260 mm x 50.8 mm was created including four anvils to simulate the four-point bending test. For the ECT, a shell layer of 38.1 mm x 50.8 mm was created. The shell consisted of three layers; outer liner, flute paper and inner liner which are represented as only one layer in the figure. The thickness of the outer and inner liners remained constant for all levels of crushing while the thickness of flute varied based on the flute height presented in Table 6-1.

6.4.2 Model Setup

For the four-point bending model setup, the model followed the methodology reported in Chapter 4.2.4. The flute and the liners were connected as being perfectly bonded in both micro-geometry models while the contact between the anvils and the board were modelled as frictionless contacts in all the FE models. The large deformation setting was turned on to account for the geometric non-linearities in all models. Figure 6-2 shows the illustration of four-point bending and ECT test setups drawn in BS Solidworks 2015 (Dassault Systèmes).

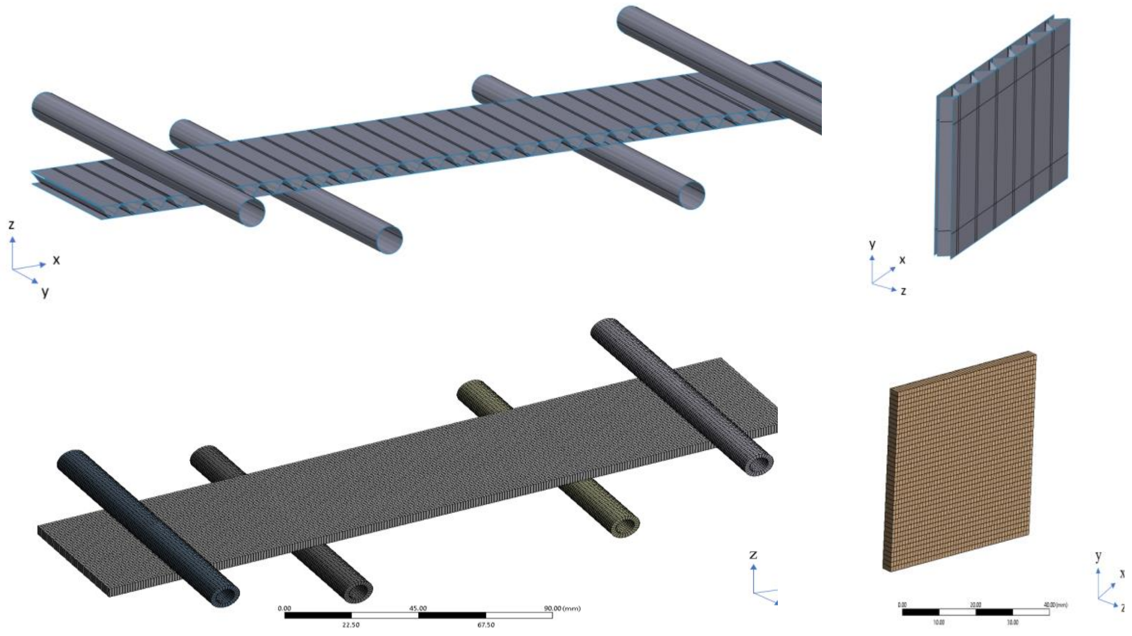

Figure 6-2: The CAD geometry of a four-point bending sample on MD (260 mm x50.8 mm) and ECT sample (38.1 mm x 50.8 mm) of a micro-geometry model and an equivalent model drawn in BS Solidworks 2015 (Dassault Systèmes).

The round edges of the top anvils were displaced downwards by 15 mm in the z-direction and the displacements in the x and y direction was set as fixed. The round edges of the bottom anvil were set as fixed displacement in x, y and z directions. A nodal vertex on the centre of the inner liner (centre of the layer in equivalent model) was set to be fixed along the y-direction to prevent rigid body motion while the direction of x and z were left free. A quadrilateral mesh element of 1 mm was applied, and the number of mesh elements generated in each model were presented in Table 6-2. Further refinement of the meshes used did not lead to any change to the bending stiffness prediction.

The setup of the ECT also followed the same methodology as presented in Chapter 4.2.4 where to simulate the wax region (as per TAPPI T 811 standard), two regions 6 mm from the top and bottom edges were set as rigid and only allowed to be displaced in the y-direction and rotate around the x-axis. This helped to prevent failure from occurring in the top and bottom regions. The top edges were displaced by 1 mm in the negative y-direction and directions x and z were left free. The bottom edges were fixed in x, y and z directions. A quadrilateral mesh element of 1 mm was used, and the number of mesh elements generated in each model were presented in Table 6-2. Further refinement of the meshes used did not lead to any change to the results. As in Chapter 4, failure was determined by examining the contour plots of the Tsai-Wu failure criterion when the scale of the failed regions (values larger than 1) on the liners reached the length of the pitch

A stabilisation damping coefficient of $2x10^{-5}$ was applied in both micro-geometry models to aid the convergence of the simulation, however it was not needed in the equivalent model as it had no convergence difficulties. It is worth mentioning that an inclusion of the stabilisation damping coefficient of $2x10^{-5}$ did not lead to changes in the equivalent model results.

6.5 Results & Discussion

6.5.1 *Bending Stiffness*

Figure 6-3a shows the raw CFB bending stiffness in CD predictions compared with the experimental data reported in Chapter 5. Figure 6-3b shows these results that have been normalised against the bending stiffness of the uncrushed samples (0%) for each model/experiment. The predictions for all models match reasonably well with the experimental results where the bending stiffness decreased as the crushing level increased.

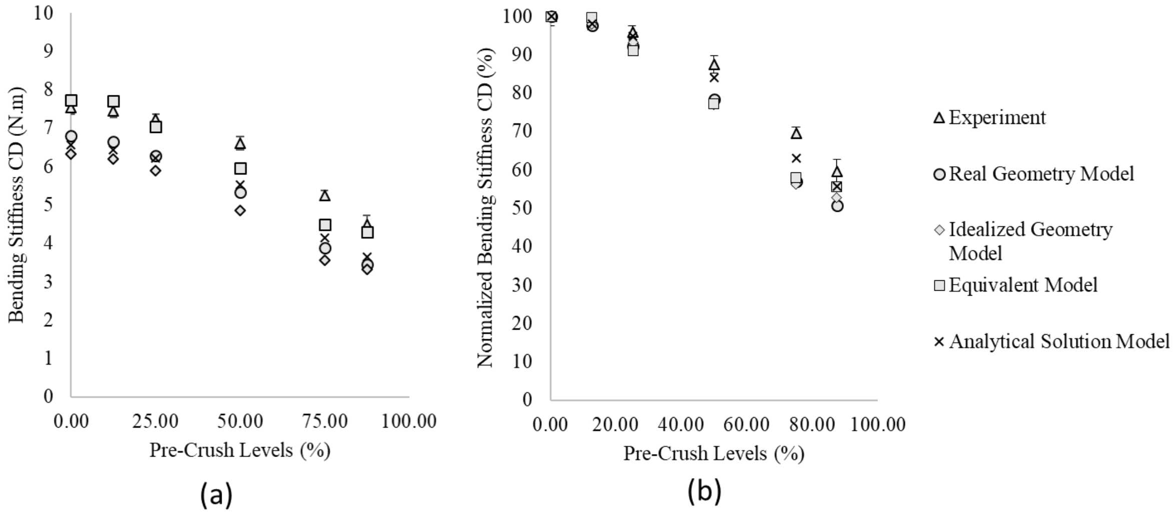

Figure 6-3: Bending stiffness in CD obtained from the experiment and different models.

Based on Figure 6-3(a), the real geometry, idealized geometry and analytical solution under predicted the bending stiffness of CFB in CD when compared to the experimental results (by up to 32%). As discussed in Chapter 4.3.1, it is likely that the under prediction came from not considering the glue that adheres the liners and flute together. Approximation of some material constants (such as presented in Section 2.5.2) might also contribute to the differences between experiment and model predictions. Aside from the under prediction at 50% and 75% pre-crushed levels, the equivalent model showed an accurate prediction compared to the experimental results.

Based on Figure 6-3(b), when normalised to account for the effect of the adhesive layers and any underestimation of material properties, all models showed a similar response in trend with increasing crushed level. This shows that the inclusion of the real geometry of a crushed flute may not be necessary to capture the bending performance in CD and the paper properties and calliper define the bending performance of CFB.

Figure 6-4 shows the CFB bending stiffness results and the normalized bending stiffness (against the uncrushed samples 0%) in MD from the experiment and different models. Similar to the bending on CD, the bending stiffness on MD decreased as the level of pre-crushing increased.

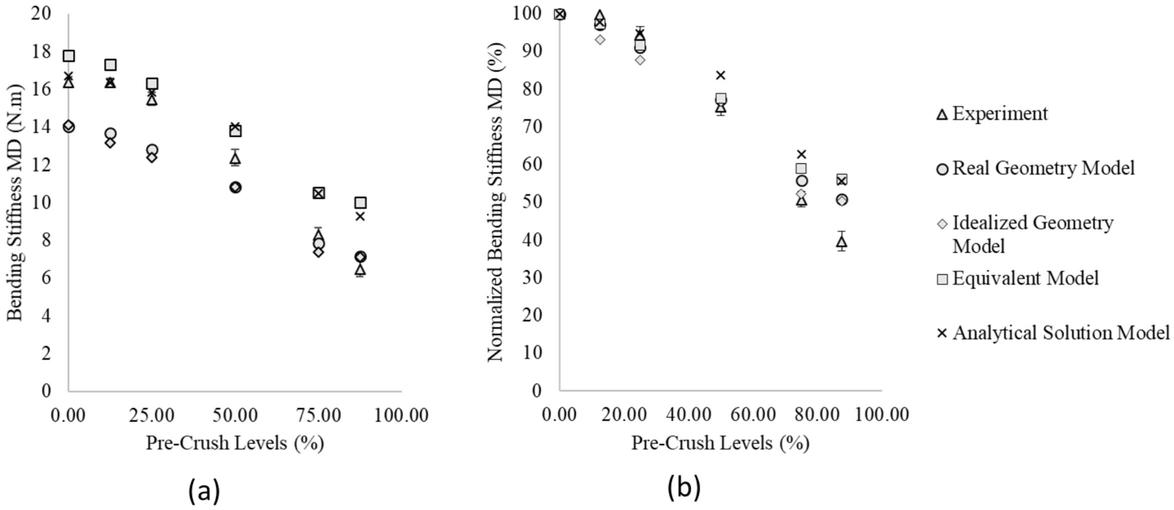

Figure 6-4: Bending stiffness in MD obtained from the experiment and different models of CFB.

Between pre-crushed levels of 0% and 25%, the analytical model showed accurate agreement with the experiment (within 3.5%), the equivalent model over predicted the experimental results (by up to 9%), and both real and idealized geometry models under predicted the bending stiffness on MD (by up to 20%) which can be associated to the addition of stiffness from the glue that was not considered in the model.

From 50% pre-crushed levels onwards, the bending stiffness from the experiment showed a larger drop compared to all models as shown in Figure 6-4(b). This may be associated with other damage caused by crushing the samples such as delamination of the flute that was not considered in the models. The delamination of the flute may weaken the whole board by decoupling the connection between the liners and result in significant loss of bending stiffness.

On the dropping trend across the pre-crushed level, all models showed a similar trend as seen in Figure 6-4(a). This shows that the bending performance in MD was not governed by the geometry of a crushed flute but governed by liner properties and the calliper of the CFB.

6.5.2 Edge Crush Test (ECT)

Figure 6-5 shows the ECT results and the ECT results normalised against the uncrushed CFB samples (0%) from the experiment and as predicted by the models. It was observed that the ECT force decreased as the crush level increased.

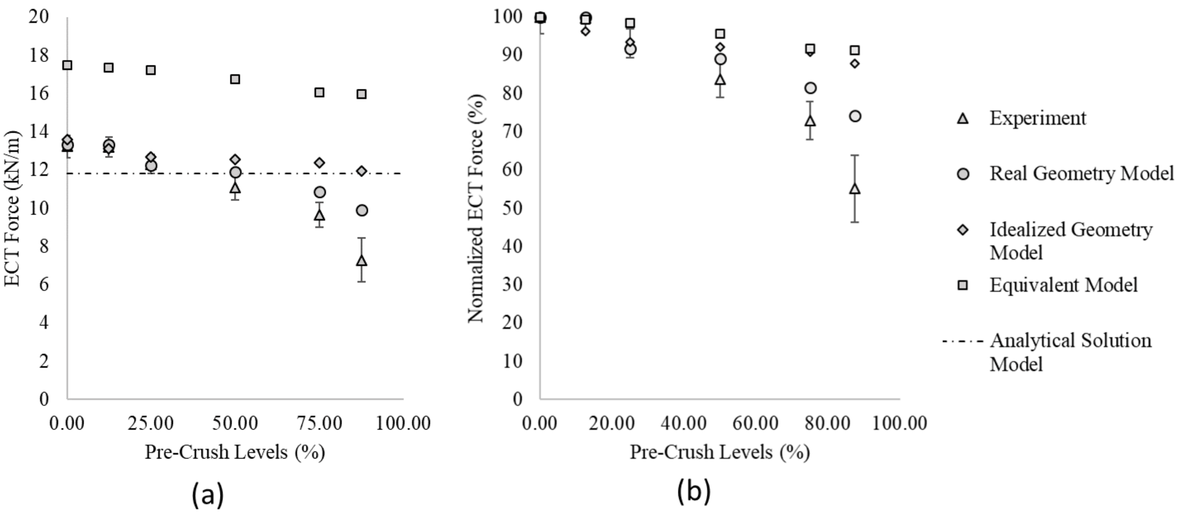

Figure 6-5: ECT force of the CFB obtained from the experiment and different FE models.

From Figure 6-5(a), it can be seen that the real and idealized geometry models showed closer agreement to the experiment as opposed to the equivalent model and analytical solution. The analytical solution was limited, allowing only prediction of the undamaged ECT sample (0%) as it did not consider the calliper variable in equation (4.11). The equivalent model showed the biggest difference at 0% pre-crushed level and consistently over predicted the experimental results between 32% - 119% at all crush levels which might be explained by its difficulties to predict buckle as a solid core in the edge compression model.

From Figure 6-5(b), all models showed a dropping trend in the ECT force between crush levels of 0% and 25% except for the analytical solution model. It was observed that between these levels, the real and idealized geometry models showed good accuracy compared to the experiment. However, from a crush level of 50% onwards, the real geometry model followed the experimental ECT force more closely than the other models. This shows that the use of the actual flute profile in CFB samples can provide more sensitive ECT force predictions. Nevertheless, the experimental ECT force still shows a larger dropping trend (50% to 87.5%) compared to the real geometry model and this may be due to other damage such as delamination that was not considered in the model (Giampieri et al., 2011).

6.5.3 Microscopic Analysis

Figure 6-6 shows images of the flute structure at different crush levels that were obtained using a BX53 Upright Microscope with XC50 Digital Camera (Olympus Corp.). The images at 0% crush (i.e. uncrushed) level serve as a point of reference to analyse the structure of the flute compared to different crush levels.

Extent of Crushing (%)	**Microscopy Image**	
0 %		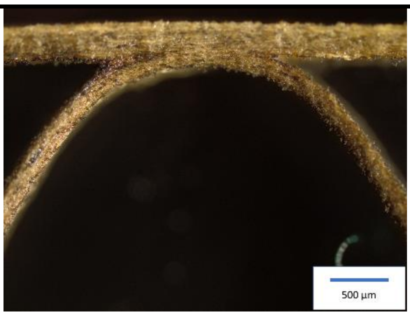
12.5 %	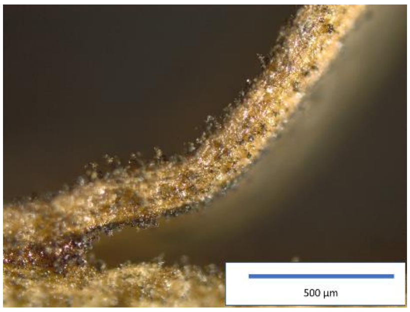	
25 %	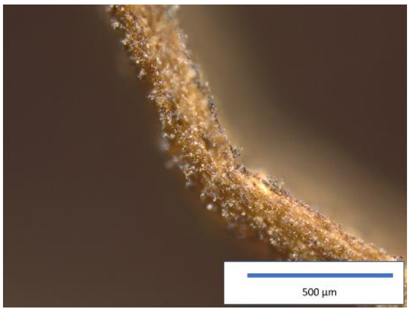	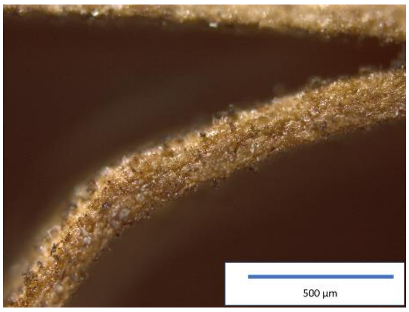
50 %		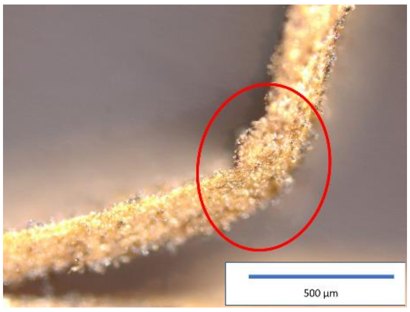
75 %	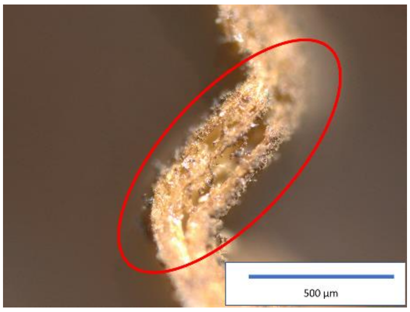	

87.5 %	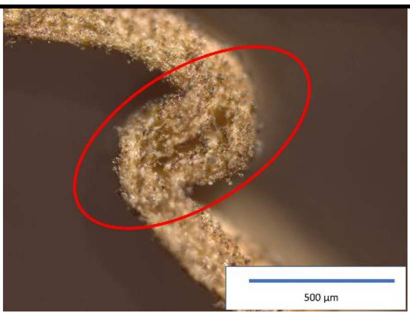	

Figure 6-6: Microscopy analysis of the structure of flute liner at different pre-crushed levels. The regions bounded by the red circles show signs of delamination.

It was observed that the flute buckled at 12.5% and 25% crush levels but there was no evidence of delamination at these stages. The geometry of buckling on the flute was captured by the real geometry model as presented in Figure 6-2. As a consequence, the predictions from the real geometry model were excellent. From crush levels of 50% onwards, signs of delamination were observed. The delamination was shown to propagate from the middle section of the flute liner and has been suggested to be caused by the inter-laminar shear force exerted during the crushing process (Beex & Peerlings, 2009). It is well known that delamination weakens the paper (Beex & Peerlings, 2009; Giampieri et al., 2011; Nygårds et al., 2009). Since this damage was not considered in any of the models, this may be the reason why from 50% pre-crushed levels onwards, the dropping trends in the experimental bending stiffness in MD and experimental ECT force were larger than predicted by all the models.

6.5.4 *Model Evaluation*

Based on the results, it can be seen that all the models can predict the mechanical performance of CFB with reasonable accuracy. Table 6-3 shows the computational time required to run each FE simulation. The equivalent model had the lowest computational solving time while the real and idealized geometry models had similar solution times.

Table 6-3: Computation time to simulate the FE model response of CFB under four-point bending loading and ECT test using a computer processor of Intel (R) Core (TM) i7-6700 CPU @ 3.40GHz and 16 gigabytes of random-access memory (RAM). Note that analytical solution model is not presented here as it does not require computation power to solve the equation.

	Computational Solving Time (min)		
FE Model	**Bending CD**	**Bending MD**	**ECT**
Real Geometry	27 – 40	24 – 40	3 – 5
Idealized Geometry	14 – 30	24 – 35	3 – 3.5
Equivalent	4 – 6	4 – 6	0.3 – 0.5

The real geometry model showed a good prediction trend for the bending performance in CD. It also showed a reasonable trend for the bending performance in MD and ECT performance but due to not considering the delamination on the flute liner, the trend started to skew beyond the 50% crush level. As opposed to other models, the real geometry model showed the best sensitivity in predicting the ECT performance on crushed boards.

The idealized geometry model behaved similarly to the real geometry model in both bending in CD and MD performance. This suggested that the effect of flute geometry and the lower take-up factor seen in Figure 6-1 were not a major factor in predicting the bending stiffness of CFB. In predicting the ECT performance, there was a good accuracy for the 0% and 25% crush levels, but it was not as sensitive as the real geometry model when applied beyond 50% crush. While not achieving the right take-up factor could be a reason, it seems unlikely as having less mass of fluting medium paper compared to the actual geometry should mean that the idealized geometry model is weaker but the results showed that it was the other way around. Hence, the lack of sensitivity might be more affected due to not considering the actual geometry.

The equivalent model captured the bending performance reasonably accurately and proved that the thickness of the board was more crucial than the flute geometry in affecting the bending performance. The equivalent model over predicted the experimental results for ECT and showed a similar dropping trend as the idealized geometry model as the level of crush increased. However, it was not as sensitive as the real geometry model. An advantage of the equivalent model was that the computational time reduced significantly compared to the micro geometry models.

The analytical solution captured the bending performance reasonably well and further justifies the importance of board thickness over the flute geometry with respect to bending performance. However, it over predicted the ECT force of uncrushed sample and there is currently no relation that can be used to predict the ECT performance of a crushed CFB since the analytical solution for ECT is more dependent on the compression properties of the paper components (Dimitrov, 2010). It was also found to be the quickest way to predict the strength performance of CFB since it did not require any computation solving time.

6.6 Conclusion

In this chapter it was found that to predict the bending performance of CFB, all models showed a similar trend as the extent of crushing on the board increased which proved that the bending stiffness was more sensitive towards the calliper of the CFB rather than the flute geometry. On predicting the ECT performance, the real geometry model showed the closest match to the experimental results which suggested the importance of flute geometry. Damage to the structure of the flute due to delamination was evident in significantly crushed samples and was not included in any of the models which is likely the reason the models over predicted the mechanical performance of CFB at high crush levels.

The availability of a micro-geometry model based on real flute measurements can allow further investigation on how other forms of damage influence CFB behaviour. For example, it could be used to see how localised damage such as local crushing or perforations can affect the overall CFB mechanical performance. Application of the model in this way is the focus of the next chapter.

Reference

Beex, L., & Peerlings, R. (2009). An experimental and computational study of laminated paperboard creasing and folding. International Journal of Solids and Structures, 46(24), 4192-4207.

Dimitrov, K. (2010). Relationship between the ECT-strength of corrugated board and the compression strength of liner and fluting medium papers (Doctoral dissertation). University of Pretoria, Pretoria, South Africa.

Giampieri, A., Perego, U., & Borsari, R. (2011). A constitutive model for the mechanical response of the folding of creased paperboard. International Journal of Solids and Structures, 48(16), 2275-2287.

Nygårds, M., Just, M., & Tryding, J. (2009). Experimental and numerical studies of creasing of paperboard. International Journal of Solids and Structures, 46(11), 2493-2505.

Urbanik, T. (2001). Effect of corrugated flute shape on fibreboard edgewise crush strength and bending stiffness. Journal of Pulp and Paper Science, 27(10), 330-335.

Chapter 7.

Perforated Corrugated Fibreboard – Localised damage

Preface

In this chapter, the performance of perforated CFB was investigated. The approach used in this chapter was to replicate commercially perforated samples in a lab and to validate them through the use of the flute morphology technique in developed in Chapter 3. The mechanical performance was evaluated and used to extend the real flute geometry FE model in developed in Chapter 4 to include perforations.

7.1 Introduction

Perforation is defined as the formation of a series of holes that are made through piercing the sheet. In CFB, perforated lines are widely used to decrease the properties of the board along the lines so that it is easier to tear them apart (Hermansson, 1999). This is especially useful for shelf-ready packaging in the market where retailers can directly place the box with the products inside on the shelf and tear off some of the box to display the contents. In doing this, retailers can avoid spending time to organise the products on the shelf. In addition, perforated lines along with ventilation holes are also well known in fruit and vegetable packaging as they can provide air ventilation and temperature balance which increases the shelf life of the products (Jinkarn et al., 2006).

While the addition of perforations to CFB helps to add more packaging features, it comes at the expense of losing some of its compressive strength performance (Neidoni et al., 2006). The perforated holes may be designed to be large to easily tear them but will be weaker in terms of its stacking strength. Hence, an optimal balance is important to get the best performance of perforated CFB packaging designs. Currently, there is little information in the published literature in this area.

To be able to conduct research of perforated CFB, it is important to have a repeatable lab-scale way of producing the perforated samples as industrially perforated CFB are prone to variability due to handling, stacking, printing and wear and tear of the perforation tool. In addition, obtaining commercial samples with perforations at specific angles (relative to the flute direction) is difficult. Several parameters need to be accounted for to characterise perforation. In this study, the focus was on the punch depth, surface topography analysis and flute morphology analysis (developed in Chapter 3) around the perforation area. In commercial perforation practice, the perforation rule (blade) is punched through the CFB in a flatbed or more commonly rotary die, there is significant compression applied to the CFB locally during the hole cutting. It is hypothesised that this local damage may influence the mechanical properties of the material, in addition to the formation of the perforation holes themselves. Since laser cutting can produced a consistent lab perforated samples without this type of damage, this study also included laser cut perforation samples to be able to compare how the indentation caused by the mechanically perforated samples affect them.

The ability to rapidly evaluate the impact of perforation on overall CFB or packaging performance would have wide application. For example, the location and shape of perforated lines could be optimised to minimise the impact on box integrity within the constraints imposed by the need to include perforations in the design. This could be achieved by modifying the FE model developed in Chapter 4 to include localised damage. Back in Chapter 2, it was shown that there is currently limited research reported on developing a FE model of CFB with perforation. This chapter also looked at the potential to include perforations and validated it with experimental results for CFB bending.

The course of this chapter was divided into two sections. The first was to investigate ways to replicate industrial perforation in a laboratory using the same mechanical tool as used in the manufacturing plant. B-flute CFB was used in this study where four different sample groups were perforated to different depths and validated by comparing with industrially perforated samples through surface topography analysis and the use of Skeleton analysis as developed in Chapter 3 to quantify the flute morphology. From here, the closest matched sample groups were identified and selected to analyse the apparent bending stiffnesses which were compared with an undamaged and laser perforated samples.

The second part presents the extension of FE model developed in Chapter 4 with addition of perforation in assessing apparent bending stiffness. Since the resources to determine the material properties of the B-flute CFB were not available, this section used C-flute CFB and laser perforated the samples at different orientations similar to the reported work in Chapter 4 and using the same base material. The FE model and experiment were then compared in terms of the apparent bending stiffness, maximum bending force and the failure plot.

7.2 B-Flute CFB: Replicating Industrial Perforation in Laboratory

B-flute CFB was supplied by Oji Fibre Solutions in the form of manufactured boxes, with a pitch, height and take-up factor of 6.5 mm, 2.5 mm and 1.35 respectively. The largest panels of the boxes were cut using an Epilog Fusion M2 laser cutter into samples of 260 mm x 25.4 mm along the CD direction. It is worth mentioning that the sample widths for bending testing were shorter than the C-flute CFB as reported in Chapter 4, 5 and 6 (260 x 50.8 mm) due to the limited size of the boxes the samples were prepared from, however they were still in the acceptable range of TAPPI T-811 CM-09 for conducting the four-point bending test.

7.2.1 Identifying Laboratory Perforated Punched Depth

The goal of this experiment was to identify the closest matched lab-designed perforated samples to the industrial perforated samples. Figure 7-1 shows the supplied B-flute CFB where the samples were cut as illustrated by the dotted line and industrial perforated samples (red circle) were cut from the box.

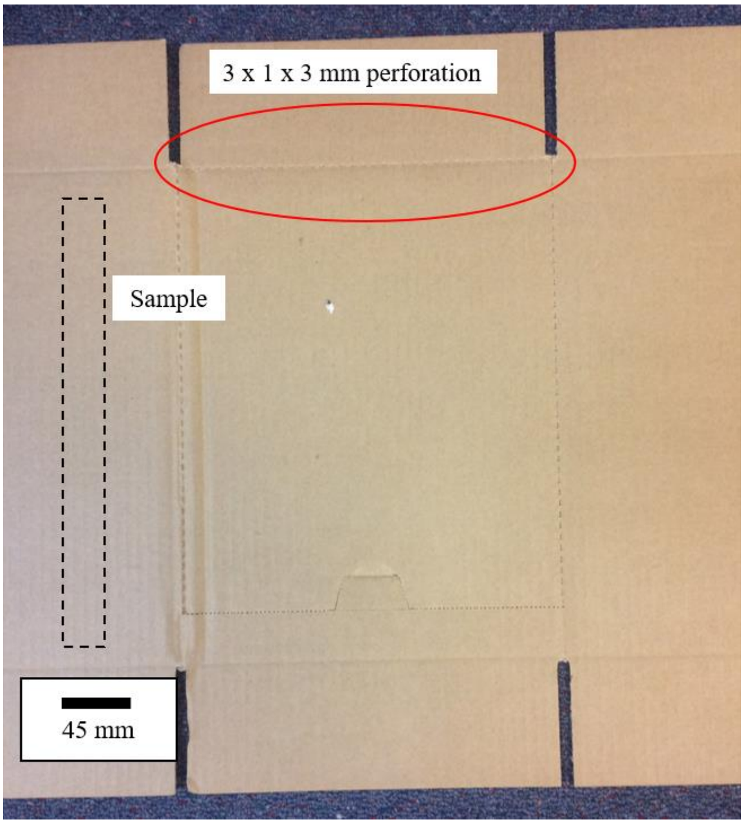

Figure 7-1: B-flute CFB samples that were supplied for this research.

The mechanical perforation rule of 3 x 1 x 3 mm was supplied by Oji Fibre Solutions along with a polyurethane foam sample that is used to generate spring-back force when punching the perforated tool into the CFB and release it after perforation (see Figure 7-2). The overhang vertical distance between the PU foam and perforation tool was about 1.5 mm as shown in Figure 7-2. The flat-bed perforation was carried out using a texture analyser TA.XT at a speed of 40 mm/sec on the inner liner of CFB samples. This speed was chosen since it is the maximum allowable speed of that equipment, however, the speed of perforation of CFB in a manufacturing plant is faster than this. In addition, the supplied industrial perforated board samples were perforated using a rotary die which may have a different impact to a flat-bed perforation. A 5 mm thick polyethylene base was used as an anvil to punch through the CFB into.

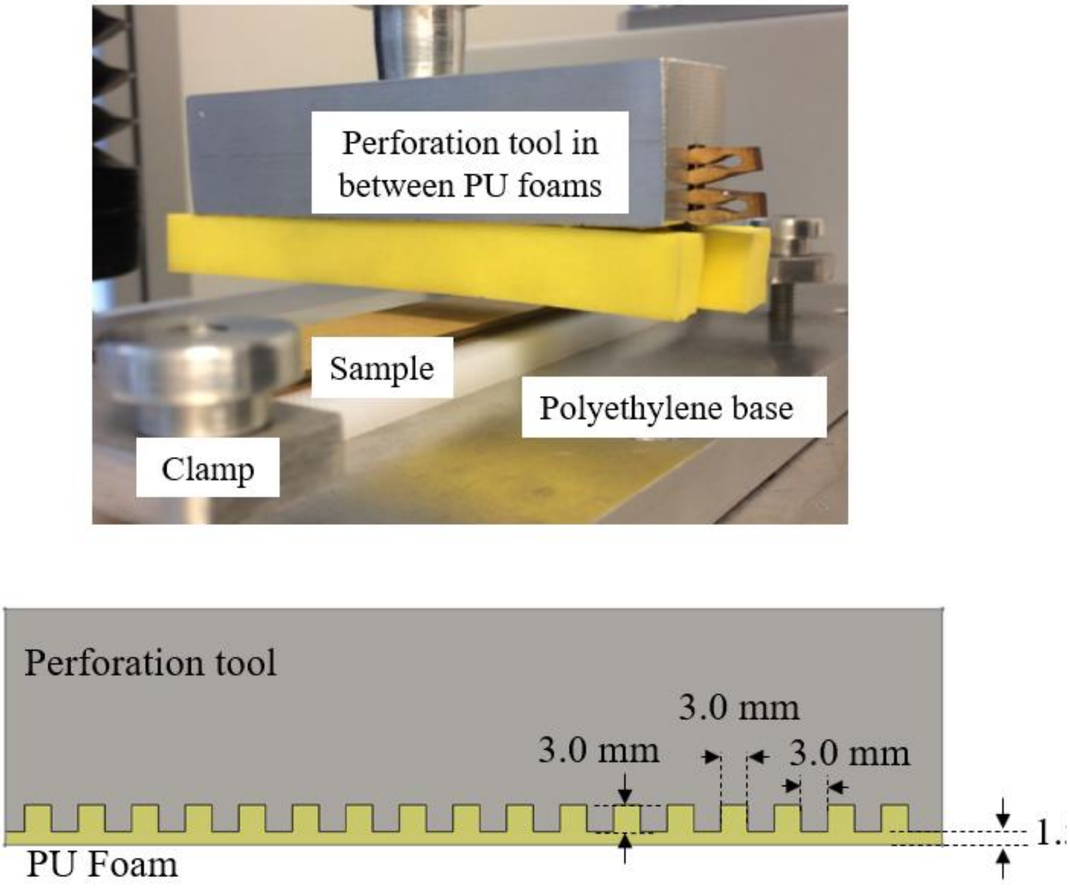

Figure 7-2: The mechanical perforation tool supplied by Oji Fibre Solution and used to perforate B-flute CFB in this study. The polyurethane (PU) foam was also supplied from the same supplier. In the bottom figure, the foam on the other side was not included to be able to see the blade.

Preliminary testing was done by perforating the CFB samples between a depth of 4.0 mm to 6.0 mm at increments of 0.5 mm. The depths were measured from when the foam contacts the samples, which means an offset of 1.5 mm before the perforation tool punched the sample as seen in Figure 7-2. The results found that 4.5 mm was the minimum perforated depth as at 4.0 mm, the perforation tool did not manage to punch through the CFB samples. Hence, the analysis was only done for samples perforated at a depth between 4.5 mm to 6.0 mm with increments of 0.5 mm and three replicates were done for each depth.

The surface topography of the perforated region was then analysed using a fringe projector (PRIMOS Lite) that captures an area of 20 x 13 mm on the sample. Figure 7-3 shows the contour plot of the perforated region while Figure 7-4 shows the indentation depth of each case.

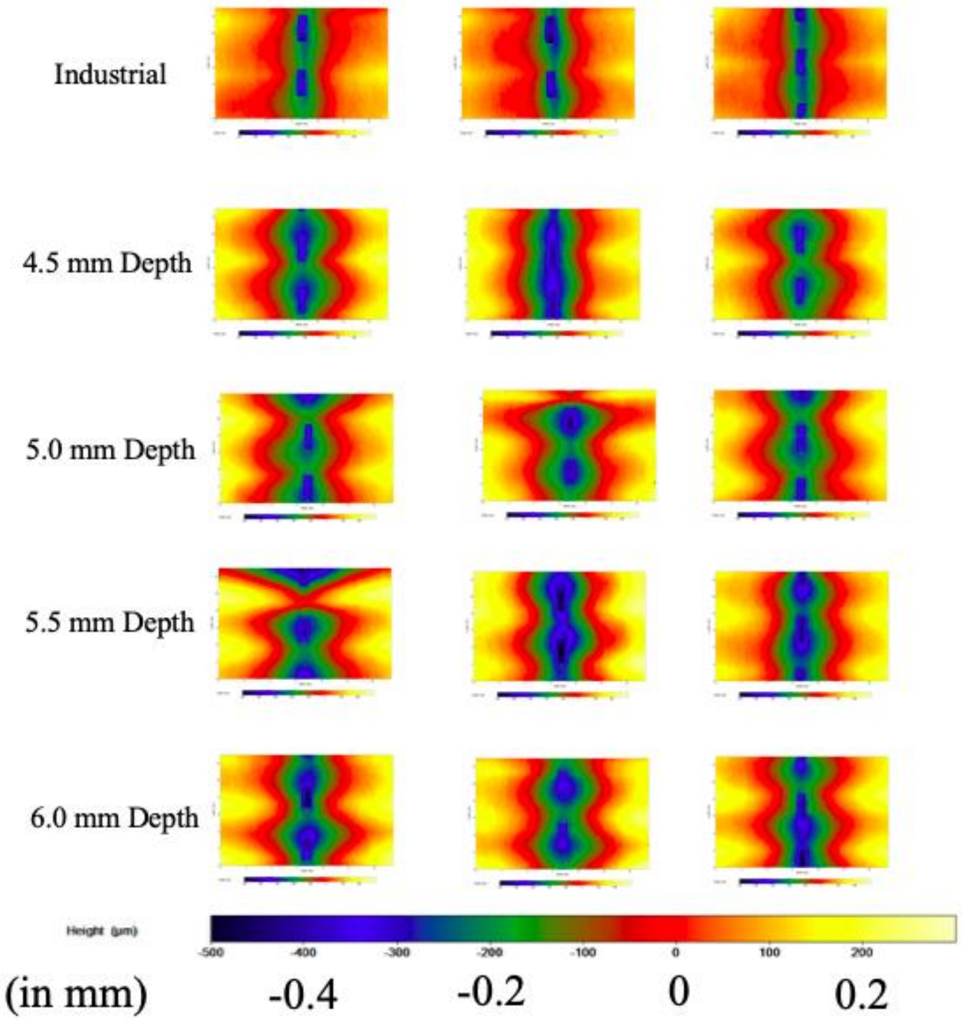

Figure 7-3: Surface topography on perforated region of several CFB samples where each group consist of three replicates. The height and width of each profile is 13 and 20 mm respectively.

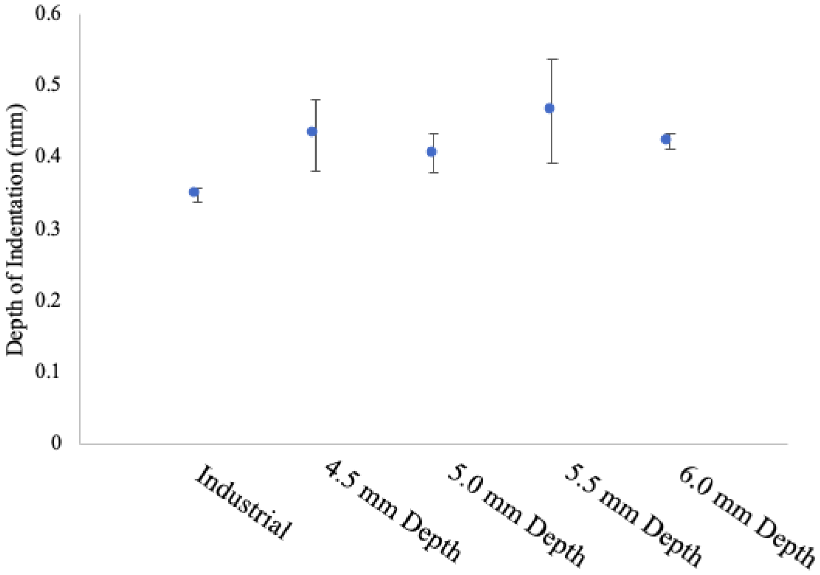

Figure 7-4: Depth of indentation across the perforated line measured from the surface topography profile using the Fringe projector. Error bars are +/- 1 SD (n=3).

It was observed in Figure 7-3 that the lab perforated samples had deeper and sharper indentation near the perforations compared to the industrial perforated samples. This was supported by the depth of indentation shown in Figure 7-4 where the industrial perforated group had the lowest depth of indentation as opposed to other groups. It possible that this was due to different speed and mode (flat vs rotary) of perforation between the lab and industrial samples.

Even though there were differences observed between the lab perforated and industrial perforated samples, the biggest difference of the indentation depth on average was only about 0.11 mm. As this accounted for about 4% of the total board calliper, it was considered as an acceptable tolerance to proceed with the lab perforated samples. It is worth mentioning that samples perforated at 6.0 mm depth had larger perforation holes than the industrial perforated samples.

To investigate further, the morphology of the flute along the perforated line was investigated by cutting thin strips of 1 mm (three replicates from each sample) and the

Skeleton analysis as developed in Chapter 3 was performed. Figure 7-5 shows the similarity factor of the flute morphology relative to the undamaged group that were obtained using the Skeleton analysis.

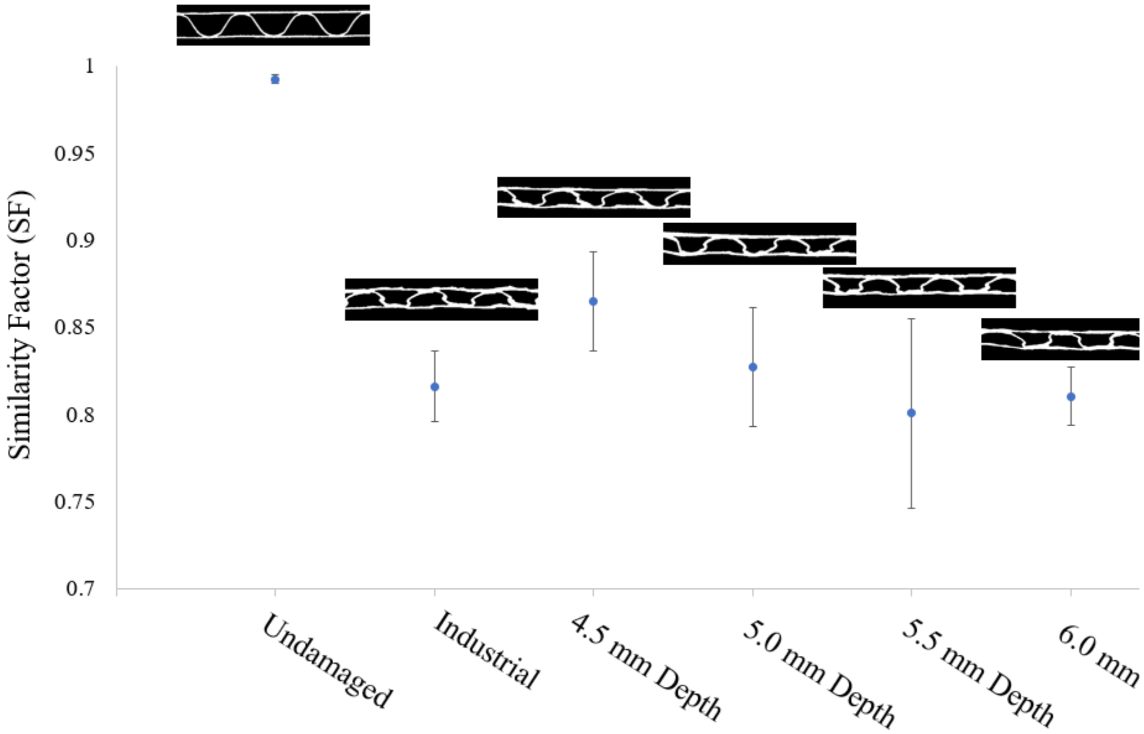

Figure 7-5: The similarity factor (SF) of flute morphology of different perforated CFB samples relative to undamaged CFB including an example of the image of each sample. Error bars are +/- 1 SD (n=9, 3 replicates of 3 samples).

It was observed that the SF dropped significantly between the undamaged and perforated samples. Between all the perforated samples, a one-way ANOVA was conducted and showed that there was no significant difference between the SF, $F(4,10) = 1.10$, $p = 0.41$. This proved that the morphology of the flute was not affected significantly and hence, lab perforated samples matched sufficiently well with industrial perforated samples.

7.2.2 Bending Performance of Perforated B-Flute CFB

The apparent bending performance of perforated B-flute CFB was carried out through performing four-point bending testing in accordance to TAPPI T-811 CM-09. The samples were 260 x 25.4 mm and perforated perpendicular to the bend direction at three different depth; 4.5 mm, 5.0 mm and 5.5 mm with each consisted of ten samples each. The 6.0 mm deep samples were omitted as the perforation holes was found to be larger and more aggressive than the industrially perforated samples. Undamaged and laser perforated samples were also included to compare them with the mechanically perforated samples. The laser perforated samples were perforated perpendicular to the bend direction using Epilog Fusion M2 laser cutter with a dimension of 3 x 1 x 3 mm across the width in the centre of the sample. Each sample consisted of ten replicates and the angle of flute orientation was set only along CD direction as the size of the supplied box did not allow for producing samples in MD direction. Industrially perforated sample were not included in this experiment as the size of the supplied box did not allow enough length to be produced based on the required standard sample size (see Figure 7-1). The force and centre deflection data that were obtained from the experiment was calculated into the apparent bending stiffness following the bending stiffness equation (4.1) presented in Chapter 4. The outcomes from the experiment were compared the apparent bending stiffness and maximum bending force of between different samples.

B-Flute Apparent Bending Stiffness

Figure 7-6 presents the apparent bending stiffness of samples of perforated B-flute CFB. Data is presented as mean and standard deviation. The letters denote that for all variables with the same letter, the difference between the means is not statistically significant by one-way ANOVA. If two variables have different letters, they are significantly different.

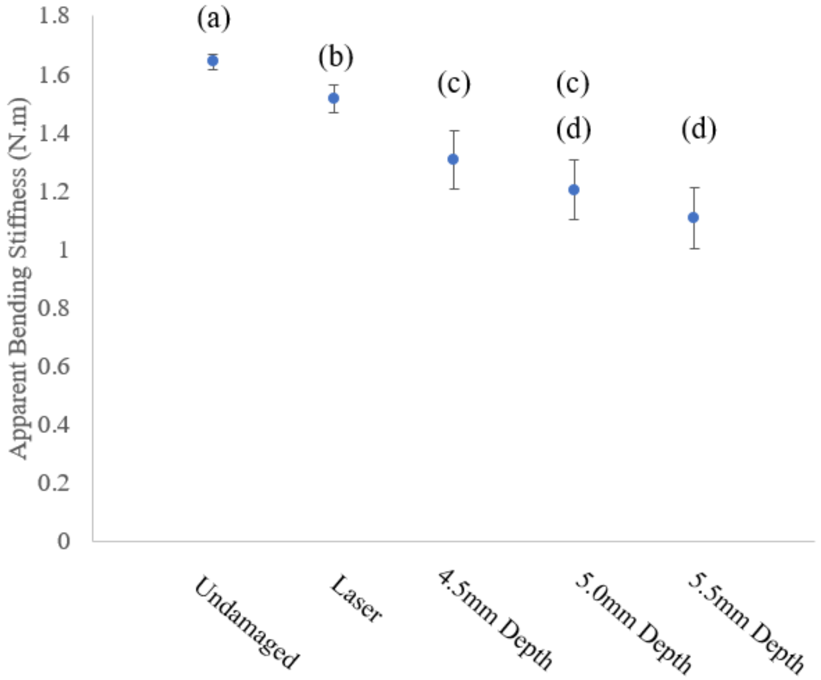

Figure 7-6: The apparent bending stiffness of undamaged CFB and several perforated CFB samples as measured through four-point bending test. The letters refer to the significance between each crushed level based on an Anova and Tukey posthoc analysis. Error bars are +/- 1 SD (n=10). (Refer Appendix E for Tukey post-hoc results)

It was observed that the undamaged group had the highest bending stiffness compared to the apparent stiffness of the other groups. By laser perforating the CFB, the apparent bending stiffness dropped significantly ($p < 0.05$) compared to undamaged group.

The laser perforated group was found to perform better in terms of the bending performance as opposed to mechanically perforated groups ($p < 0.05$). This was due to the indentation caused from perforating the samples mechanically whereas there was no indentation is formed using the laser cutter. The indentation tends to weaken the CFB further, hence, reducing the apparent bending stiffness.

Between the mechanically perforated groups, there was no statistical evidence found say there are differences between the 4.5 mm and 5.0 mm depth, and 5.0 mm and 5.5 mm depth ($p > 0.05$). There was however, a statistically significant drop in the apparent bending stiffness between samples of 4.5 mm and 5.5 mm depth.

B-Flute Maximum Bending Force

Figure 7-7 presents the maximum bending force from the different perforated samples of B-flute CFB. Data is presented as mean and standard deviation. For all variables with the same letter, the difference between the means is not statistically significant whereas it is statistically significant when two variables have different letters.

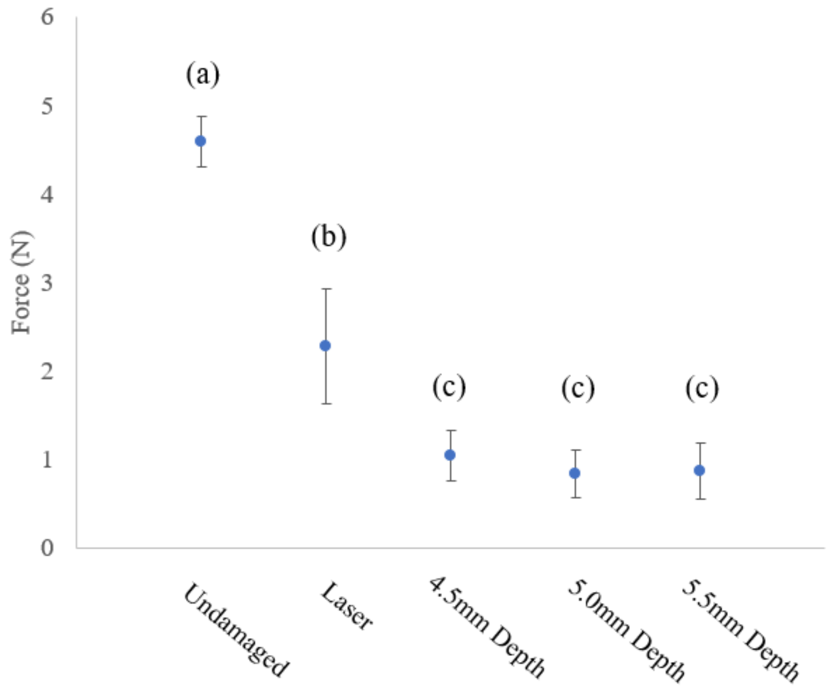

Figure 7-7: Maximum bending force of undamaged CFB and several perforated CFB samples as measured through four-point bending test. The letters refer to the significance between each crushed level based on an Anova and Tukey posthoc analysis. Error bars are +/- 1 SD (n=10). (Refer Appendix E for Tukey post-hoc results)

A one-way ANOVA revealed that at least one pair had a statistically significant difference between each other ($p < 0.05$). The undamaged group had the highest maximum bending force compared to other perforated samples. The laser perforated group was found to have significantly higher maximum bending force compared to mechanically perforated groups ($p < 0.05$). Between the mechanically perforated groups, there was no statistically significant difference found ($p > 0.05$).

Interestingly, the laser perforated group had the largest standard deviation as opposed to other samples. Figure 7-8 presents the force-deflection curve of all laser perforated samples where it was observed that there were two consistently high and low maximum bending forces observed from the ten samples. Figure 7-9 shows the perforated region on the bottom liner of each sample that were segregated according to the high and low of the maximum bending force. The perpendicular lines to the perforated line are the peak of the flute and the view is on the bottom liner of the samples (compressive side during bending).

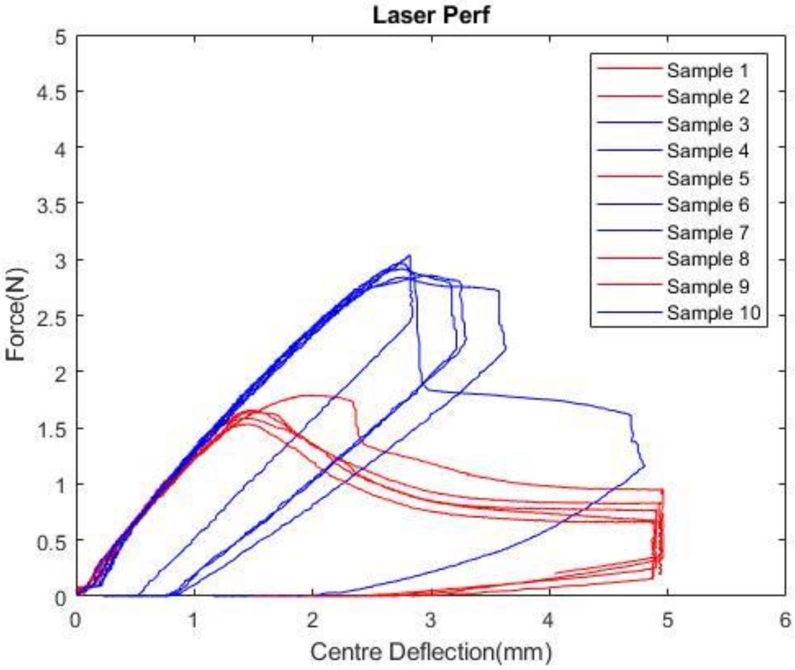

Figure 7-8: Force-deflection curve of laser perforated CFB samples. (Blue colour is the samples that had perforation holes in between the flute peaks on the bottom liner and red line is the samples that had perforation on the flute peaks on the bottom liner, refer Figure 7-9)

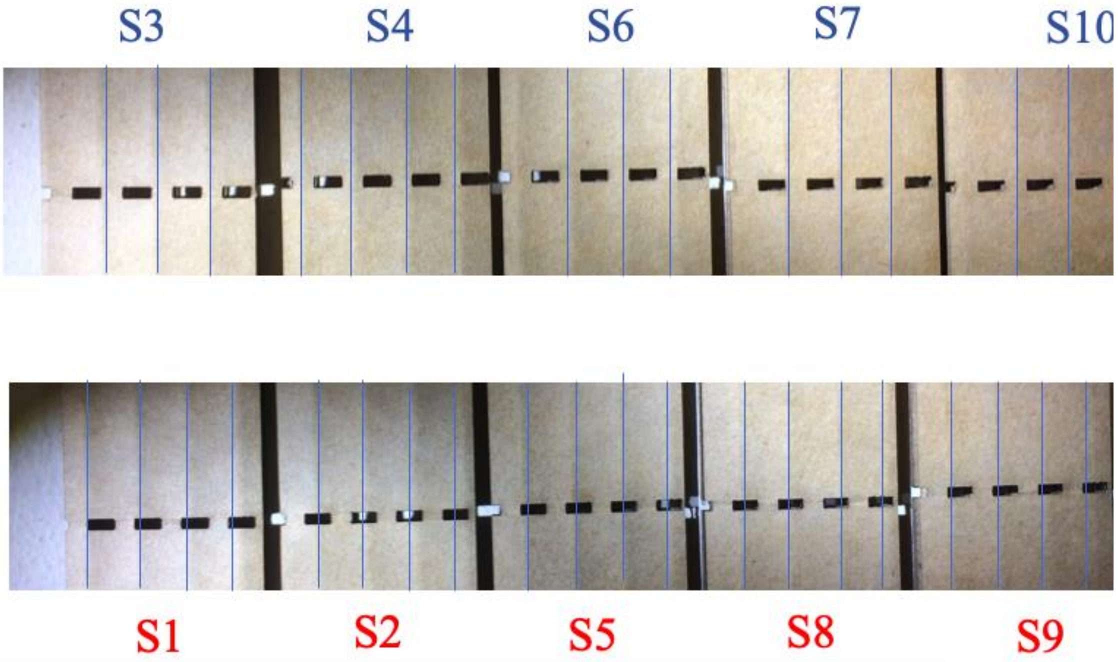

Figure 7-9: Illustration of the perforation region on laser perforated CFB samples where the top row shows perforation in between the flute peaks on the bottom liner while bottom row shows perforation on the flute peaks on the bottom liner.

Figure 7-9 revealed that the difference between both groups were due to the positions of the perforated holes across the width of the samples. For samples that had higher maximum bending force, the perforated holes lay in between the peaks on the bottom liner whereas the maximum bending force was lower when the perforated holes lay on the peaks on the bottom liner. During bending, the bottom liner experienced compressive stress while the top liner experienced tensile stress. When the peaks of the flute on the bottom liner were cut, the glued region between the bottom liner and flute were removed which reduced its ability to resist compressive stress, hence, resulting in lower maximum bending force.

After this behaviour were observed, all the mechanically perforated samples were also segregated into groups of perforation holes that lay on the peaks and non-peaks of the bottom liner. Force-deflection curves for all three mechanically perforated samples are presented in Figure 7-10.

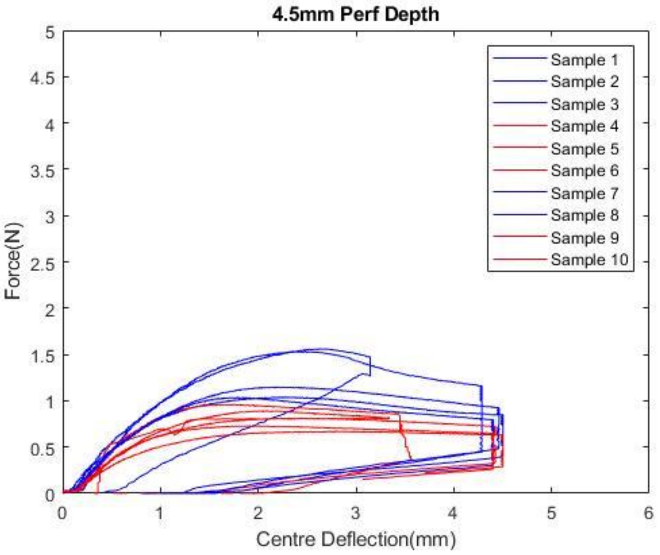
4.5mm Perf Depth
Force(N)
Centre Deflection(mm)
0
0.5
1
1.5
2
2.5
3
3.5
4
4.5
5
0
1
2
3
4
5
6
Sample 1
Sample 2
Sample 3
Sample 4
Sample 5
Sample 6
Sample 7
Sample 8
Sample 9
Sample 10

(a)

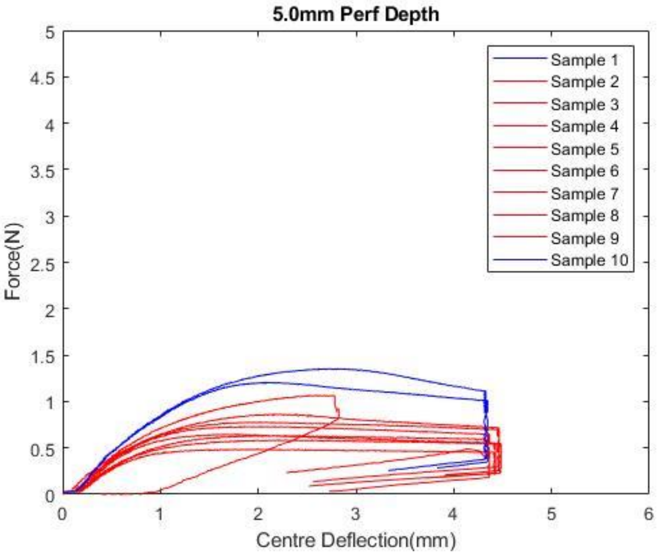
5.0mm Perf Depth
Force(N)
Centre Deflection(mm)
0
0.5
1
1.5
2
2.5
3
3.5
4
4.5
5
0
1
2
3
4
5
6
Sample 1
Sample 2
Sample 3
Sample 4
Sample 5
Sample 6
Sample 7
Sample 8
Sample 9
Sample 10

(b)

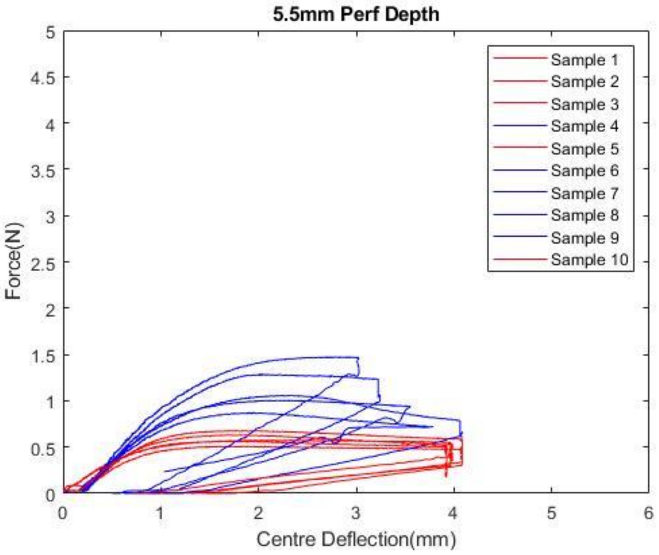

(c)

Figure 7-10: Force-deflection curve of mechanically perforated CFB samples where a) 4.5 mm depth b) 5.0 mm depth and c) 5.5 mm depth. (Blue colour is the samples that had perforation holes in between the flute peaks on the bottom liner and red line is the samples that had perforation on the flute peaks on the bottom liner)

From Figure 7-10, it was evident that the behaviour due to the series position of perforated holes not only existed in laser perforated samples, but also in mechanically perforated samples. It is worth mentioning that the perforation was done randomly at the start of the experiment, which is the reason why the 5.0 mm depth group had only two samples on peaks. Coincidentally, the rest of the perforated samples including laser perforated had 5 out of 10 samples on each position.

The findings suggested that for a perforation spacing that is close to the pitch of the CFB (in this research 3 mm perforation spacing and 2.5 mm pitch of CFB), there is an opportunity to optimise its bending performance (by up to 100% improvement) based on the position of the perforation.

7.3 C-Flute CFB: Experimental and FE Model of Four-Point Bending on Laser Perforated CFB

In Chapter 4.2.5, the development of a FE model was presented to predict the four-point bending test and ECT of CFB. It is unlikely that the ECT test can be carried out successfully on perforated samples as the samples will fail even before the test starts due to localized failure in the material remaining between perforation holes. For this reason, this work was solely focused on the four-point bending of perforated CFB. The type of board selected was C-flute CFB instead of B-flute CFB due to difficulties in obtaining the material properties of the latter.

The material properties of the C-flute CFB was presented in Table 2-4, Table 4-1, Table 4-2 and Table 4-3 while the geometry of the model was constructed using arc-and-tangent (Urbanik, 2001) curve on Solidworks which was also reported in Chapter 4. The only addition to the model was the perforated line of 2 x 1 x 2 mm in the middle section of the four-point bending sample (see Figure 7-11). This perforation design was chosen based on an existing perforated box with C-flute profile in the New Zealand market.

Figure 7-11: Laser perforated C-flute CFB sample used in this experiment with a perforation design of 2 x 1 x 2 mm.

The setup and boundary conditions of the model followed the same as reported in Chapter 4.2.4 and extended to add the perforation line. The mesh was a quadratic element with a size of 1 mm (further refinement did not yield any improvements) and anvils was displaced by 10 mm. In total, five samples of angles 0° (CD), 30°, 45°, 60° and 90° (MD) were investigated using the model. The model was run using Workbench 17.1 (Ansys Inc.).

To validate the predictions from the model, C-flute CFB (as used in Chapters 4-6) was cut using Epilog Fusion M2 laser cutter to 260 x 50.8 mm samples with perforation lines of 2 x 1 x 2 mm in the middle section. Similar to as in Chapter 4, ten replicates of five angles of flute were chosen. These were 0° (CD), 30°, 45°, 60° and 90° (MD). The samples were conditioned in accordance to TAPPI T 420 prior to the four-point bending test that was carried out following TAPPI T 820. The apparent bending stiffness was calculated based on the bending stiffness equation (4.1) presented in Chapter 4 using the force and centre deflection data obtained from the experiment.

The experimental and model results were compared by assessing the apparent bending stiffness, maximum bending force and failed regions of the sample.

7.3.1 C-Flute Apparent Bending Stiffness

Figure 7-12 compares the apparent bending stiffness of perforated C-flute CFB from the experiment and FE model, and the undamaged bending stiffness of the experiment and the modified FE model. Experimental data is presented as mean and standard deviation.

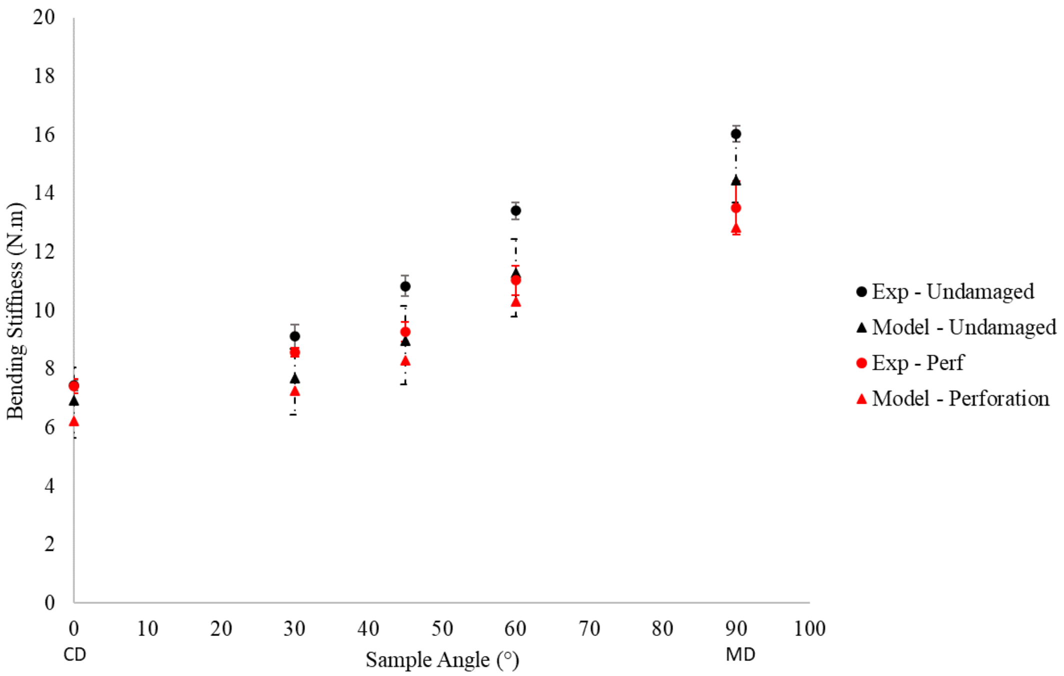

Figure 7-12: The apparent bending stiffness of undamaged and perforated C-flute CFB samples orientated at different angles displaying the experimental and FE model results. Error bars are +/- 1 SD (n=10). (Refer Appendix B for Tukey post-hoc and t-test results)

A one-way ANOVA and Tukey pos-hoc analysis on the experimental perforated samples revealed that the apparent bending stiffness between all angles had a statistically significant difference between each other ($p < 0.05$). It was observed that the differences between the experimental results of undamaged and perforated samples increased moving from 0° to 90° perforation angles. To compare both samples at each angle, a t-test analysis was carried out which showed that only samples perforated at 0° had no significant difference ($p > 0.05$) while the rest of the groups showed significant differences between undamaged and perforated samples ($p < 0.05$).

The results from the FE model also showed that perforated samples had lower apparent bending stiffness compared to undamaged samples. The results demonstrated that the FE model can predict the apparent bending stiffness following the same trend observed from the experiment but under predicted apparent bending stiffness by approximately 5%

- 16%. This may be due to not considering the properties of the glue in the model, which may add more stiffness to the CFB (Gilchrist et al., 1999).

7.3.2 C-Flute Maximum Bending Force

Figure 7-13 presents the maximum bending force of perforated C-flute CFB from the experiment and FE model, and the undamaged samples from experiment and FE model that was presented and discussed in Chapter 4. Data is presented as mean and standard deviation.

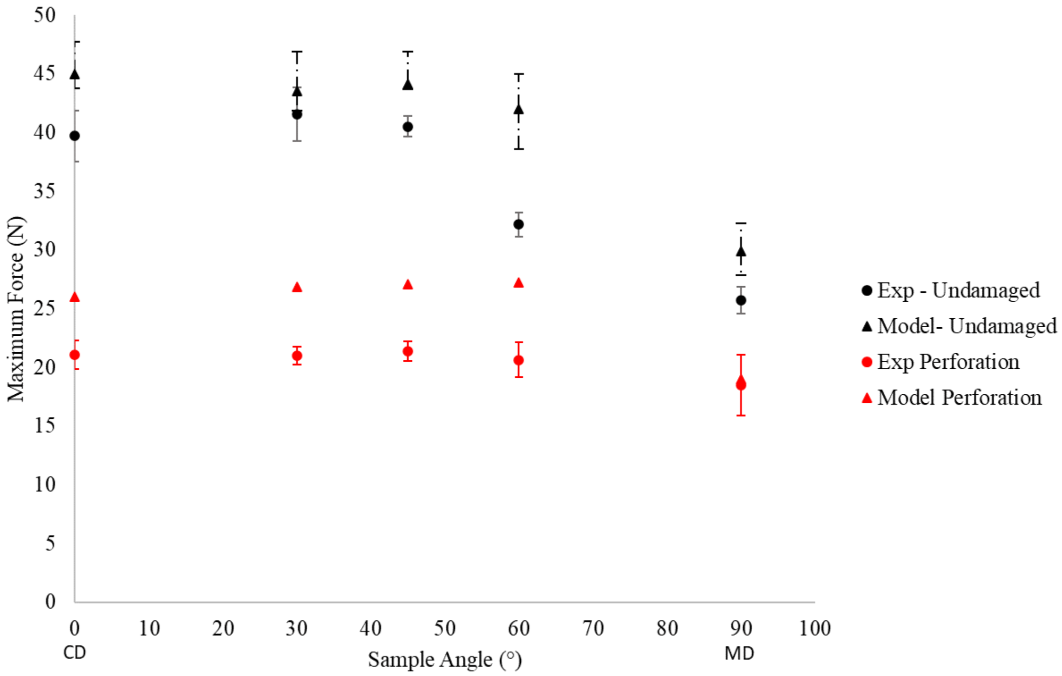

Figure 7-13: The maximum bending force of undamaged and perforated C-flute CFB samples orientated at different angles displaying the experimental and FE model results. Error bars are +/- 1 SD (n=10). (Refer Appendix B for Tukey post-hoc and t-test results)

A one-way ANOVA and Tukey pos-hoc analysis on the experimental perforated samples revealed that the maximum bending force between angle 0° and 60° were not significantly different ($p > 0.05$) but they were all found to be significantly higher than the maximum bending force at 90°. Interestingly, the same pattern was found in the FE model of perforated samples.

Compared to the undamaged samples, both experimental and FE model results of perforated samples showed significant drops (experiment: $p < 0.05$) which proved that perforation has an impact on the strength performance of CFB.

7.3.3 C-Flute Failure Comparison

Figure 7-14 presents the failure plot from the Tsai-Wu criterion in the FE model compared with the experimental samples after going through the four-point bending test.

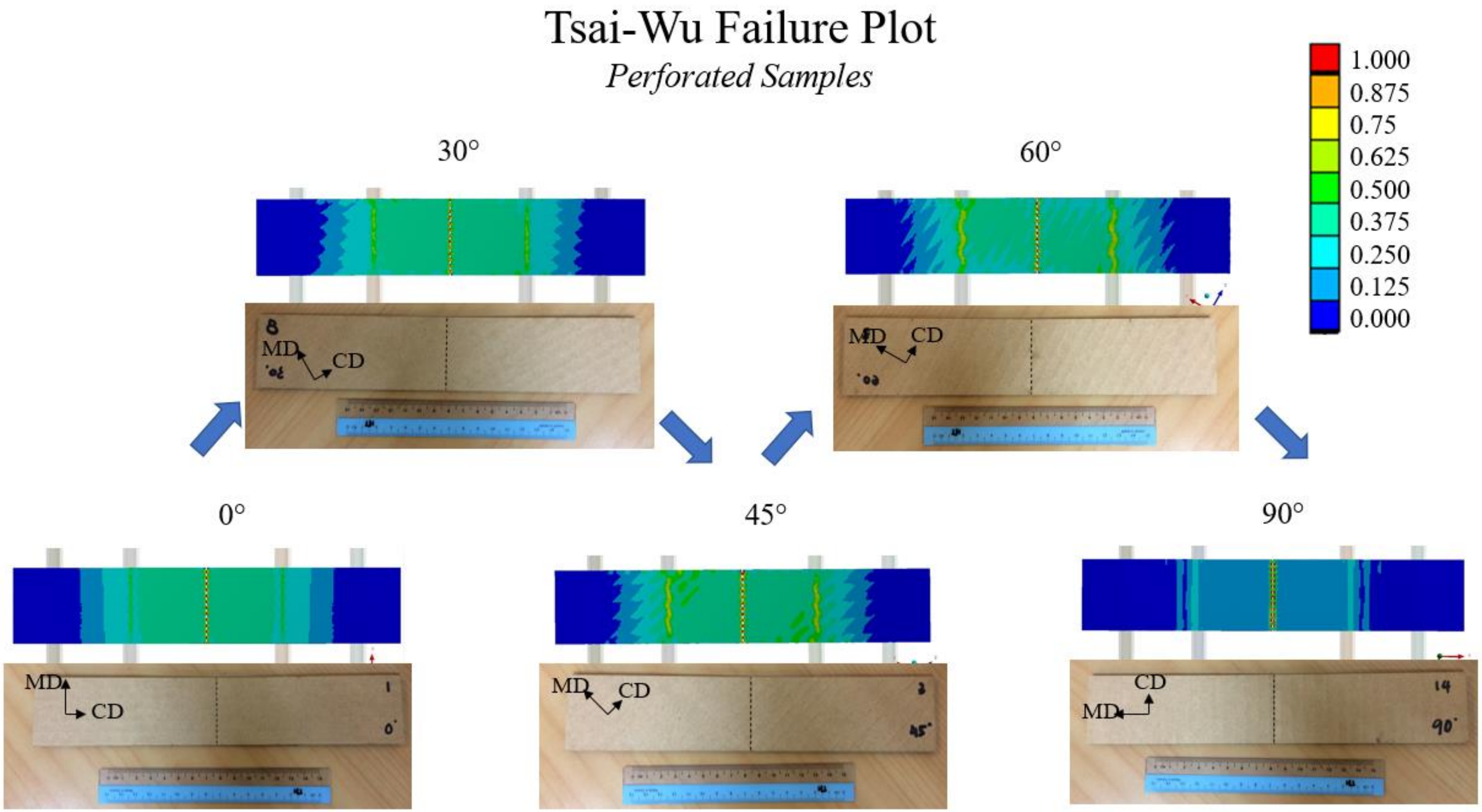

Figure 7-14: Tsai-Wu failure criterion from FE model and experimental samples of perforated C-flute CFB orientated at different angles.

Unlike the undamaged samples where failure propagates based on the orientation of the flute (see Figure 4-10), the addition of perforation caused failure to propagate along the perforation line in any orientation showing that the addition of perforation can cause a shift in the locus of failure. This was observed experimentally and numerically from Figure 7-14 which demonstrated the ability of FE model to be used in understanding the behaviour of perforation design on CFB.

7.4 Further Analysis

In the previous section, the use of FE model was demonstrated to predict the bending performance of CFB with reasonable accuracy. It was also shown that the maximum bending force can be different depending on whether the perforation holes lie on the peaks of the flute or in between the peaks on the bottom liner (compressive side during bending). Due to these reasons, it was decided to extend the FE model that was developed and used in both Chapter 4 and Chapter 6 to see how well it can predict this behaviour.

As the material properties and raw materials to obtain the material properties of B-flute CFB used in this research study were not available, the model uses the material properties of C-flute CFB but with a B-flute geometry. Hence, the outcome from the model was only valid to explore whether the position of the perforation relative to the flute altered failure in a similar trend to what was observed in section 7.2.2 but not the absolute values such as bending stiffness and maximum bending force as it would not be accurate.

Figure 7-15 shows the geometry of the FE model and how the perforation region looks with perforation on the peaks and in between the peaks of the flute on the bottom liner. The setup of the model remained the same with a quad mesh of 1 mm but both models were set to be displaced by 5 mm (reduced displacement due to the smaller flutes failing at lower displacement). Further details about the model can be found in Chapter 4.2.4.

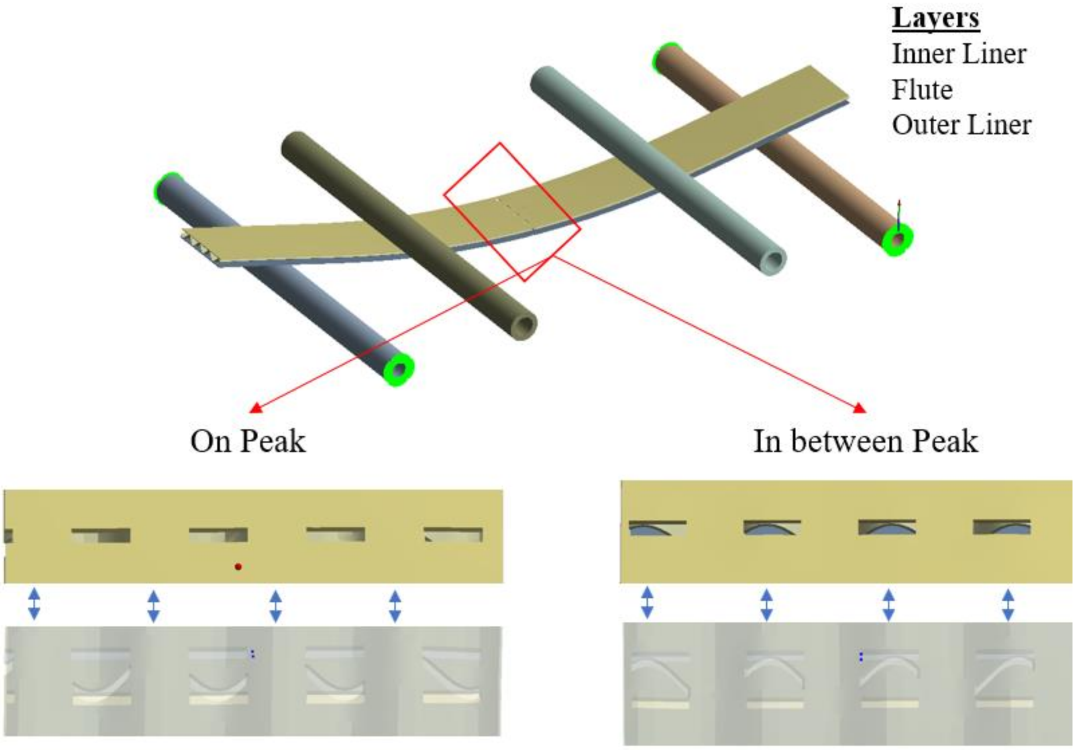

Figure 7-15: The geometry of the four-point bending model showing the perforated region with different perforation position on CFB.

Figure 7-16 shows the Tsai-Wu failure plot of predictions with perforations on the peaks of flute and with perforations in between the peaks of flute. Six sub-steps images are presented with the aim of comparing the first failure point found in the analysis which is when the Tsai-Wu index has a value of more than 1.

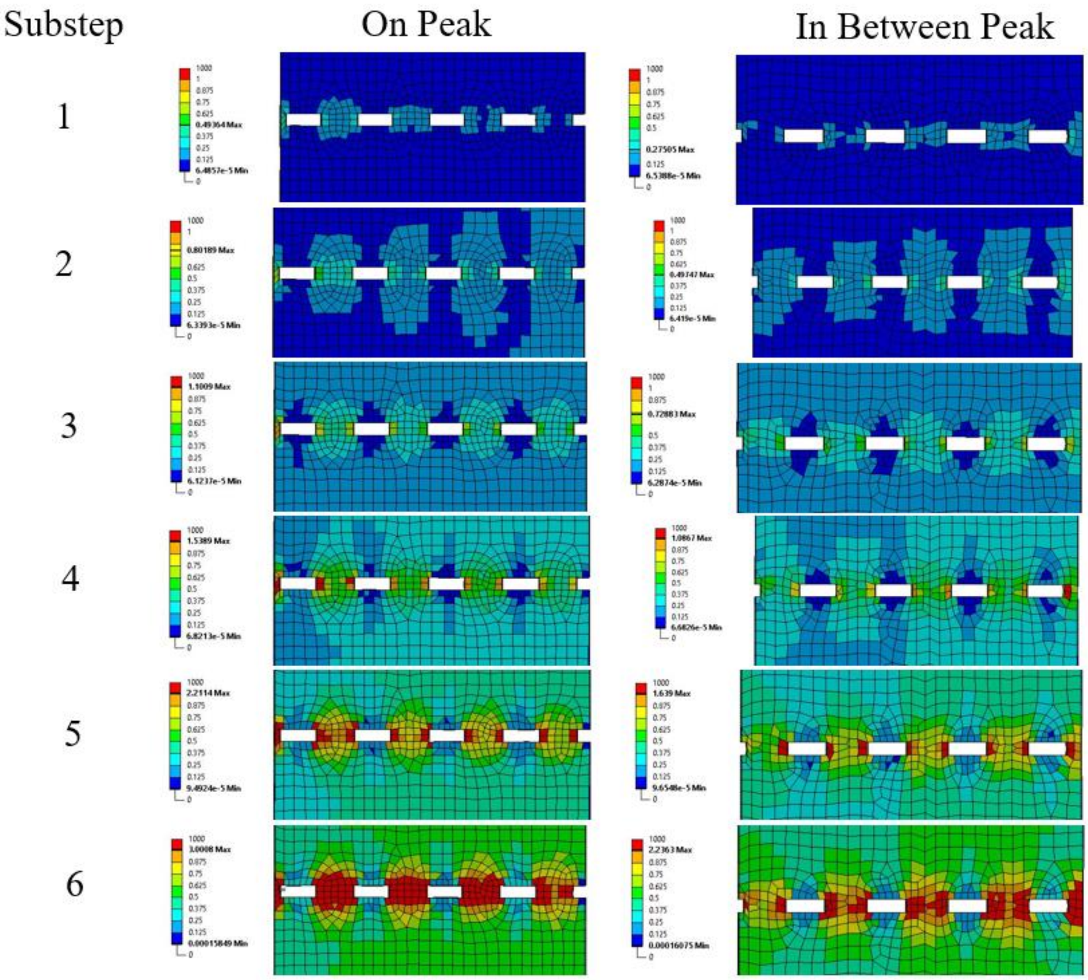

Figure 7-16: Tsai-Wu failure plot at the perforated region on the bottom liner(compressive side) of the two models from sub-step 1 to sub-step 6.

From Figure 7-16, the first point of failure in the model with perforation on peaks of flute was at substep 3 while it was at substep 4 for the perforation in between the peaks of flute. At substep 6, it was observed that the region between each perforated hole for the model with perforation on peaks of flute had more failure elements (red coloured) as opposed to when the perforation is in between the peaks. The FE model was therefore able to predict failure at lower load related to perforation location as seen experimentally in Figure 7-8, Figure 7-9 and Figure 7-10. This finding suggested that the FE model will be useful in understanding the effect of perforated holes on the strength performance of CFB.

7.5 Conclusion

A number of conclusions can be drawn from this chapter. The apparent bending stiffness decreased with addition of laser perforation compared to undamaged samples, and further decreased with addition of mechanical perforation due to indentation damage that occurred during the formation of the perforations. The strength of CFB based on its maximum bending force can be altered depending on the position of perforation line relative to the flute peaks on inner liner. This works best for perforation spacing that are similar in magnitude to the flute pitch. The utility of the FE model was demonstrated through its ability to capture the behaviour observed from the experiment accurately while also predicting the bending stiffness with good accuracy.

The FE modelling approach could be extended to enable its use in optimising perforation design such that damage to the overall mechanical performance of CFB packaging could be minimised.

Reference

Gilchrist, A., Suhling, J., & Urbanik, T. (1999). Nonlinear finite element modeling of corrugated board. The 1999 ASME Joint Applied Mechanicals and Materials Division Meeting. Blacksburg, New York, USA; pp. 101–106.

Hermansson, A. (1999). Openability of retail packages. Packaging Technology and Science: An International Journal, 12(5), 219-223.

Jinkarn, T., Boonchu, P., & Bao-Ban, S. (2006). Effect of carrying slots on the compressive strength of corrugated board panels. Kasetsart Journal: Natural Science, 40(6), 154-161.

Neidoni, N., Bolos, V., & Buzdugan, M. I. (2009). Experimental optimization of perforations for corrugated board boxes. The International Conference Interdisciplinarity in Engineering INTER-ENG (p. 287). Elsevier Limited.

Urbanik, T. (2001). Effect of corrugated flute shape on fibreboard edgewise crush strength and bending stiffness. Journal of Pulp and Paper Science, 27(10), 330-335.

Chapter 8.

Conclusion and Future Recommendation

8.1. Conclusion

This research set out to develop tools and models to explore the link between damage (either local or global) of corrugated fibreboard, to reductions in mechanical performance. This was achieved through development of a new image analysis-based method to evaluate flute morphology, and the development and comparison of a range of mathematical models to predict pre- and post-damage performance. These tools and models were applied to globally damaged (crushed) and locally damaged (perforated) CFB. Through these investigations the utility of the models were demonstrated for prediction of performance but also to decouple the effects of changing flute morphology from micro-scale damage to paper structure or liner-medium adhesion. The flute morphology analysis developed in Chapter 3 can be used to characterise the morphological change of the fluting structure when CFB is subjected to mechanical damage. This technique is novel and takes advantage of the functionality of laser cutting to provide cross sections without the application of forces. Previous preparation methods, such as using sharp blades have the potential to change the structure during sampling. In this work it was applied to evaluate global damage and the Similarity Factor (SF) was derived to allow comparison between samples and either ideal or pre-damaged flute structures. In Chapter 7 it was applied to characterise changes to flute morphology in samples that had been locally damaged (mechanical perforations).

Beyond the scope of this work, the method could be applied in CFB research to characterise existing damage prior to testing or after failure during testing. For example, the technique could be used to compare flute geometries between CFB boxes that exhibit variation in performance during cyclic humidity or vibrational testing, or to screen boxes used in these trials to reduce variability. Similarly, in industry the technique could be used as a quality control tool to ensure optimal corrugator or converting operation. Samples taken from the single-facer or double-backer could be analysed using this technique and used to investigate how changes to operation (such as paper grade or machine speed) impact flute morphology. Optimisation of converting lines could be carried out where trade-offs between print and die cutting quality against physical damage to the CFB structure.

This work also investigated the link between changes to flute morphology (measured using this technique) and changes to mechanical performance of the CFB. The new technique allowed comparison between the flute morphology with bending stiffness, ECT and dynamic shear testing (DST). In Chapter 5 a similar trend was found with respect to increasing damage (crush), bringing new insights, in that both calliper and flute geometry changes have an influence on the mechanical strength of CFB. In the experiments carried out in Chapter 5, the flute morphology was captured after the CFB had relaxed after the crushing process. More detailed experimental work could be made to identify what level of damage must be done in order that the flute morphology does not recover. Similarly experiments where repeated crush-relaxation cycles are applied to determine when irrecoverable flute deformation begins to occur.

In Chapter 5, it was seen that DST had higher sensitivity compared to other performance tests. Changes in DST performance were seen at crush levels that did not show changes to either flute morphology, bending or compression results. As the effect of the flute structure was already eliminated through the flute morphology analysis, this suggest that the crushing might cause other localised damage to the fibres in the constituent papers or in flute-liner adhesion that impacted the torsional behaviour of CFB and caused significant drop in the DST measurement. It is reported that DST provides information about the fluted component of CFB, but this analysis demonstrates that it might provide information about damage to the fluting medium itself, rather than its geometry.

With the success of FE modelling work developed in Chapter 4, it was shown that the models can also be used to predict the bending and edge-crush test performance of CFB. This was extended to the inclusion of mechanical damage by inclusion of the measured flute geometries as shown in Chapter 6 for crushing and in Chapter 7 for perforation. The addition of flute structure with an actual morphology damage in the model allowed for a better accuracy in predicting the ECT and can be useful for models that require an understanding of localised damage structure.

The findings from Chapter 6 also saw that the FE models were still limited in that they under predicted normalised performance at high degrees of damage. It is believed that this was due to the delamination of the flute paper, due to the crushing, an effect that was not present in the model. Such delamination and/or damage to flute-liner adhesion may cause the liners to decouple from each other, hence, affecting the performance significantly. In Chapter 7, the FE model predicted the apparent bending stiffness of laser perforated CFB accurately and also demonstrated its effectiveness in capturing the behaviour observed experimentally. The success in the FE modelling work could be extended in a range of applications as to apply it for a range of different papers for strength optimisation, in finding optimal design of perforation line shape and location for specific requirements and even for finding the optimal flute structure that can give the best strength performance of CFB.

Perforations to CFB was shown to decrease the apparent bending stiffness of the CFB no matter what angles they are orientated to the flute. This provided an insight that as compared to undamaged samples, the perforation shifted the locus of failure towards the perforated region. This finding leads to the idea of using localised damage such as perforations to pre-define where and how failure will occur. Potentially by shifting stresses to other parts of a box design in this way, improved overall performance could be achieved. It was also shown (both experimentally and through FE modelling), that the position of perforations relative to the flute peaks significantly impacts performance. By avoiding punching through flute peaks that rest on the compressive side of the liner, it is possible to improve the maximum bending force of CFB.

8.2. Future Recommendation

The work carried out in this thesis has provided new knowledge around the global and localised mechanical damage to the fluting structure of CFB and models to predict the effects of this damage to the mechanical performance of CFB. Though out the research, new questions were asked which could potentially be explored further to gain valuable knowledge around the mechanical performance of CFB. Some potential directions for future work based on the tools and models developed in this work are to:

- Investigate the damage mechanisms occurring during crushing. Chapter 3 and Chapter 5 were focused on measuring the flute structure after the crushing process. Modifications to this measurement could be made to follow damage initiation during crushing. This could be carried out by applying a resin mixture at different points during crushing to harden the structure which could then be laser cut using the same methodology developed in Chapter 3 and the morphological change could be quantified. The difference between the state of the flute at crushing and after crushing could provide insights into the mechanism of flute structural damage.
- Use the flute morphology analysis to analyse the flute structure at each step along the CFB manufacturing process to be able to identify processes that cause significant impact to the flute structure and improve it for a better board quality. Biancollini (2005) undertook a similar study along the manufacturing process but this was limited to visual observation. By being able to actually quantify the morphological change, the differences between each step along the way could be monitored.
- Applying the models developed in Chapter 4 for a range of different papers that will enable finding the optimal combination of papers to make CFB with specific

requirements such as lowest cost and grammage. Figure 8-1 shows some preliminary work currently carried out by the author of an example of what could be achieved here using the analytical solution from Chapter 4. The properties of seventeen different types of commercial papers were obtained online (Svenska Cellulosa AB, 2018; Billerudkorsnas, 2017a; Billerudkorsnas, 2017b). These were then combined to generate a total of 4913 combinations for a single wall regular slotted container CFB with the different flute types (A, C, B, E, F). The properties of the papers were used to calculate the analytical bending stiffness and ECT of each combination CFB design (which were rearranged based on the McKee's semi-empirical formula and named as the "Strength Factor" in the figure) and plotted against the total grammage of the CFB. There are obvious implications on the findings such as the minimum grammage to consider for a given flute type and restrictions on what type of paper can be practically used for the liner and flute, but it gives an at-a-glance view of what could possibly be achieved through this extension. This preliminary data suggests that from a BCT perspective generally A-Flute will provide better performance or similar performance at lower grammage than other board types. However, the analytic model for ECT, bending, and BCT do not account for interflute buckling of the liner which may lower the strength for A-flute at low grammages. This analysis could be extended to also consider other functionalities such as resistance to crushing to avoid damage during printing.

$$\text{Strength Factor} : \frac{BCT}{K*Z^{(2a-1)}} = ECT^{(a)} * \{\sqrt{(D_{MD}D_{CD})}\}^{1-a}$$

where K = 2.028, a=0.746

$$\text{Total gsm} = gsm_{inner} + TF*gsm_{flute} + gsm_{outer}$$

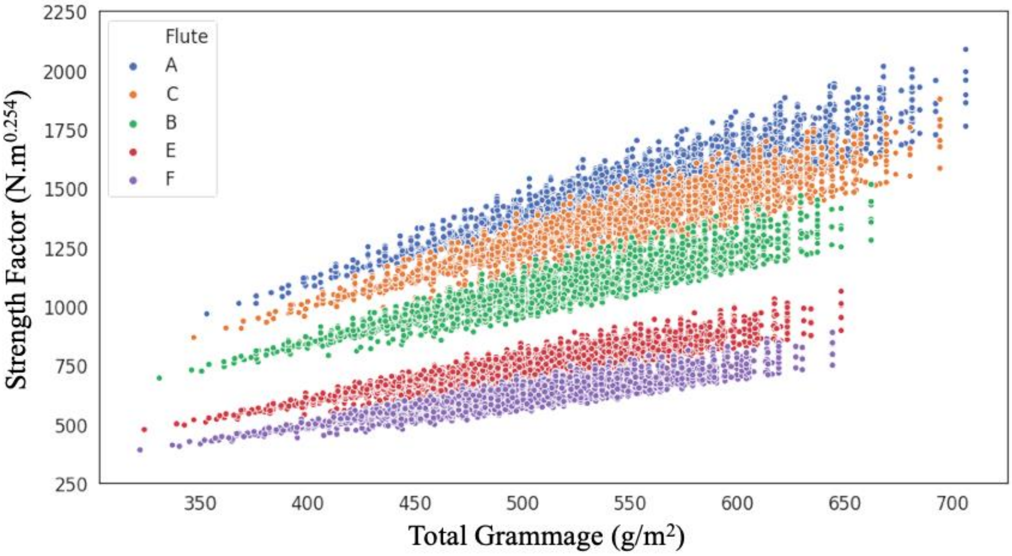

Figure 8-1: Plot of the strength factor (ECT component multiplied by the bending stiffness component using McKee's relation) against the total grammage of the CFB. The graph consisted of 4913 data that was combined from 17 types of paper available online to made up a single wall CFB. The constants from the McKee's semi-empiracal equation was used folowed from what was reported by Popil (n.d).

- Use of the actual damage on the flute morphology in modelling other tests of CFB such as flat crush test and DST where it is likely to improve and refine the sensitivity of those models. For example, in developing an FE model for a flat crush test, the use of an actual flute geometry will affect the dampening response of the structure when subjected to crushing. The use of an actual flute structure in a DST model could be interesting in finding out whether the response between different crushed level of the flute matches well with the experimental results and further explore the relative roles of flute geometry and fluting medium delamination or flute-liner adhesion damage.
- The use of the FE model to optimise the perforation design of CFB so that it could minimise the impact on the overall mechanical performance of CFB boxes. This

can be done in a number of ways such as investigating the size of perforation, the gap distance and the angles of perforation relative to the flute. It is expected that different flute types will have different optimal perforation designs.

Reference

Biancolini, M. E. (2005). Online quality control of corrugated board panel by image processing. International Journal of Computer Applications in Technology, 23(2-4), 157-165.

Billerudkorsnas (2017a). Billerudkorsnas Supreme Liner Technical data sheet; Solna Municipality, Sweden. Accessed on 14th March 2020 from https://www.billerudkorsnas.com/globalassets/billerudkorsnas/our-offer/packaging-materials/corrugating-materials/technical-data-sheet-billerudkorsnas-supreme.pdf

Billerudkorsnas (2017b). Billerudkorsnas Design Liner Technical data sheet; Solna Municipality, Sweden. Accessed on 14th March 2020 from https://www.billerudkorsnas.com/globalassets/billerudkorsnas/our-offer/packaging-materials/corrugating-materials/technical-data-sheet-billerudkorsnas-design.pdf

Popil, R. (n.d) Predicting Box Compression Strength. Georgia, USA. Accessed on 14th March 2020 from http://www.rbi.gatech.edu/sites/default/files/documents/Predicting%20Box%20Compression%20Strength_3.pdf

Svenska Cellulosa AB (2018). SCA Kraftliner; Sundsvall, Sweden. Accessed on 14th March 2020 from https://www.sca.com/en/paper/containerboard/our-products/sca-kraftliner/

Appendices

The appendices contain the supplementary work carried out based on the research from this thesis. The appendices were grouped into sections based on each chapter where Appendix A presents supplementary work from Chapter 3, Appendix B presents supplementary work from Chapter 4, Appendix C presents supplementary work from Chapter 5, Appendix D presents supplementary work from Chapter 6 and Appendix E presents supplementary work from Chapter 7. Appendix F contains the collaboration work done using the model developed in Chapter 4 that were applied using data from another research whereby this were presented and published as a conference proceedings.

Appendix A

The work in this appendix was completed based on the discussion in Chapter 3. The first subsection shows the visualisation comparison between the initial flute and the skeleton-analysed flute based on the curvatures of the tips and the flank angles.

The second subsection of in this appendix visualise the difference between the flute profiles of CFB when subjected to different extent of crushing (Figure 3-11). The curvatures of the tips and the flank angles were also denoted to clearly differentiate their differences.

A1 Initial Flute compared with Skeleton-Analysed Flute Profiles

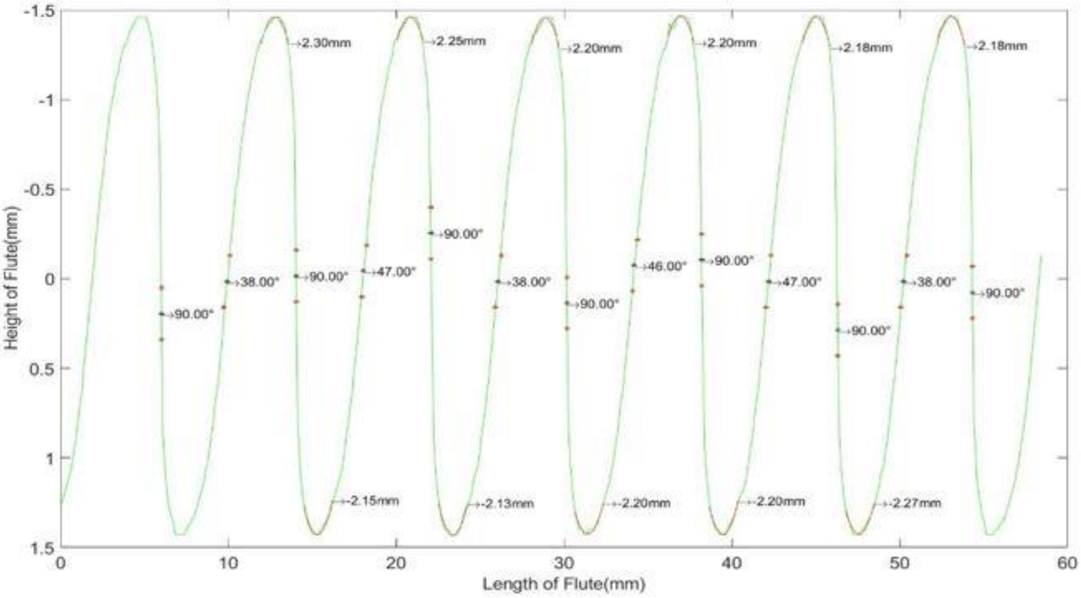

(a) Initial flute

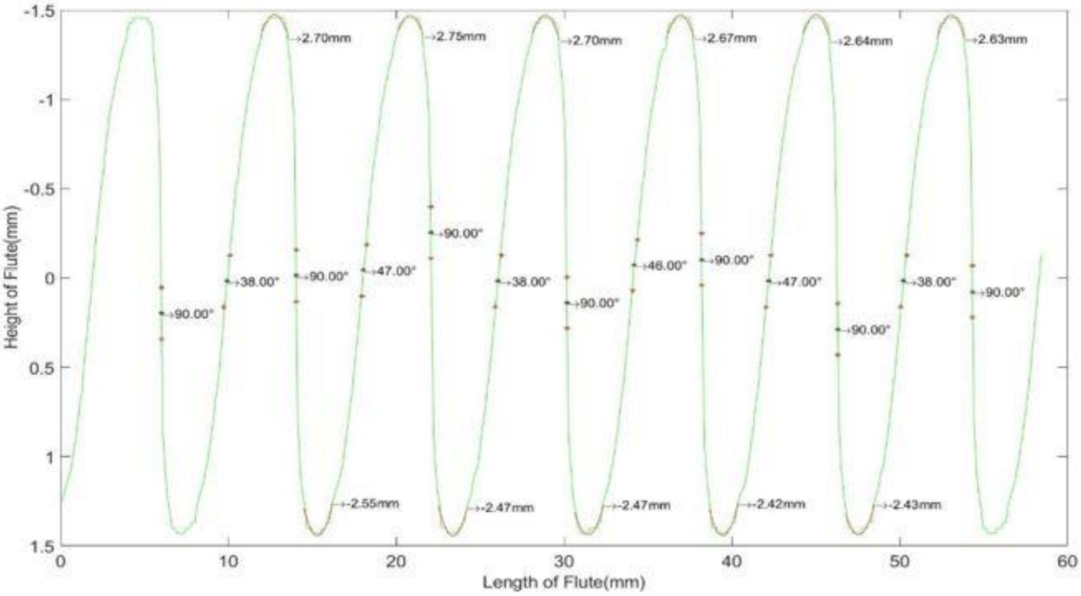

(a) Skeleton-analysed flute

Figure A-1: Illustration on measuring the curvatures of the peaks and troughs, and the flank angles between peaks and troughs on Image 3.

A2 Applying the Advanced Features on Actual Flute Profile

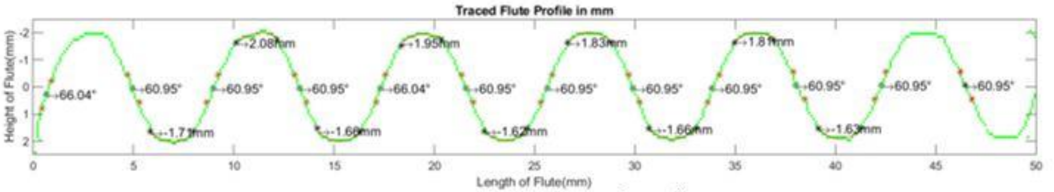

0.0 mm Uncrushed

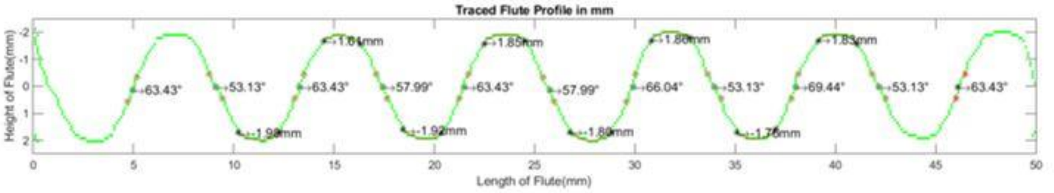

0.5 mm Crushed

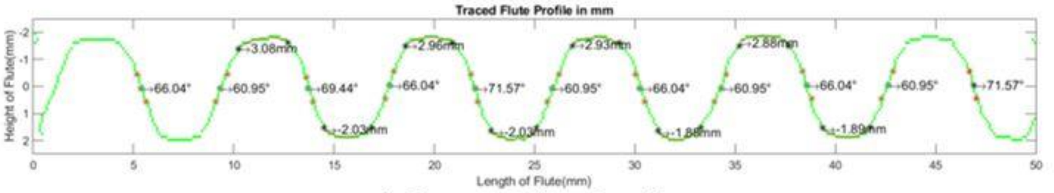

1.0 mm Crushed

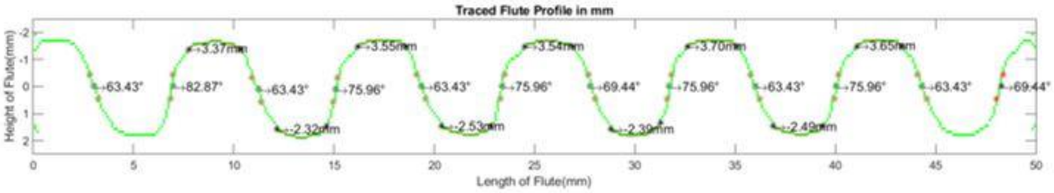

1.5 mm Crushed

Figure A-2: Illustration of applying advanced features on different level of crushing on an actual CFB flute profile. One out of ten samples from each group was used for this illustration.

Appendix B

The work in this appendix was completed based on the discussion in Chapter 4. Both Table B-1 and Table B-2 were the statistical analysis result of Tukey posthoc that were analysed on the bending stiffness and maximum bending force of different CFB sample angles during the experimental four-point bending test (the graph was presented in Figure 4-7).

Table B-1: Tukey posthoc analysis on the bending stiffness of CFB obtained from the four-point bending test.

(I) Sample Angle (°)	**(J) Sample Angle (°)**	**Mean Difference (I-J)**	**95% Confidence Interval**		**p-value**
			Lower Bound	**Upper Bound**	
0	30	-2.088539238	-1.67595671	-1.263374183	9.92E-09
0	45	-3.798057041	-3.385474514	-2.972891986	9.92E-09
0	60	-6.364449567	-5.95186704	-5.539284513	9.92E-09
0	90	-8.992770899	-8.580188371	-8.167605844	9.92E-09
30	45	-2.122100331	-1.709517803	-1.296935276	9.92E-09
30	60	-4.688492857	-4.275910329	-3.863327802	9.92E-09
30	90	-7.316814188	-6.904231661	-6.491649134	9.92E-09
45	60	-2.978975053	-2.566392526	-2.153809999	9.92E-09
45	90	-5.607296385	-5.194713858	-4.78213133	9.92E-09
60	90	-3.040903859	-2.628321332	-2.215738804	9.92E-09

Table B-2: Tukey posthoc analysis on the maximum bending force of CFB obtained from the four-point bending test.

(I) Sample Angle (°)	**(J) Sample Angle (°)**	**Mean Difference (I-J)**	**95% Confidence Interval**		**p-value**
			Lower Bound	**Upper Bound**	
0	30	-1.85875	-4.0333373	0.3158373	0.126302905
0	45	-0.81687	-2.9914573	1.3577173	0.822085377
0	60	7.53983	5.3652427	9.7144173	9.93E-09
0	90	13.96763	11.7930427	16.1422173	9.92E-09
30	45	1.04188	-1.1327073	3.2164673	0.654912317

30	60	9.39858	7.2239927	11.5731673	9.92E-09
30	90	15.82638	13.6517927	18.0009673	9.92E-09
45	60	8.3567	6.1821127	10.5312873	9.92E-09
45	90	14.7845	12.6099127	16.9590873	9.92E-09
60	90	6.4278	4.2532127	8.6023873	1.08E-08

Appendix C

The work in this appendix was completed based on the discussion in Chapter 5. Table A-1 reports the Tukey post-hoc analysis for each test (dependent variable) based on comparing the performance when subjected to different extent of crushing on CFB. This statistical evaluation allowed for comparing whether or not a statistically significant difference is observed between two levels of crushing on CFB with the ‘Sig.’ column showing the p-value result.

Table C-1: Tukey post-hoc analysis performed on the levels of crushing of CFB on different dependent variables (bending stiffness on CD, bending stiffness on MD, ECT, DST and flute morphology analysis

Dependent Variable	Group I	Group J	Mean Difference (I-J)	Std. Error	Sig.	95% Confidence Interval	
						Lower Bound	Upper Bound
Bending Stiffness on CD	0% Crush	12.5% Crush	0.0990	0.0813	0.8261	-0.1411	0.3391
		25.0% Crush	0.3050*	0.0813	0.0055	0.0649	0.5451
		50.0% Crush	0.9420*	0.0813	0.0000	0.7019	1.1821
		75.0% Crush	2.2920*	0.0813	0.0000	2.0519	2.5321
		87.5% Crush	3.0480*	0.0813	0.0000	2.8079	3.2881
	12.5% Crush	25.0% Crush	0.2060	0.0813	0.1322	-0.0341	0.4461
		50.0% Crush	0.8430*	0.0813	0.0000	0.6029	1.0831
		75.0% Crush	2.1930*	0.0813	0.0000	1.9529	2.4331
		87.5% Crush	2.9490*	0.0813	0.0000	2.7089	3.1891
	25.0% Crush	50.0% Crush	0.6370*	0.0813	0.0000	0.3969	0.8771
		75.0% Crush	1.9870*	0.0813	0.0000	1.7469	2.2271
		87.5% Crush	2.7430*	0.0813	0.0000	2.5029	2.9831
	50.0% Crush	75.0% Crush	1.3500*	0.0813	0.0000	1.1099	1.5901
		87.5% Crush	2.1060*	0.0813	0.0000	1.8659	2.3461
	75.0% Crush	87.5% Crush	0.7560*	0.0813	0.0000	0.5159	0.9961
Bending Stiffness on MD	0% Crush	12.5% Crush	0.0220	0.1611	1.0000	-0.4539	0.4979
		25.0% Crush	0.9050*	0.1611	0.0000	0.4291	1.3809
		50.0% Crush	4.0320*	0.1611	0.0000	3.5561	4.5079
		75.0% Crush	8.0880*	0.1611	0.0000	7.6121	8.5639
		87.5% Crush	9.9000*	0.1611	0.0000	9.4241	10.3759
	12.5% Crush	25.0% Crush	0.8830*	0.1611	0.0000	0.4071	1.3589
		50.0% Crush	4.0100*	0.1611	0.0000	3.5341	4.4859

		75.0% Crush	8.0660*	0.1611	0.0000	7.5901	8.5419
		87.5% Crush	9.8780*	0.1611	0.0000	9.4021	10.3539
	25.0% Crush	50.0% Crush	3.1270*	0.1611	0.0000	2.6511	3.6029
		75.0% Crush	7.1830*	0.1611	0.0000	6.7071	7.6589
		87.5% Crush	8.9950*	0.1611	0.0000	8.5191	9.4709
	50.0% Crush	75.0% Crush	4.0560*	0.1611	0.0000	3.5801	4.5319
		87.5% Crush	5.8680*	0.1611	0.0000	5.3921	6.3439
	75.0% Crush	87.5% Crush	1.8120*	0.1611	0.0000	1.3361	2.2879
Edge Crush Test	0% Crush	12.5% Crush	-0.0800	0.3778	0.9999	-1.1962	1.0362
		25.0% Crush	0.8150	0.3778	0.2746	-0.3012	1.9312
		50.0% Crush	1.9730*	0.3778	0.0000	0.8568	3.0892
		75.0% Crush	3.4230*	0.3778	0.0000	2.3068	4.5392
		87.5% Crush	5.9470*	0.3778	0.0000	4.8308	7.0632
	12.5% Crush	25.0% Crush	0.8950	0.3778	0.1856	-0.2212	2.0112
		50.0% Crush	2.0530*	0.3778	0.0000	0.9368	3.1692
		75.0% Crush	3.5030*	0.3778	0.0000	2.3868	4.6192
		87.5% Crush	6.0270*	0.3778	0.0000	4.9108	7.1432
	25.0% Crush	50.0% Crush	1.1580*	0.3778	0.0378	0.0418	2.2742
		75.0% Crush	2.6080*	0.3778	0.0000	1.4918	3.7242
		87.5% Crush	5.1320*	0.3778	0.0000	4.0158	6.2482
	50.0% Crush	75.0% Crush	1.4500*	0.3778	0.0042	0.3338	2.5662
		87.5% Crush	3.9740*	0.3778	0.0000	2.8578	5.0902
	75.0% Crush	87.5% Crush	2.5240*	0.3778	0.0000	1.4078	3.6402
Dynamic Stiffness Test (BPI)	0% Crush	12.5% Crush	1.6700*	0.2570	0.0000	0.9108	2.4292
		25.0% Crush	6.2500*	0.2570	0.0000	5.4908	7.0092
		50.0% Crush	11.1200*	0.2570	0.0000	10.3608	11.8792
		75.0% Crush	12.5100*	0.2570	0.0000	11.7508	13.2692
		87.5% Crush	12.7100*	0.2570	0.0000	11.9508	13.4692
	12.5% Crush	25.0% Crush	4.5800*	0.2570	0.0000	3.8208	5.3392
		50.0% Crush	9.4500*	0.2570	0.0000	8.6908	10.2092
		75.0% Crush	10.8400*	0.2570	0.0000	10.0808	11.5992
		87.5% Crush	11.0400*	0.2570	0.0000	10.2808	11.7992
	25.0% Crush	50.0% Crush	4.8700*	0.2570	0.0000	4.1108	5.6292
		75.0% Crush	6.2600*	0.2570	0.0000	5.5008	7.0192
		87.5% Crush	6.4600*	0.2570	0.0000	5.7008	7.2192
	50.0% Crush	75.0% Crush	1.3900*	0.2570	0.0000	0.6308	2.1492
		87.5% Crush	1.5900*	0.2570	0.0000	0.8308	2.3492
	75.0% Crush	87.5% Crush	0.2000	0.2570	0.9701	-0.5592	0.9592
Flute Morphology (SF)	0% Crush	12.5% Crush	0.0034	0.0019	0.5124	-0.0023	0.0091
		25.0% Crush	0.0143*	0.0019	0.0000	0.0086	0.0201
		50.0% Crush	0.0688*	0.0019	0.0000	0.0631	0.0745
		75.0% Crush	0.1411*	0.0019	0.0000	0.1354	0.1468
		87.5% Crush	0.1961*	0.0019	0.0000	0.1904	0.2018
	12.5% Crush	25.0% Crush	0.0110*	0.0019	0.0000	0.0053	0.0167
		50.0% Crush	0.0655*	0.0019	0.0000	0.0598	0.0712
		75.0% Crush	0.1378*	0.0019	0.0000	0.1321	0.1435

		87.5% Crush	0.1927*	0.0019	0.0000	0.1870	0.1984
	25.0% Crush	50.0% Crush	0.0545*	0.0019	0.0000	0.0488	0.0602
		75.0% Crush	0.1268*	0.0019	0.0000	0.1211	0.1325
		87.5% Crush	0.1817*	0.0019	0.0000	0.1760	0.1874
	50.0% Crush	75.0% Crush	0.0723*	0.0019	0.0000	0.0666	0.0780
		87.5% Crush	0.1272*	0.0019	0.0000	0.1215	0.1329
	75.0% Crush	87.5% Crush	0.0549*	0.0019	0.0000	0.0492	0.0606

.

Figure C-1 shows the curvature on the flute tips between different level of crushing on CFB that were obtained from analyzing the flute morphology.

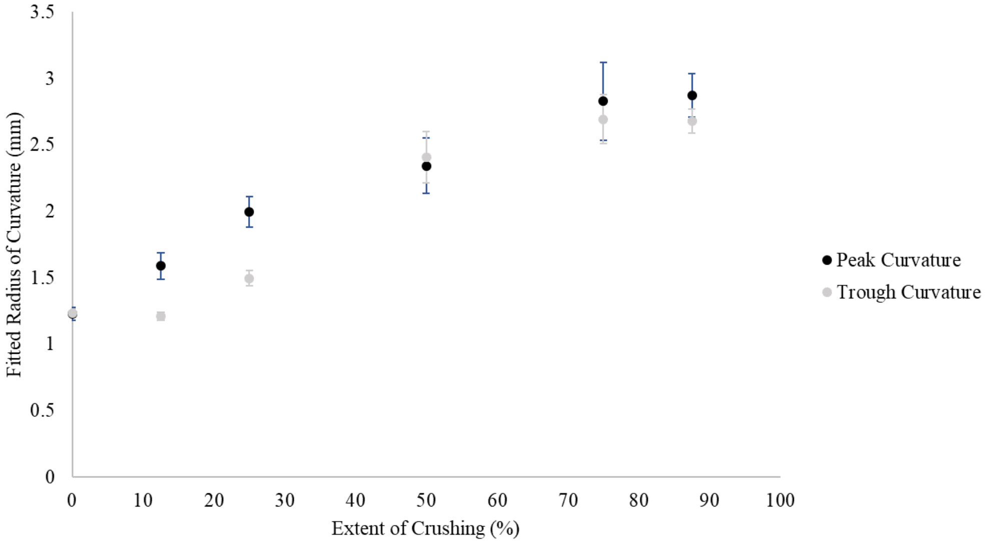

Figure C-1: Curvature on the peaks and troughs of the flute structure of CFB at different crushed levels. Note that at 12.5% and 25.0%, the peaks curvatures are large than the troughs due to the liners on the peaks is thinner than the troughs and the peaks are on the top during the crushing process.

Appendix D

The work in this appendix present on the development of the equivalent FE model reported in Chapter 6. This work was completed by the author's co-supervisor, Dr. Celia Kueh, and the author used this model to evaluate the difference between various mathematical models as discussed in Chapter 6.

Figure D-1 shows the geometrical features of CFB that were extracted for calculating homogenizing the flute structure of CFB, Table D-1 presents the geometrical parameters of the C-flute CFB and Table D-2 presents the calculation of the ABD matrix of the corrugated flute where the variables for C-flute CFB were obtained from Table 2-4, Table 4-3 and Table D-1.

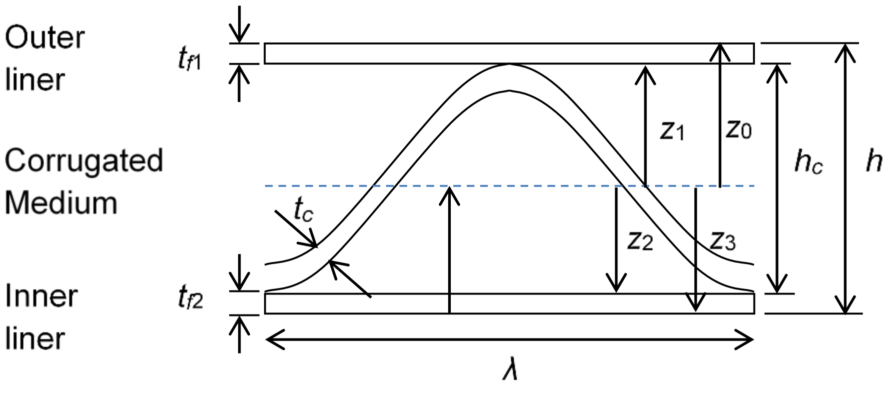

Figure D-1: CFB cross-section parameters.

Table D-1: C-flute CFB geometric parameters. Some of the variables such as t_{f1}, t_{f2}, h_c and h have been presented in Table 4-1 and Table 4-2.

Centroid, $\bar{z}$	$(t_{f2}^2/2 + (t_{f2} + h_c/2)\,h_c + (h - t_{f1}/2)\,t_{f1}) / (t_{f1} + t_{f2} + h_c)$
z_0	$h - \bar{z}$
z_1	$h - \bar{z} - t_{f1}$
z_2	$\bar{z} - t_{f2}$
z_3	$\bar{z}$

Table D-2: Stiffness matrix ABD calculations for the flute with formulae from (Biancolini et al., 2010). Note that all the orthotropic variables such as E_{11}, E_{22}, ν_{12}, ν_{21} and G_{12} are of the flute liners shown in Table 4-3 and other relations calculated based on Table 2-4.

ABD matrix of corrugated flute	
ρ core equivalent	$\rho_c (\alpha\, t_c / h_c) + \rho_{air} (1-(\alpha\, t_c/h_c))$
A_{11}	$E_{11}\, t_c /(1+6(1-\nu_{12} \nu_{21})(f^2/t_c^2)(\alpha^2 - \alpha \sin(2\pi\alpha)/(2\pi))$
A_{12}	$\nu_{21}\, A_{11}$
A_{21}	A_{12}
A_{22}	$E_{22}\, t_c\, \alpha$
A_{66}	$G_{12}\, t_c / \alpha$
D_{11}	$E_{11}\, t_c^3\, \alpha/(12\, (1-\nu_{12} \nu_{21}))$
D_{12}	$\nu_{12}\, D_{11}$
D_{21}	D_{12}
D_{22}	$E_{22}\, t_c^3/(12\, (1-\nu_{12} \nu_{21}))+E_{22}\, t_c\, f^2/2$
D_{66}	$G_{12}\, t_c^3/(12\, \alpha)$

Table D-3 presents the homogenized material properties of the equivalent flute of CFB that were calculated using the ABD stiffness matrix. This were fed as the input to the equivalent FE model that simulated the bending stiffness and ECT of CFB in Chapter 6.

Table D-3: Material properties assigned to effective flute layer of shell model. Note that all the orthotropic variables such as E_{11}, E_{22}, ν_{12}, ν_{21} and G_{12} are of the flute liner shown in Table 4-3 and other relations calculated based on Table 2-4.

Effective Corrugated Core Properties	**Equation**	**Source**
Orthotropic elasticity		
E_{11}	$(A_{11} - A_{12}^2/ A_{22})/h_c$	(Aboura et al., 2004)
E_{22}	$(A_{22} - A_{12}^2/ A_{11})/h_c$	(Aboura et al., 2004)
ν_{12}	A_{12}/A_{22}	
G_{12}	$G_{12}\, \alpha\, t_c/h_c$	(Bartolozzi et al., 2014)
G_{23}	$4\, (h_c/h)\, G_{12}\, (h_c - t_c)\, t_c/(\alpha\, P^2)$	(Nordstrand et al., 1994)

$\boldsymbol{G_{13}}$	$(h_c/h)\ 0.00275\ E_{11}\ /\ (1-\nu_{12}{}^{2})$	(Carlsson et al., 2001; Nordstrand et al., 1994)
Orthotropic Stress Limits		
$\boldsymbol{\sigma_{11t}}$	$\sigma_{11t}\ t_c/h_c$	
$\boldsymbol{\sigma_{22t}}$	$\sigma_{22t}\ \alpha\ t_c/h_c$	
$\boldsymbol{\sigma_{11c}}$	$\sigma_{11c}\ t_c/h_c$	
$\boldsymbol{\sigma_{22c}}$	$\sigma_{22c}\ \alpha\ t_c/h_c$	

Reference

Aboura, Z., Talbi, N., Allaoui, S., & Benzeggagh, M. (2004). Elastic behavior of corrugated cardboard: experiments and modeling. Composite Structures, 63(1), 53-62.

Bartolozzi, G., Baldanzini, N., & Pierini, M. (2014). Equivalent properties for corrugated cores of sandwich structures: A general analytical method. Composite Structures, 108, 736-746.

Biancolini, M., Brutti, C., & Porziani, S. (2010). Corrugated board containers design methods. International Journal of Computational Materials Science and Surface Engineering, 3(2-3), 143-163.

Carlsson, L. A., Nordstrand, T., & Westerlind, B. (2001). On the elastic stiffnesses of corrugated core sandwich. Journal of Sandwich Structures & Materials, 3(4), 253-267.

Nordstrand, T., Carlsson, L. A., & Allen, H. G. (1994). Transverse shear stiffness of structural core sandwich. Composite Structures, 27(3), 317-329.

Appendix E

The work in this appendix was completed based on the discussion in Chapter 5. Table E-1 and Table E-2 presents the Tukey post-hoc results for the apparent bending stiffness and the maximum bending force comparing between undamaged and perforated B-flute CFB.

Table E-1: Tukey post-hoc results of the apparent bending stiffness comparing undamaged and different type of perforation samples.

(I) Sample Angle (°)	**(J) Sample Angle (°)**	**Mean Difference (I-J)**	**95% Confidence Interval**		**p-value**
			Lower Bound	**Upper Bound**	
Undamaged	Laser Perf	0.01	0.13	0.24	0.02
Undamaged	4.5mm Perf Depth	0.22	0.34	0.45	0.00
Undamaged	5.0mm Perf Depth	0.33	0.44	0.55	0.00
Undamaged	5.5mm Perf Depth	0.43	0.54	0.65	0.00
Laser Perf	4.5mm Perf Depth	0.10	0.21	0.32	0.00
Laser Perf	5.0mm Perf Depth	0.20	0.31	0.42	0.00
Laser Perf	5.5mm Perf Depth	0.30	0.41	0.52	0.00
4.5mm Perf Depth	5.0mm Perf Depth	-0.01	0.10	0.22	0.07
4.5mm Perf Depth	5.5mm Perf Depth	0.09	0.20	0.31	0.00
5.0mm Perf Depth	5.5mm Perf Depth	-0.01	0.10	0.21	0.11

Table E-2: Tukey post-hoc results of the maximum bending force comparing undamaged and different type of perforation samples.

(I) Sample Angle (°)	**(J) Sample Angle (°)**	**Mean Difference (I-J)**	**95% Confidence Interval**		**p-value**
			Lower Bound	**Upper Bound**	
Undamaged	Laser Perf	1.79	2.31	2.83	0.00
Undamaged	4.5mm Perf Depth	3.03	3.55	4.07	0.00
Undamaged	5.0mm Perf Depth	3.23	3.75	4.27	0.00

Undamaged	5.5mm Perf Depth	3.20	3.72	4.24	0.00
Laser Perf	4.5mm Perf Depth	0.72	1.24	1.76	0.00
Laser Perf	5.0mm Perf Depth	0.93	1.45	1.97	0.00
Laser Perf	5.5mm Perf Depth	0.90	1.42	1.94	0.00
4.5mm Perf Depth	5.0mm Perf Depth	-0.32	0.20	0.72	0.80
4.5mm Perf Depth	5.5mm Perf Depth	-0.35	0.17	0.69	0.88
5.0mm Perf Depth	5.5mm Perf Depth	-0.55	-0.03	0.49	1.00

Table E-3 and Table E-4 presents the Tukey post-hoc and t-test results for the apparent bending stiffness comparing between undamaged and perforated C-flute CFB at different angle of orientation.

Table E-3: Tukey post-hoc results of the apparent bending stiffness comparing undamaged and laser perforated samples at different angle of orientation.

(I) Sample Angle	(J) Sample Angle	Mean Difference (I-J)	95% Confidence Interval		p-value
			Lower Bound	Upper Bound	
0	30	-1.84	-1.16	-0.47	0.00
0	45	-2.56	-1.87	-1.19	0.00
0	60	-4.30	-3.61	-2.93	0.00
0	90	-6.78	-6.09	-5.41	0.00
30	45	-1.40	-0.72	-0.03	0.04
30	60	-3.14	-2.46	-1.77	0.00
30	90	-5.62	-4.94	-4.25	0.00
45	60	-2.42	-1.74	-1.06	0.00
45	90	-4.90	-4.22	-3.54	0.00
60	90	-3.17	-2.48	-1.80	0.00

Table E-4: T-test results of the difference in the apparent bending stiffness of undamaged and perforated samples orientated at different angles.

t-test (Undamaged vs Perf)	p-value
0°	0.64
30°	0.00
45°	0.00
60°	0.00
90°	0.00

Table E-5 and Table E-6 presents the Tukey post-hoc and t-test results for the maximum bending force comparing between undamaged and perforated C-flute CFB at different angle of orientation.

Table E-5: Tukey post-hoc results of the maximum bending force comparing undamaged and laser perforated samples at different angle of orientation.

			95% Confidence Interval		
(I) Sample Angle	(J) Sample Angle	Mean Difference (I-J)	Lower Bound	Upper Bound	p-value
0	30	-1.94	0.10	2.15	1.00
0	45	-2.32	-0.27	1.78	1.00
0	60	-1.57	0.48	2.53	0.96
0	90	0.57	2.62	4.66	0.01
30	45	-2.42	-0.37	1.67	0.99
30	60	-1.67	0.37	2.42	0.98
30	90	0.46	2.51	4.56	0.01
45	60	-1.30	0.75	2.79	0.84
45	90	0.84	2.88	4.93	0.00
60	90	0.09	2.14	4.19	0.04

Table E-6: T-test results of the difference in the maximum bending force of undamaged and perforated samples orientated at different angles.

t-test (Undamaged vs Perf)	p-value
0°	1.73E-08
30°	2.08E-10
45°	1.86E-11
60°	1.60E-09

90°	4.14E-05

Appendix F

The conference publication written by the author based on using the FE model developed in Chapter 4 is attached in this Appendix.

Modelling the Edge Crushing Performance of Corrugated Fibreboard under Different Moisture Content Levels

Aiman Jamsari[1], Andrew Nevins[2], Celia Kueh[1], Eli Gray-Stuart[1], Karl Dahm[3] & John Bronlund[1]

[1] School of Engineering and Advanced Technology, Massey University, Private Bag 11 222, Palmerston North 4442, New Zealand
[2] Bega Cheese Limited, PO Box 123, Bega NSW 2550, Australia
[3] Callaghan Innovation, 69 Gracefield Road, Lower Hutt 5010, New Zealand
a.jamsari@massey.ac.nz

Abstract. This paper investigates the performance of corrugated fibreboard (CFB) under different humidity through edge crush test (ECT). The paper components that made up the CFB also went through tensile and compressive test at different humidity levels. This paper also developed an ECT finite element model of the CFB that assume orthotropic shell behaviour. The tensile and compressive data of the paper components at different humidity levels were used as the input for the model. It was found out that there is a good agreement between the ECT results from the experiment and the model. This suggests that modelling strength of CFB in harsh environments can simply be done by reducing its paper properties.

Keywords: Corrugated Fibreboard, Edge Crush, Strength

1 Introduction

Corrugated fibreboard (CFB) is a well-known packaging material that is used for various goods and products due to being lightweight and cheap while possessing high strength and stiffness [1]. Typical single-walled CFB is made up by a fluted corrugated sheet and two flat linerboards. The fluted structure plays important role in protecting packaged goods from hazards since it acts to resists bending and pressure from any direction when anchored to the linerboards. The two main directions in CFB is known as machine direction (MD) and the cross direction (CD) where MD aligns with the manufacturing flute direction and CD corresponds normal to the flute direction.

The design of CFB constantly changes to suit requirements such as strength and storage conditions of the packaged goods. This shows that it is crucial to analyse the structural component of CFB in designing a good packaging box [2]. As emphasized by Markstrom [3], the compressive strength of CFB is a direct measure of the box's stacking strength. This is also evident as McKee, et al. [4] shows that the box crush strength will be dependent by the edge crush test(ECT), bending stiffness and perimeter of the box.

In a harsher warmer or cooler conditions such as in a cool store, the properties of CFB will decrease much more due to the relative humidity that increases the moisture content of the material [5]. The impact of an increase in humidity has been shown to accelerate the failure of the CFB under compressive loading [6], hence indicating that the reduction of properties due to the humidity levels should be included in designing a good packaging box.

This paper investigates the strength performance of CFB and its paper components through ECT, tensile and compressive test at different humidity levels as measured through moisture content. The tensile and compressive material properties of the paper components obtained at different moisture content levels were then used as the input parameters for the finite element (FE) model of the CFB under ECT test.

2 Methodology

2.1 Tensile and Compressive Test of Paper Components

The C-flute CFB used in this research is made up of 250gm^{-2} Kraft linerboard and 160 gm^{-2} semi-chemical fluting medium that are manufactured by Carter Holt Harvey., Kinleith, New Zealand (now known as Oji Fibre Solution). Samples of 15x250 mm^{2} were cut from the Kraft linerboards and semi-chemical fluting medium in the machine and cross-machine direction. Batches of 35 samples (except for Kraft MD with 28 samples) were placed in a sealable plastic container above four different saturated salt solutions at 20°C (see **Fig. 1**) to obtain the required relative humidity as shown in **Table 1**. In addition to that, one batch perp pulp type and direction was conditioned to 50% RH in accordance with EN 20 187.

Table 1. Relative humidity above saturated salt solutions at 23°C [7].

Salt	Relative Humidity
NaCl	75.5
KCl	85.1
$BaCl_2$	90.0

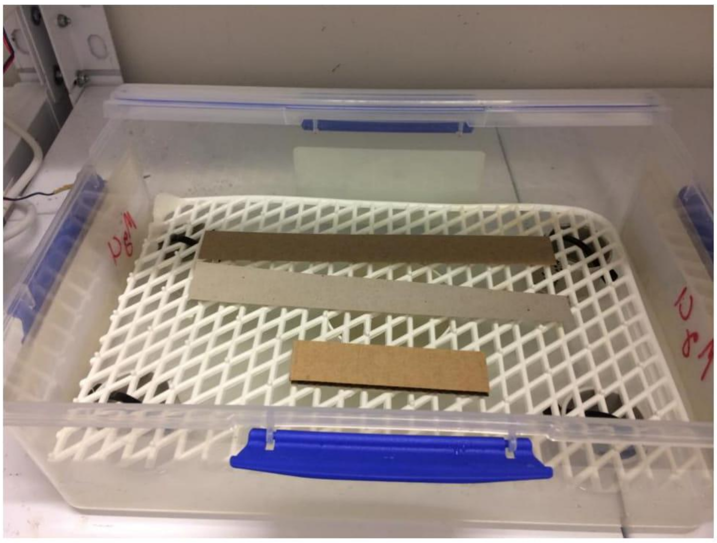

Fig. 1. $250gm^{-2}$ Kraft linerboard, $160gm^{-2}$ Semi-chemical fluting medium and ECT sample of CFB stored in a beaker above a salt solution at 20°C.

The samples conditioned above the salt solutions were then sealed in a labelled metalised film bags (Mettler Toledo PG 503-S, Switzerland). The samples were removed from their bags prior to testing and resealed again in their respective bags immediately after testing. The weight before and after testing was measured to determine their moisture content. Moisture content will be used in this study as a measure of moisture absorption as opposed to relative humidity since it is more detailed in terms of how many percent of water intake that the samples absorb.

From the batches of 35 (or 28), 15 samples (or 12 for the Kraft MD) were tested using an L & W Compression Strength Tester STFI (AB Lorentzen and Wettre, Sweden) with a clamp speed of 3 mm/min following TAPPI T 826 procedure.

The remaining 20 samples (16 for Kraft MD) were tested using an Alwetron TH1 Tensile Tester (AB Lorentzen and Wettre, Sweden). The test span was 100 mm and the clamp speed was 10 mm/min. The procedure follows TAPPI T 494.

2.2 Experimental ECT Test

C-flute CFB samples were cut to $100x25\ mm^2$ and stored in a sealable container above four different saturated salt solutions (see **Table 1**) at 20°C for 4 weeks. Each level of RH consists of 10 samples. One batch of samples was conditioned to 50% RH in accordance with EN 20 187. Similarly, the samples were removed from their bags prior to testing and resealed again immediately after testing. The weight before and after the testing was measured to determine their MC.

Platens with groves were used to provide support for the ECT test and it was conducted with a platen speed of 12.5mm/min following the FEFCO No. 8 standard procedure.

2.3 Finite Element Model of ECT

The ECT model of CFB in this study is assumed as an orthotropic shell element. Each paper component consists of 20 variables with the main variables listed down in **Table 2**. The thickness, density and Poisson's ratio for each paper components are presented in **Table 3** in the **Appendix A** while the rest of the main variables are extracted from the tensile and compressive data of the paper components. The remaining variables are computed based on the relations presented in **Table 4** in the **Appendix A**.

Table 2. The main orthotropic variables of the paper components that made up the CFB.

Variables
Thickness (mm)
Density (kg/m^3)
Elastic Modulus, E_{11}
Elastic Modulus, E_{22}
Poisson's Ratio, v_{12}
Tensile Strength, σ_{11t}
Tensile Strength, σ_{22t}
Compressive Strength, σ_{11c}
Compressive Strength, σ_{22c}

The geometry of the flute is drawn using the relations presented by Urbanik [8] that compromise of arc-and-tangent curves. This curve was drawn in Solidworks and the liners were also added to create the model of C-flute CFB (100x25 mm^2). The drawing model was then transferred to Ansys to carry out the FE simulation. A combination of static structural and ANSYS Composite PrepPost (ACP) was used to run the FE simulation where static structural performs the crushing simulation and ACP determines the failure criterion plot. Tsai-Wu failure criterion is implemented in this study where the ultimate failure of CFB is identified once the failed region reaches a full length of the pitch length.

The setup of the model was done by assuming a perfect bond between the flute and the liners. Large deformation is included to account for the geometric non-linearities. **Fig. 2** shows the illustration of the ECT model drawn in Solidworks. The mesh was set for a quadratic element with a size of 1 mm. Further refinement of the mesh does not improve the results.

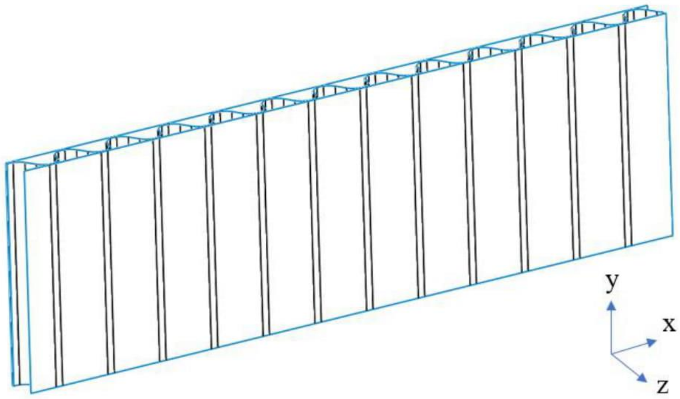

Fig. 2. Drawing model of ECT sample of C-flute CFB in Solidworks. This model was transferred to Ansys to perform the FE simulation.

3 Results and Discussion

3.1 Tensile and Compressive Strength of CFB

Fig. 3 shows the result of the short span compression test conducted on 250gm^{-2} Kraft linerboard and 160gm^{-2} Semi-chemical fluting medium at different moisture content. The moisture content of 7%db represents the moisture content expected at standard testing conditions (50%RH and 23°C).

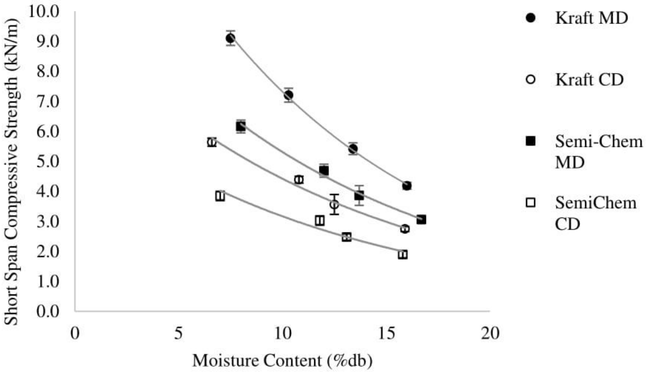

Fig. 3. The short-span compressive strength of Kraft and Semi-chemical paper measured at different moisture content levels.

It was found that the short span compressive strength measurements decrease with an exponential trend as the moisture content increases up to around 20%db. The compressive strength on MD is higher than CD for both Kraft and Semi-chemical paper. The Kraft linerboard was found to possess stronger compressive strength than Semi-chemical fluting medium.

However, on a mass basis (see **Fig. 7** in **Appendix B**), the 160gm^{-2} Semi-chemical fluting medium is stronger than the 250gm^{-2} Kraft linerboard. Kline [9] reported that the longer fibres such as in Kraft linerboard possess greater strength but the semi-chemical pulping process leaves more lignin and hemicellulose that contributes to more stiffness in the Semi-chemical fluting medium.

Fig. 4 and **Fig. 5** shows the tensile strength and tensile stiffness of the 250gm^{-2} Kraft linerboard and 160gm^{-2} Semi-chemical fluting medium at different moisture content. These results were measured from the tensile test conducted on the two types of paper.

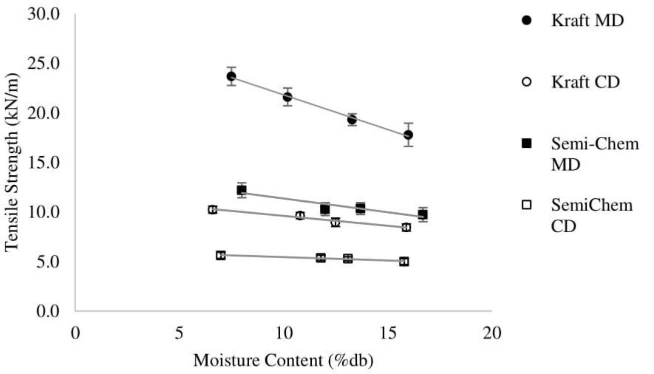

Fig. 4. The tensile strength of Kraft and Semi-chemical paper measured at different moisture content levels.

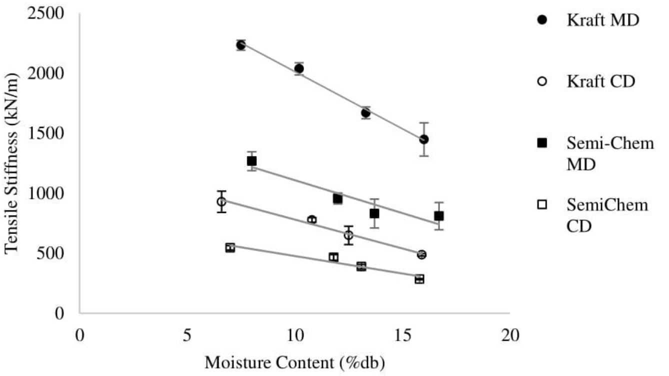

Fig. 5. The tensile stiffness of Kraft and Semi-chemical paper measured at different moisture content levels.

Similar to the results from short-span compression test, it is observed that Kraft linerboard possess stronger tensile behaviour compared to Semi-chemical fluting medium and the strength on MD is stronger than CD. It is also seen in both the tensile strength and tensile stiffness that the Kraft MD has a steeper decrease slope across the moisture content as opposed to other cases.

Unlike the compression strength results, on a mass basis (see **Fig. 8** in **Appendix B**), the Kraft linerboard is stronger than Semi-chemical fluting medium which justifies the explanation made by Kline [9] that longer and higher proportion of softwood fibres provides better fibres bonding and result in a stronger tensile strength.

From the short-span compression and tensile test results, exponential and linear equations have been fitted with the data to produce the relation of short-span compression strength, tensile strength and tensile stiffness with moisture content up to 20%db in **Appendix B**. These equations will be used to compute the main variables (**Table 2**) of each paper at different moisture content. The main variables were input in the FE model to predict the ECT performance of CFB at different moisture content.

3.2 Experiment & Modelling of ECT Test

Fig. 6 shows the experimental and modelling results of ECT on CFB at different moisture content.

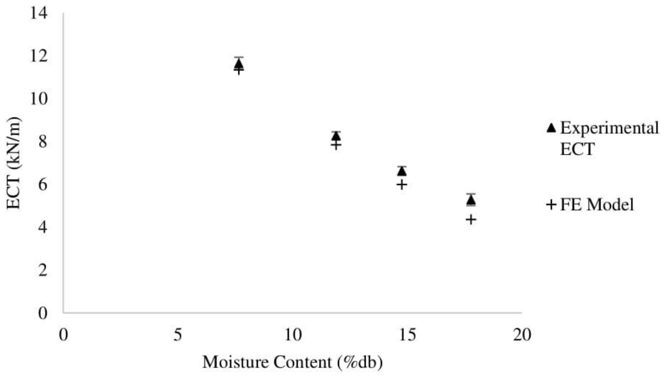

Fig. 6. The results of ECT at different moisture content based on the experiment and FE model.

It is observed that the ECT reduces as the moisture content increase. This is expected since the absorption of water will weaken the bond of the cellulose fibre of the paper material which affects the mechanical performance of CFB [10]. The reduction of ECT as the moisture content increase also show agreement with the findings from the tensile and compression behaviour of the Kraft and Semi-chemical paper in the previous section.

The FE model results show good agreement with the experimental findings where it can predict the reduction of ECT as the moisture content increase. This show that the prediction made by just reducing the material properties of the CFB paper components is enough to capture the strength behaviour at different levels of moisture content without the need of a more detailed model that includes the damages to the paper structure such as delamination and fibre breakage.

The ECT value has been shown to be useful in predicting the strength of CFB box through the Mckee formula [4]. Since the CFB boxes typically need to face harsh environments such as low temperature and high humidity during storage and handling, these factors should be considered in designing boxes that can endure these conditions. The outcome from this section shows that these factors can be accommodated in the designs by reducing the tensile and compressive material properties of the paper components in the numerical simulation.

4 Conclusion

This study investigates the tensile and compressive behaviour at different moisture level of two paper components that made up a C-flute CFB namely 250gm^{-2} Kraft linerboard and 160gm^{-2} Semi-chemical fluting medium. The different moisture level is achieved through standard conditioning room (7%db) and the use of three saturated salt which are NaCl, KCl and $BaCl_2$. Then, the strength of CFB at similar moisture level was investigated through ECT test with the inclusion of FE model to evaluate the performance of CFB.

The results in the tensile and compression test show reduction as moisture level increase. On a mass basis, the Semi-chemical fluting medium shows better specific compressive performance due to having more lignin and hemicellulose, but weaker specific tensile performance due to having shorter fibres as compared to the Kraft linerboard. Between the direction of the fibres for each paper component, the behaviour along MD is stronger than CD in all cases.

The ECT of CFB reduces as the moisture level increase. The FE model that uses the tensile and compression test of the paper components as the input parameters show good agreement with the experimental results. This shows that the strength behaviour of CFB at different moisture level can simply be modelled by using the right input parameters.

References

1. Association FB. *Fibre box handbook*: Fibre Box Association, 1999.
2. Biancolini M. Evaluation of equivalent stiffness properties of corrugated board. Composite structures 2005;**69**(3):322-28
3. Markstrom H. Testing methods and instruments for corrugated boards. Lorentz and Wettre, Kista, Sweden 1999
4. McKee R, Gander J, Wachuta J. Compression strength formula for corrugated boxes. Paperboard packaging 1963;**48**(8):149-59
5. Fadiji T, Berry T, Coetzee CJ, Opara L. Investigating the mechanical properties of paperboard packaging material for handling fresh produce under different environmental

Appendices

Appendix A

Table 3. The thickness and density of the paper component that made up the C-flute CFB used in this study.

Paper	250gm^{-2} Kraft	160gm^{-2} Semi-Chemical
Thickness (mm)	0.253	0.204
Density (kg/m^3)	791	784

Table 4. Relations from various literatures on computing the other variables as the input parameters for the FE model of CFB.

Variables	Formula	Source
E_{33}	$E_{11} / 200$	[11 12]
G_{12}	$0.387\sqrt{E_{11}.E_{22}}$	[13 14]
v_{12} & v_{13}	0.01	[15-17]
G_{13}	$E_{11} / 55$	[12 18 19]
G_{23}	$E_{22} / 35$	[12 18 19]
σ_{33t}	$\frac{4}{\sigma_{11}^2\sigma_{22}^2} > \left[\frac{1}{\sigma_{33}^2} - \left(\frac{1}{\sigma_{11}^2} + \frac{1}{\sigma_{22}^2}\right)\right]^2$	[17]
σ_{33c}	0.6 x σ_{33t}	[17 20]
τ_{12}	$\sqrt{\sigma_{11c}.\sigma_{22c}}$	[21]
τ_{13}	0.024 MPa	[19]
τ_{12}	0.024 MPa	[19]

Appendix B

Table 5. Best fit exponential equations for the compressive strength and moisture content of Kraft and Semi-chemical paper at 23°C.

Sample	Equation	R^2(%)
Kraft MD	SSCS = exp(2.878-0.08883*MC)	99.0
Kraft CD	SSCS = exp(2.274-0.07914*MC)	97.2
Semi-chem MD	SSCS = exp(2.479-0.08135*MC)	97.1
Semi-chem CD	SSCS = exp(2.052-0.08300*MC)	90.1

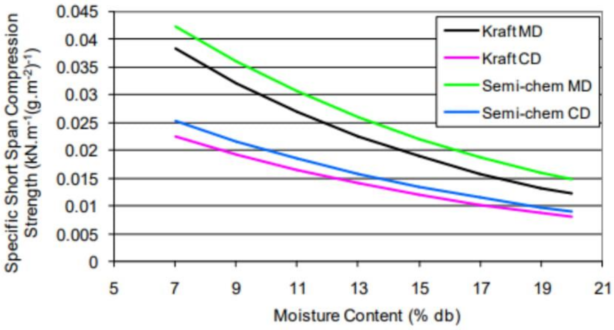

Fig. 7. Calculated specific (per unit basis weight) short span compression strength of 250gm-2 Kraft linerboard and 160gm-2 Semi-chemical fluting medium where the short span compression strength was estimated using the equations in **Table 5**.

Table 6. Best fit linear equations for the tensile strength and moisture content of Kraft and Semi-chemical paper at 23°C.

Sample	Equation	R^2(%)
Kraft MD	$TS_{gth} = 28.95 - 0.7195*MC$	92.4
Kraft CD	$TS_{gth} = 11.86 - 0.2244*MC$	87.2
Semi-chem MD	$TS_{gth} = 14.28 - 0.2854*MC$	71.1
Semi-chem CD	$TS_{gth} = 6.268 - 0.0838*MC$	63.7

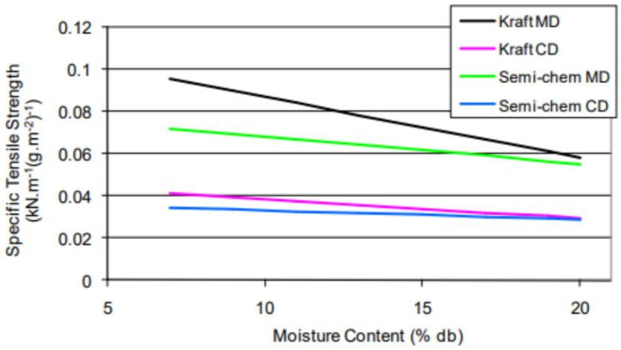

Fig. 8. Calculated specific (per unit basis weight) tensile strength of 250gm^{-2} Kraft linerboard and 160gm^{-2} Semi-chemical fluting medium where the tensile strength was estimated using the equations in **Table 6**.

Table 7. Best fit linear equations for the tensile stiffness and moisture content of Kraft and Semi-chemical paper at 23°C.

Sample	**Equation**	**R^2(%)**
Kraft MD	$TS_{stiffness} = 2979 - 97.46*MC$	95.94
Kraft CD	$TS_{stiffness} = 1240 - 47.08*MC$	96.21
Semi-chem MD	$TS_{stiffness} = 1798 - 60.11*MC$	95.12
Semi-chem CD	$TS_{stiffness} = 796.2 - 32.10*MC$	92.46

Statement of Contribution

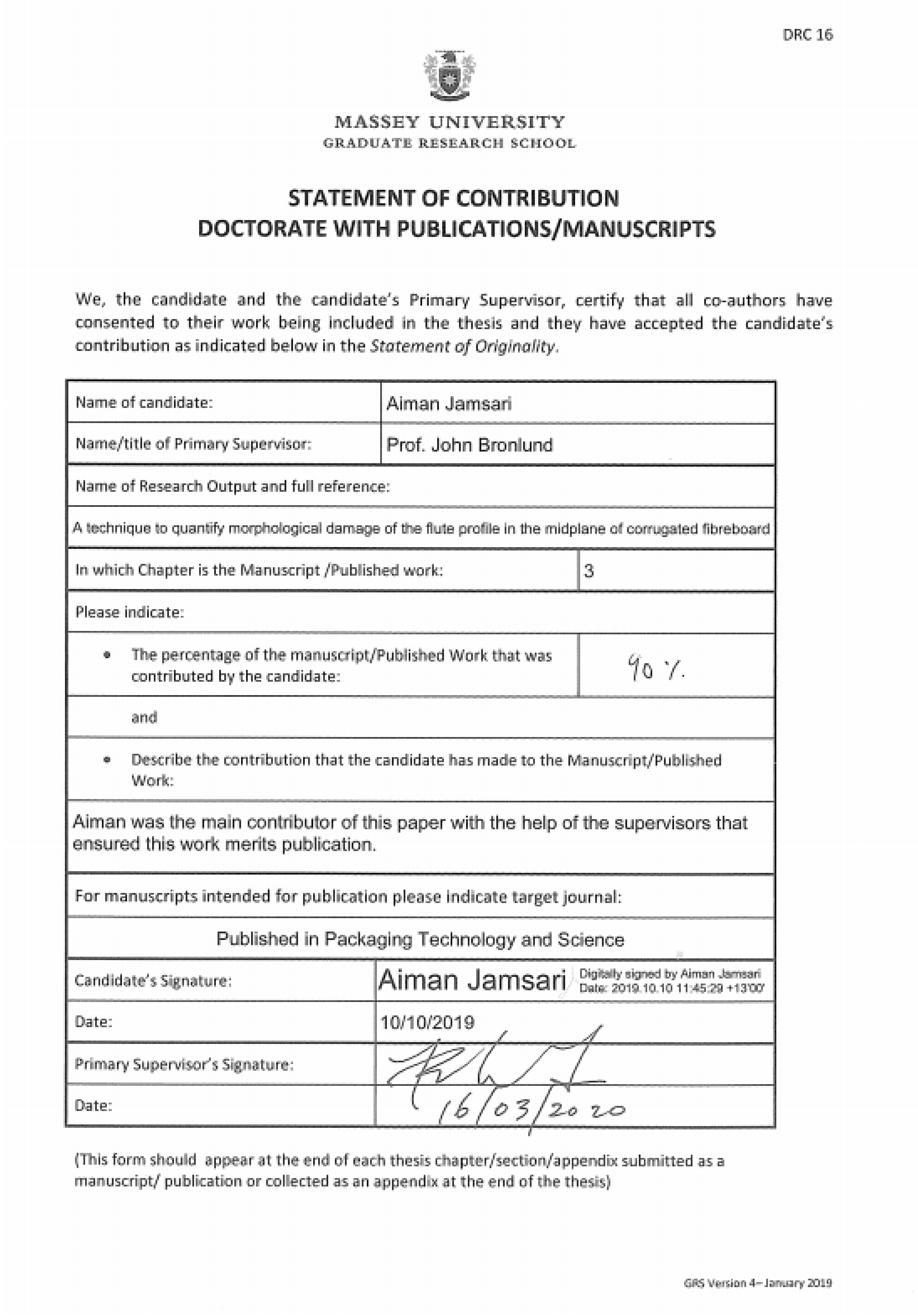

DRC 16

MASSEY UNIVERSITY
GRADUATE RESEARCH SCHOOL

STATEMENT OF CONTRIBUTION
DOCTORATE WITH PUBLICATIONS/MANUSCRIPTS

We, the candidate and the candidate's Primary Supervisor, certify that all co-authors have consented to their work being included in the thesis and they have accepted the candidate's contribution as indicated below in the *Statement of Originality*.

Name of candidate:	Aiman Jamsari
Name/title of Primary Supervisor:	Prof. John Bronlund
Name of Research Output and full reference:	
A technique to quantify morphological damage of the flute profile in the midplane of corrugated fibreboard	
In which Chapter is the Manuscript /Published work:	3
Please indicate:	
• The percentage of the manuscript/Published Work that was contributed by the candidate:	90 %
and	
• Describe the contribution that the candidate has made to the Manuscript/Published Work:	
Aiman was the main contributor of this paper with the help of the supervisors that ensured this work merits publication.	
For manuscripts intended for publication please indicate target journal:	
Published in Packaging Technology and Science	
Candidate's Signature:	Aiman Jamsari Digitally signed by Aiman Jamsari Date: 2019.10.10 11:45:29 +13'00'
Date:	10/10/2019
Primary Supervisor's Signature:	
Date:	16/03/2020

(This form should appear at the end of each thesis chapter/section/appendix submitted as a manuscript/ publication or collected as an appendix at the end of the thesis)

GRS Version 4– January 2019

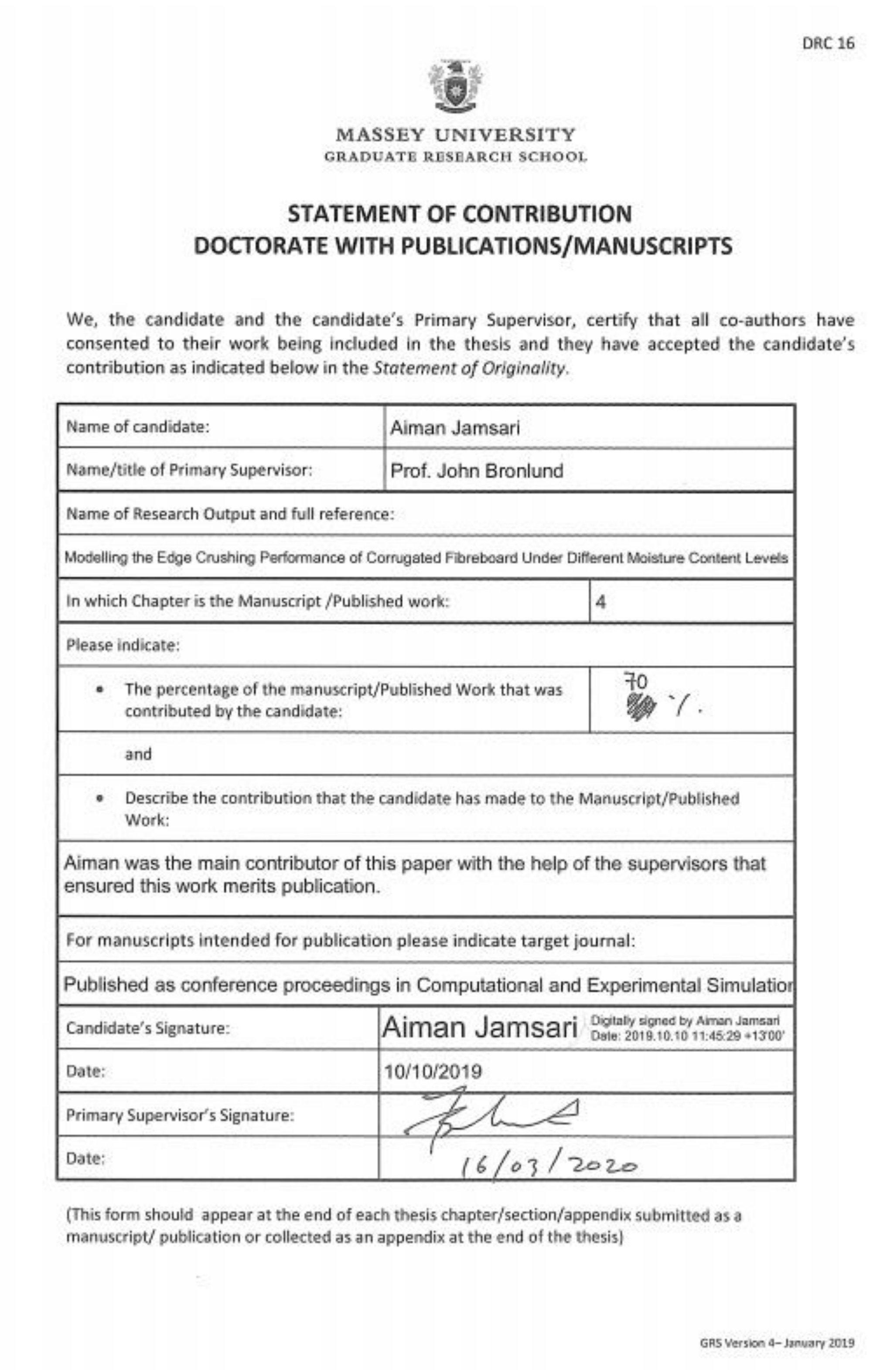

DRC 16

MASSEY UNIVERSITY
GRADUATE RESEARCH SCHOOL

STATEMENT OF CONTRIBUTION
DOCTORATE WITH PUBLICATIONS/MANUSCRIPTS

We, the candidate and the candidate's Primary Supervisor, certify that all co-authors have consented to their work being included in the thesis and they have accepted the candidate's contribution as indicated below in the *Statement of Originality*.

Name of candidate:	Aiman Jamsari
Name/title of Primary Supervisor:	Prof. John Bronlund
Name of Research Output and full reference:	
Modelling the Edge Crushing Performance of Corrugated Fibreboard Under Different Moisture Content Levels	
In which Chapter is the Manuscript /Published work:	4
Please indicate:	
• The percentage of the manuscript/Published Work that was contributed by the candidate:	70 %
and	
• Describe the contribution that the candidate has made to the Manuscript/Published Work:	
Aiman was the main contributor of this paper with the help of the supervisors that ensured this work merits publication.	
For manuscripts intended for publication please indicate target journal:	
Published as conference proceedings in Computational and Experimental Simulatio	
Candidate's Signature:	Aiman Jamsari Digitally signed by Aiman Jamsari Date: 2019.10.10 11:45:29 +13'00'
Date:	10/10/2019
Primary Supervisor's Signature:	
Date:	16/03/2020

(This form should appear at the end of each thesis chapter/section/appendix submitted as a manuscript/ publication or collected as an appendix at the end of the thesis)

GRS Version 4– January 2019

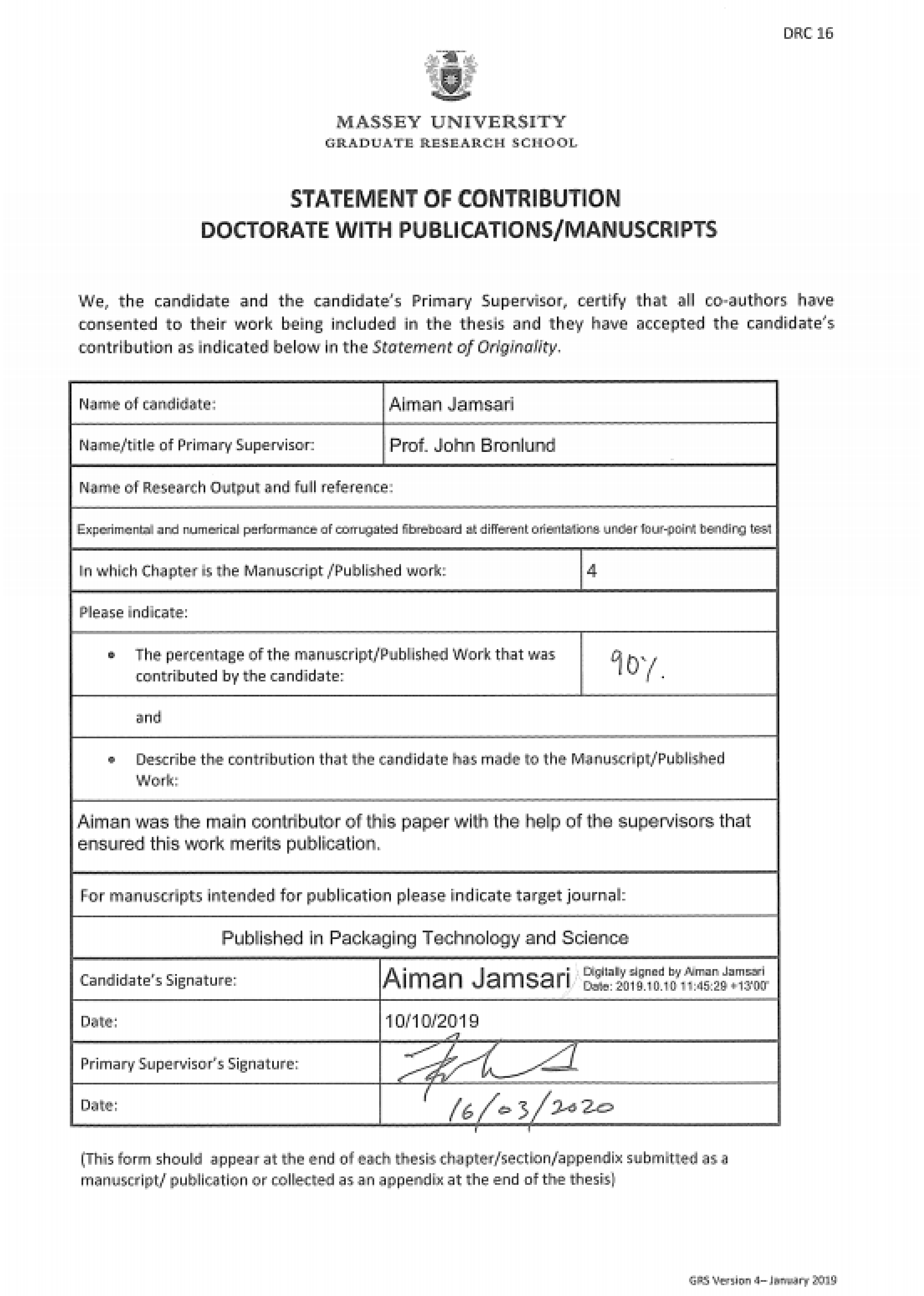

DRC 16

MASSEY UNIVERSITY
GRADUATE RESEARCH SCHOOL

STATEMENT OF CONTRIBUTION
DOCTORATE WITH PUBLICATIONS/MANUSCRIPTS

We, the candidate and the candidate's Primary Supervisor, certify that all co-authors have consented to their work being included in the thesis and they have accepted the candidate's contribution as indicated below in the *Statement of Originality*.

Name of candidate:	Aiman Jamsari
Name/title of Primary Supervisor:	Prof. John Bronlund
Name of Research Output and full reference:	
Experimental and numerical performance of corrugated fibreboard at different orientations under four-point bending test	
In which Chapter is the Manuscript /Published work:	4
Please indicate:	
• The percentage of the manuscript/Published Work that was contributed by the candidate:	90%.
and	
• Describe the contribution that the candidate has made to the Manuscript/Published Work:	
Aiman was the main contributor of this paper with the help of the supervisors that ensured this work merits publication.	
For manuscripts intended for publication please indicate target journal:	
Published in Packaging Technology and Science	
Candidate's Signature:	Aiman Jamsari Digitally signed by Aiman Jamsari Date: 2019.10.10 11:45:29 +13'00'
Date:	10/10/2019
Primary Supervisor's Signature:	
Date:	16/03/2020

(This form should appear at the end of each thesis chapter/section/appendix submitted as a manuscript/ publication or collected as an appendix at the end of the thesis)

GRS Version 4– January 2019

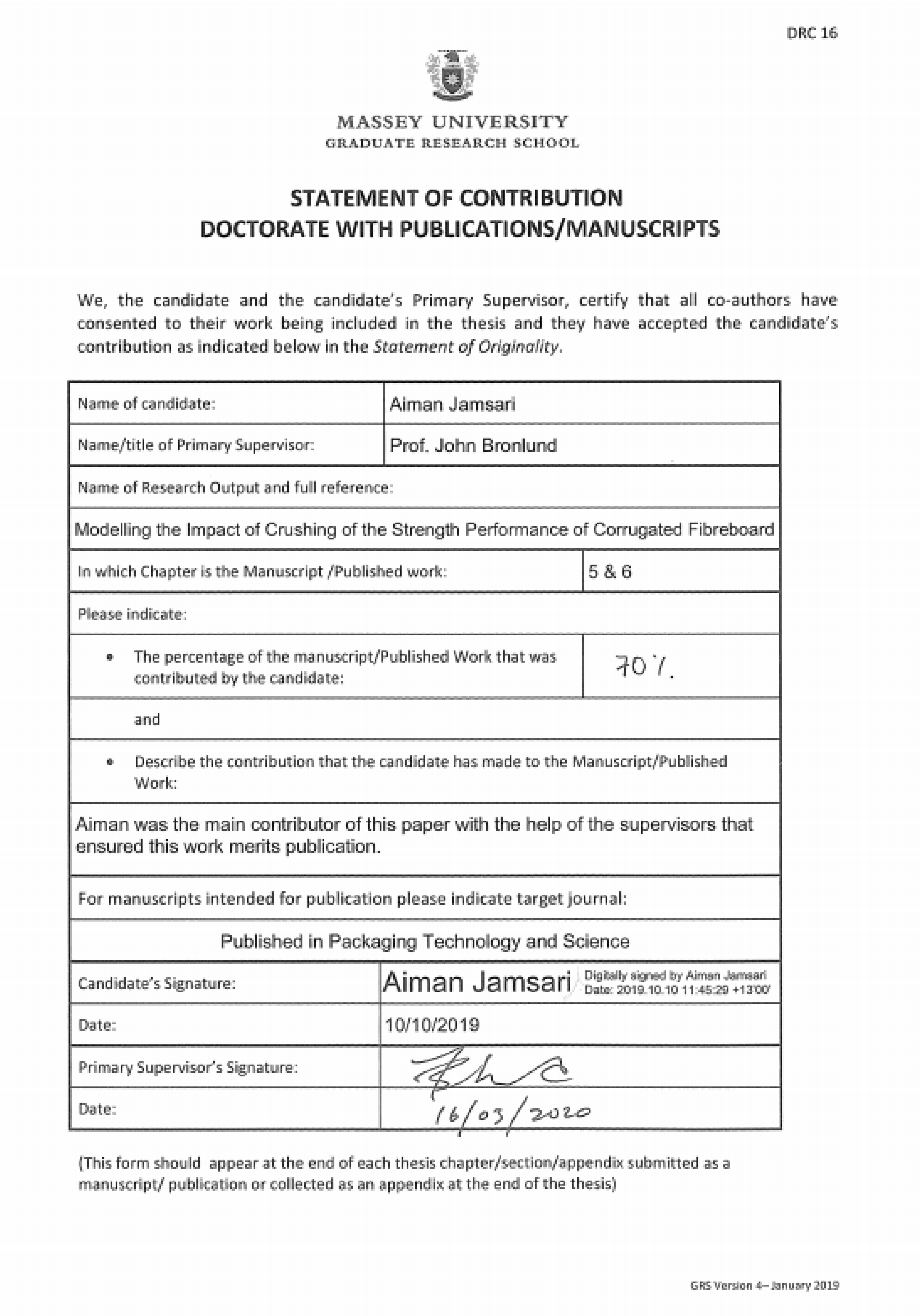

DRC 16

MASSEY UNIVERSITY
GRADUATE RESEARCH SCHOOL

STATEMENT OF CONTRIBUTION
DOCTORATE WITH PUBLICATIONS/MANUSCRIPTS

We, the candidate and the candidate's Primary Supervisor, certify that all co-authors have consented to their work being included in the thesis and they have accepted the candidate's contribution as indicated below in the *Statement of Originality*.

Name of candidate:	Aiman Jamsari
Name/title of Primary Supervisor:	Prof. John Bronlund
Name of Research Output and full reference:	
Modelling the Impact of Crushing of the Strength Performance of Corrugated Fibreboard	
In which Chapter is the Manuscript /Published work:	5 & 6
Please indicate:	
• The percentage of the manuscript/Published Work that was contributed by the candidate:	70%
and	
• Describe the contribution that the candidate has made to the Manuscript/Published Work:	
Aiman was the main contributor of this paper with the help of the supervisors that ensured this work merits publication.	
For manuscripts intended for publication please indicate target journal:	
Published in Packaging Technology and Science	
Candidate's Signature:	Aiman Jamsari Digitally signed by Aiman Jamsari Date: 2019.10.10 11:45:29 +13'00'
Date:	10/10/2019
Primary Supervisor's Signature:	
Date:	16/03/2020

(This form should appear at the end of each thesis chapter/section/appendix submitted as a manuscript/ publication or collected as an appendix at the end of the thesis)

GRS Version 4– January 2019